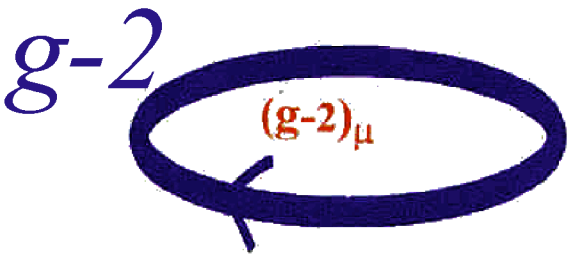

Brookhaven National Laboratory

Brookhaven Science Associates

Upton, New York 11973

Muon g-2 Note No. 415

Title: **Energy-binned Analysis of the 2000 ω_a Data**

Author: **Fred Gray**

Affiliation: **University of Illinois**

Date: **September 5, 2002**

Energy-binned analysis of the 2000 ω_a data

Fred Gray

5th September 2002

Abstract

This document gives a measurement of the muon anomalous precession frequency ω_a in the data from the 2000 $g-2$ run, including estimates of some of the systematic uncertainties. The data are divided into energy bins of width 200 MeV, and each energy bin is fitted separately. This allows the use of the full statistical power of the data, and it has somewhat different systematic issues than the traditional approach. The recommended value of ω_a corresponds to $R = 128.71 \pm 0.70(\text{stat.}) \pm 0.26(\text{syst.})$. The total uncertainty, statistical and systematic combined, is 0.75 ppm. This result is biased by a previously secret offset of +14.744 ppm.

1 Philosophy

There are many reasons why it is interesting to perform an energy-binned analysis:

- The statistical uncertainty of the result is reduced. Over the range from 2.0 GeV to 3.2 GeV, the uncertainty is 5 percent smaller for the energy-binned method than for the traditional fit. Even more statistical power can be gained by lowering the threshold to 1.4 GeV, since the low-asymmetry data does not dilute the high-asymmetry data. This process yields a statistical uncertainty that is 12 percent smaller than for the 2.0-3.2 GeV conventional fit.

- The CBO modulation of the asymmetry (the so-called "Rob effect") could be suppressed by fitting in narrow energy bins. Indeed, this modulation arises entirely from the mixing of energies. In the expression

  $$\int dE e^{-t/\tau} N(E)[1+A(E)\cos(\omega_a t+\phi(E))][1+e^{-t/\tau_{CBO}} A_{CBO}(E)\cos(\omega_{CBO} t+\phi_{CBO}(E))]$$

  note that the CBO modulation of the non-wiggling part is weighted with $N(E)$ whereas for the wiggling part it is weighted with $N(E)A(E)$. (Unfortunately, this potential advantage is not apparent in practice; the asymmetry modulation amplitude in a single energy bin is found to be comparable to that in the entire range.)

- Mapping ω_a as a function of energy provides a substantial consistency check, possibly excluding classes of unknown systematic errors that would affect R differently for different energies.

- Determining the energy dependence of parameters other than ω_a can provide insight into subtle effects. Most notably, the CBO amplitudes and phases as a function of energy have been used to construct beam dynamics models.

- When all three of the CBO effects (rate, asymmetry, and phase modulations) are included in the fitting function, ω_a drifts significantly as a function of fit start time. For some reason, this drift is smaller when fitting by energy bin.

This analysis does not use explicit "mop" terms. Where possible, known effects are taken into account. Then, stations are included in the fit only at start times where their spectra can be fit with physically motivated terms.

2 Executive summary

This report gives six different results. All of them are based on the same functional form, which is the full physics function including all known CBO-related effects. The start times are determined by three different criteria, called A, B, and C. In method A, all stations simply start at 49.1 μs. In method B, each station is allowed to start at its own appropriate time. Method C extends this further, allowing a different start time for each energy bin. The other variable is the energy range that is included; results A', B', and C' use energies from 2.0 GeV to 3.2 GeV whereas the unprimed results A, B, and C extend this range down to 1.4 GeV.

Results A and A' are presented for comparison purposes only, since they do not yield an acceptable χ^2/dof. Among the other four results, C is chosen as the recommended value because it has the smallest uncertainty.

The results and their associated systematic errors are shown in Table 1.

	A	A'	B	B'	**C**	C'
R	128.996	128.866	128.105	127.857	**128.711**	128.589
Statistics	0.636	0.686	0.727	0.781	**0.701**	0.754
χ^2/dof	1.0109	1.0100	1.0032	1.0030	**1.0033**	1.0027
$\delta\chi^2$/dof	0.0018	0.0023	0.0019	0.0023	**0.0019**	0.0023
Included in statistics:						
Half ring effect	0.270	0.289	0.312	0.334	**0.297**	0.319
Pileup statistics	0.112	0.131	0.095	0.114	**0.117**	0.131
Gain	0.037	0.045	0.070	0.086	**0.086**	0.10
Pileup scale	0.194	0.175	0.156	0.170	**0.167**	0.175
Pileup energy dependence	0.080	0.080	0.080	0.080	**0.080**	0.080
Unseen pileup	0.057	0.076	0.073	0.090	**0.085**	0.104
Muon loss scale	0.072	0.058	0.043	0.034	**0.048**	0.037
Muon loss shape	0.039	0.027	0.019	0.016	**0.014**	0.008
Flashlets	0.011	0.013	0.002	0.002	**0.019**	0.021
CBO frequency	0.033	0.039	0.085	0.098	**0.042**	0.005
Main CBO envelope	0.057	0.053	0.024	0.017	**0.016**	0.005
CBO phase modulation envelope	0.102	0.095	0.079	0.032	**0.021**	0.032
Random seed	0.045	0.045	0.053	0.051	**0.046**	0.041
Bin width	0.061	0.057	0.151	0.123	**0.094**	0.103
Vertical waist	0.0051	0.0047	0.0071	0.0082	**0.0030**	0.0038
Double CBO	0.012	0.0082	0.0066	0.00066	**0.0083**	0.011
Lost protons	0.002	0.007	0.005	0.008	**0.003**	0.007
Systematics (quadrature)	0.276	0.260	0.288	0.285	**0.255**	0.271
Total uncertainty	0.693	0.733	0.782	0.832	**0.746**	0.802

Table 1: Summary of fitted R values (including offset), with statistical and systematic error estimates.

3 Data selection

In general, Ernst Sichtermann's run list of January 9, 2002 is used to define the data set for this analysis. There are a number of runs in the list, at the level of a few percent, which are not included because of local data processing problems.

Detector station 2 is not used in this analysis, because a WFD problem leads to a distorted average pulse shape for it; this is the same problem that caused it to be excluded in the 1999 analysis. In principle, detector station 20 is usable; it was at the same radial position as the other detectors for the 2000 run, and it was calibrated by the same procedure as the other detectors. Nevertheless, its energy distribution is very different than that of the other detectors because the traceback chambers are located directly upstream from it. More importantly, it has a large background, uniform in time and very visible at late times, that is not present in other detectors. The source of this background is not understood; one model is that it arises from electrical noise created by the traceback electronics that are mounted on it. Consequently, this station is excluded from this analysis as well.

Laser runs are included in the data set. Fills containing laser pulses are removed by looking at the laser reference WFD and the CAMAC ADCs. It should be noted that the data acquisition system does not necessarily preserve the synchronization of fills between crates when a fill is missed by a subset of the crates. Consequently, it is possible for a few laser pulses to be included in the data set even when checks are made to exclude them. This is not believed to be a large effect, however.

The sweeper magnet was in place for most of the 2000 run, so flashlets are much less of a concern than in the 1999 analysis. Consequently, the current analysis uses only a fill-by-fill cut on the T0 counter rather than an AGS-cycle-by-AGS-cycle cut. This change was necessary in order to be able to use the data collected with only ten of the twelve AGS bunches populated. The precise requirement is that there must be exactly one pulse in the T0 counter with a height greater than 20 ADC counts. Because this cut is below the hardware threshold, the effective requirement is that there be exactly one waveform digitizer trigger for the T0 counter, excluding marker pulses and forced digitizations. Because the quadrupole firing was suppressed for a subset of the fills in the 2000 run, flashlet data is available to evaluate this choice quantitatively. An estimate of the systematic error due to flashlets is given later in this report.

The digitized traces of the electrostatic quadrupoles were checked to ensure that the quadrupole trace extends to at least 700 μs after the data acquisition start signal (about 640 μs after injection). The precise requirement is that the value at 125 μs after the data acquisition start signal must not differ by more than 20 ADC counts from the value at 700 μs. In addition, a check is performed to identify fills where the quadrupole firing was suppressed. If the value in the trace does not change by more than 5 ADC counts over the range from 2.5 μs to 600 μs after the data acquisition start signal, then the quadrupoles did not fire in that fill.

Some statistics on the number of counts lost to each of these cuts are shown in Table 2. About six percent of the data from the runs on Ernst Sichtermann's list is lost.

The fast rotation modulation is removed by adding a random offset to the fill's T0 time. A separate random number sequence is used for each detector station. The random numbers

Issue	> 2.0 GeV, > 50 μs	> 1.4 GeV, > 50 μs
Total included (not cut)	3.73×10^9	7.84×10^9
Laser fills	9.1×10^7	1.9×10^8
Data processing faults (est.)	6.1×10^7	1.3×10^8
Quad trace not recorded	4.8×10^7	1.0×10^8
Number of T0 events $\neq 1$	2.5×10^7	5.3×10^7
T0 trace not recorded	5.0×10^6	1.1×10^7
Possible quad spark	1.6×10^6	3.3×10^6

Table 2: Number of events lost due to various cuts compared with the number of events included.

are chosen from a uniform distribution over the range from -74.6 ns to 74.6 ns. ROOT's `TRandom3` random number generator is used. The authors claim that this random number generator has a period of $2^{19937} - 1$. The result is averaged over five random seeds. However, the systematic studies use only a single seed (indeed, not all of the studies even use the same seed). Systematic uncertainties are attributed to the random seed and to the fast rotation time.

A parameterization of the gain corrections determined from the average energy vs. time is applied to the data. The method by which these corrections are obtained is described in detail later in the report, and a systematic uncertainty is attributed to them.

The times and energies are computed with `G2Too`'s `MilliFit` pulse finding algorithm [2]. However, the run-to-run endpoint calibrations that convert pulse area to energy were taken from Ernst Sichtermann's analysis, which used `G2OFF` data. They were scaled by a factor which was constructed to give in each detector a $(g-2)$ asymmetry of 0.4 over the energy range from 2.0 to 3.2 GeV. Time offsets were applied to give a $(g-2)$ phase of 0 over the same energy range.

4 Pileup construction method

The pileup construction procedures that were used for the 1999 data analysis work effectively for pileup at energies greater than twice the WFD hardware threshold. This was adequate for the 1999 data, where the hardware thresholds were set below 1 GeV. During the 2000 run, though, the thresholds for several of the detectors were raised as high as 1.4 GeV. Also, the average intensity per fill is 50 percent higher in the 2000 data, so the motivation for effective pileup subtraction is even greater. Consequently, the procedure was extended to allow effective pileup subtraction at lower energies.

The "raw material" for the pileup subtraction procedure is a set of spectra made for each run separately and then summed. Each of the following is a two-dimensional histogram with time bins of width 150 ns and energy bins of width 200 MeV:

- A conventional spectrum with all fitted events in the selected data set included, with a 10 ns artificial deadtime applied. The algorithm for applying the artificial deadtime is defined below. The 10 ns parameter was chosen by examining the spectrum of time differences Δt between successive pulses. 10 ns is near the point where the pulse finder becomes fully efficient for finding even very low-energy pulses.

- A "shadow pulse" spectrum that includes all pulses which fall in the intervals between 10 ns and 15 ns before and after a "trigger pulse" whose energy is greater than the assumed WFD hardware threshold. For each time bin, this gives the full energy distribution, independent of the hardware threshold. The 10 ns to 15 ns window was chosen because it is generally the flattest portion of the Δt spectrum. This spectrum will be called $S_{new}(E,t)$.

- A constructed two-pulse pileup spectrum based on the shadow pulse spectrum. The energies of consecutive shadow pulse events from the same time bin are added together and multiplied by an adjustment factor that accounts for the nonlinearity of the pulse fitter. This factor is drawn for each pulse from a distribution; on average, it is 0.94. The pulses that are combined are usually from different fills and often even from different runs. This spectrum will be called $D_{new}(E,t)$.

- A "shadow+trigger pulse" distribution that includes both the set of shadow pulses and the set of trigger pulses. This spectrum will be called $S_{old}(E,t)$.

- A constructed two-pulse pileup spectrum based on the shadow+trigger pulse spectrum. The energies of corresponding shadow and trigger pulses are added together and multiplied by the nonlinearity adjustment factor. In this case, the pulses that are combined are always from the same WFD digitization interval. This spectrum will be called $D_{old}(E,t)$.

The conventional pileup construction that was used in the 1999 analysis is

$$N_{PUold}(E,t) = D_{old}(E,t) - S_{old}(E,t)$$

This spectrum is correct for energies E greater than twice the WFD hardware threshold $E_{HWthresh}$. It is not correct for lower energies: a pileup event with energy $2E_{HWthresh} - \epsilon$ can

be made by overlapping two pulses each with an energy $E_{HWthresh} - \epsilon/2$. This combination would not trigger the WFD, so it would not be included in the constructed pileup. However, at energies where the method works, it should obtain the correct pileup normalization. Conversely, the new pileup construction $N_{PUnew} = D_{new}(E,t) - S_{new}(E,t)$ obtains the correct energy distribution in each time bin. However, it does so only up to an arbitrary time-dependent normalization factor.

The improved pileup construction is

$$N_{PU}(E,t) = f_{old/new}(t)[D_{new}(E,t) - S_{new}(E,t)]$$

with

$$f_{old/new}(t) = \frac{\int_{E_L}^{E_U} D_{old}(E,t)}{\int_{E_L}^{E_U} D_{new}(E,t)}$$

The limits of integration are E_L=2.8 GeV and E_U=4.0 GeV. The lower limit is chosen to be just above twice the highest hardware threshold; the upper limit is somewhat arbitrary. This method uses the conventional pileup construction to set the scale factor, but it takes the energy distribution at low energies from the new construction. In practice, the scale factor is fit to a function of the form

$$f_{old/new}(t) = N(1 + A\cos(\omega_a t + \phi))$$

and the function is evaluated at each point rather than using the actual data there.

It should be noted that the pileup construction is intrinsically symmetric in time around the trigger pulse; pre-shadow pulses (in the window before the trigger pulse) are treated the same as post-shadow pulses (in the window after the trigger pulse). This approximately removes the $g-2$ phase shift between the real and the constructed pileup. However, to avoid double-counting, pre-shadow pulses are never combined with post-shadow pulses; they are treated as two separate streams of events until they are matched up.

A small correction is applied to the pileup spectrum to account for the fast rotation modulation. At very early times, the rate in the trigger pulse window differs substantially from the rate in the shadow pulse windows. The correction is given by

$$\frac{< R^2_{trigger}(t) >}{< R_{trigger}(t) \cdot R_{shadow}(t) >}$$

$R_{trigger}(t)$ is the average rate in a $\pm$10 ns window around time t, $R_{shadow}(t)$ is the average rate in the regions where shadow pulses are collected, and the brackets imply an average over a fast rotation cycle. The correction was calculated from the data itself in fine time bins; it is shown in Figure 1. It is a 0.5 percent effect at 30 μs, and it is completely negligible by 40 μs.

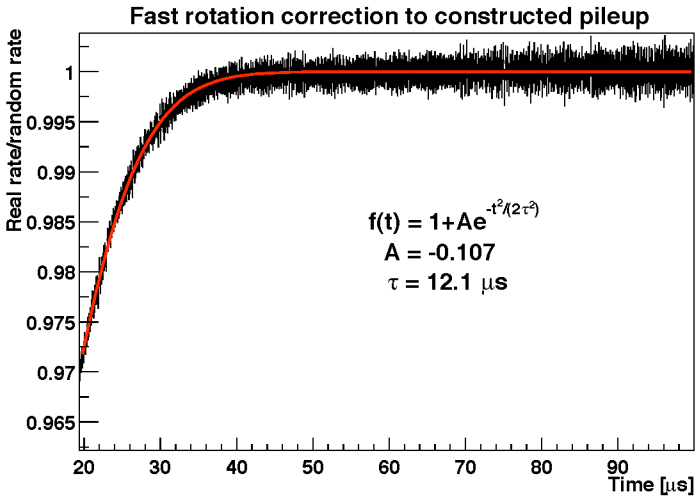

Figure 1: Correction to constructed pileup from the fast rotation modulation.

5 Fits to constructed pileup spectrum

The pileup spectrum is expected to be described by a function of the form

$$\begin{aligned} N_{PU}(t) &= e^{-2t/\tau} F_{FR}(t) \\ &\quad [1 + e^{-t/\tau_{CBO}} E(t) A_{CBO} \cos(\omega_{CBO} t + \phi_{CBO})]^2 \\ &\quad [N_{PU} - A_{PU1} \cos(\omega_a t + \phi_{PU1}) - A_{PU2} \cos(2(\omega_a t + \phi_{PU2})] \end{aligned}$$

$F(t)$ accounts for the enhancement of the pileup by the fast rotation [7]. It was determined by calculating on a finely binned time spectrum $R(t)$

$$F_{FR}(t) = \frac{< R^2(t) >}{< R(t) >^2}$$

where the brackets imply an average over a fast rotation cycle. It is approximated by the function

$$F_{FR}(t) = N_{FR} \exp(-\frac{t^2}{2\tau_{FR}^2})$$

with $N_{FR} = 2.21$ and $\tau_{FR} = 5.78\mu$s. It has previously been parameterized with two Gaussian functions, but the extra structure is not relevant after 50 μs. These values are fixed in the fit.

In practice, the lifetime τ and the frequency ω_a are fixed in these fits. The values that are used are $\tau = 64.4076$ μs and $R = 128.55$ ppm. The CBO parameters are also fixed to the same values that are used for the fits to the ordinary spectra, which will be discussed later.

It has been noted (see [1]) that a correction to the χ^2 (specifically, to the error estimate σ) is required when fitting a pileup-subtracted spectrum. The extensions to the new pileup-subtraction method cause this correction to become both larger and less straightforward to compute. The problem is made somewhat more tractable by first fitting the constructed pileup spectrum, then using those results to fix parameters in the physics fits. When fitting the pileup spectrum in narrow energy bins, no χ^2 correction factor is necessary. This is true because there are no pulses below the pulse finder's threshold of about 200 MeV, so the spectrum of single pulses lost from a bin whose width is less than this threshold is statistically independent from the spectrum of double pulses gained. The uncertainty assigned to each point is taken to be

$$\delta N_{PUnew}(E,t) = f_{old/new}(t) \sqrt{D_{new}(E,t) + S_{new}(E,t)}$$

Clearly, this is only an approximation, since it implies perfect knowledge of $f_{old/new}(t)$.

The fits are performed with a per-station start time determined from the flatness of the χ^2/dof. The algorithm that was used to determine these times is described later in this report. The stop time for all of the fits is 120 μs.

It is clear that there is not a single best way to present the results of 198 fits (22 stations, 9 energy bins per station) so that they are both meaningful and reasonably compact. The trends versus energy are mostly independent of the station number, so each parameter is shown as a function of energy, averaged over all stations, in Figure 2. The results of all

of the individual fits are shown in Figures 3 through 5. In these plots, the nine leftmost points are the fits to station 1 in order of increasing energy. The next nine points are absent, corresponding to the nine energy bins of station 2; other stations follow similarly. In addition, stations alternate marker style and color.

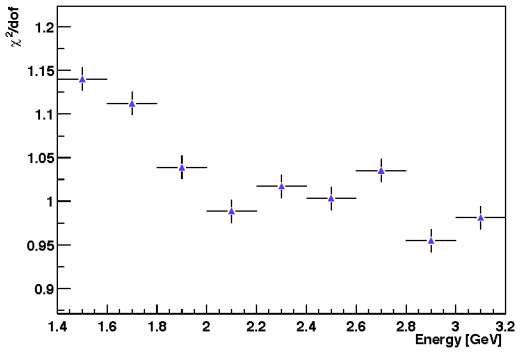

(a) χ^2/dof

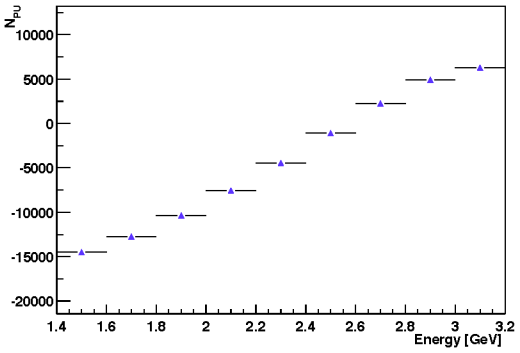

(b) N_{PU}

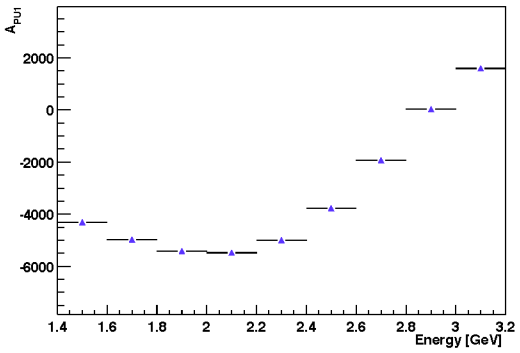

(c) A_{PU1}

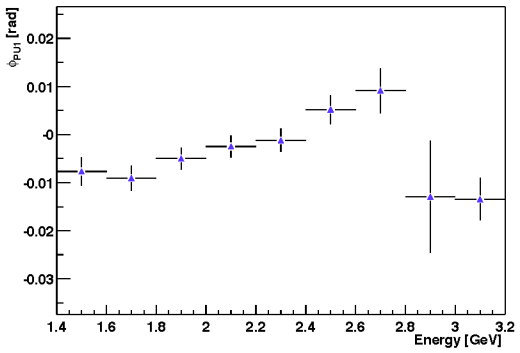

(d) ϕ_{PU1}

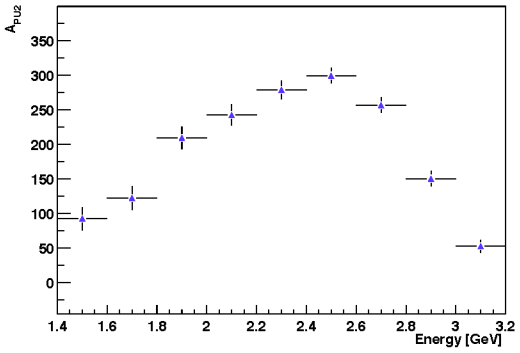

(e) A_{PU2}

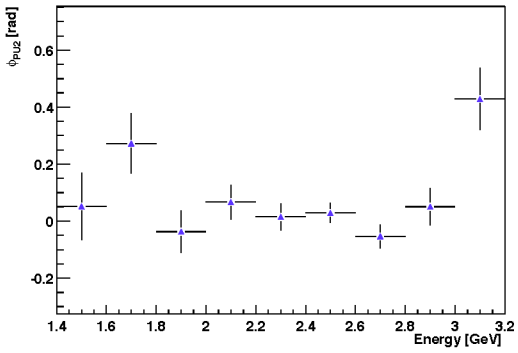

(f) ϕ_{PU2}

Figure 2: Results of fits to constructed pileup spectrum by energy bin, averaged over detectors. These results are from the earliest allowed fit start time to 120 μs.

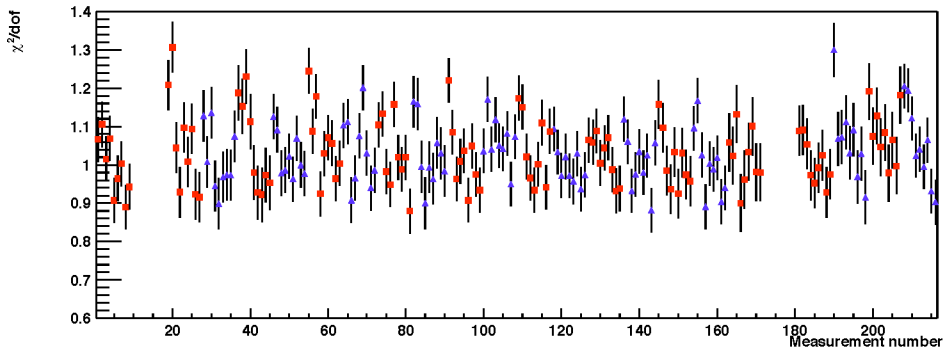

(a) χ^2/dof

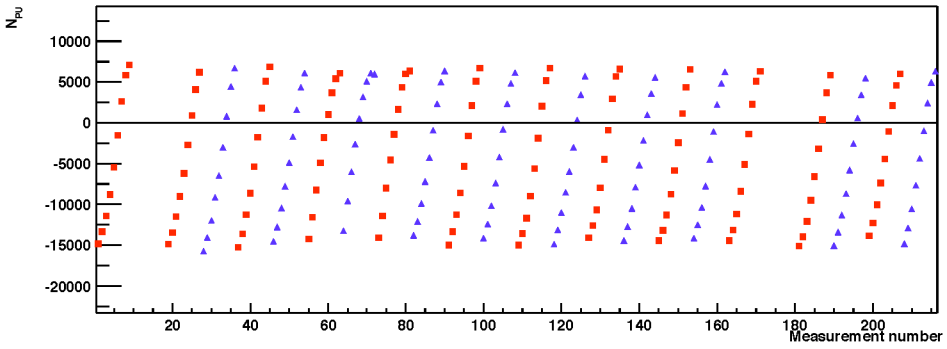

(b) N_{PU}

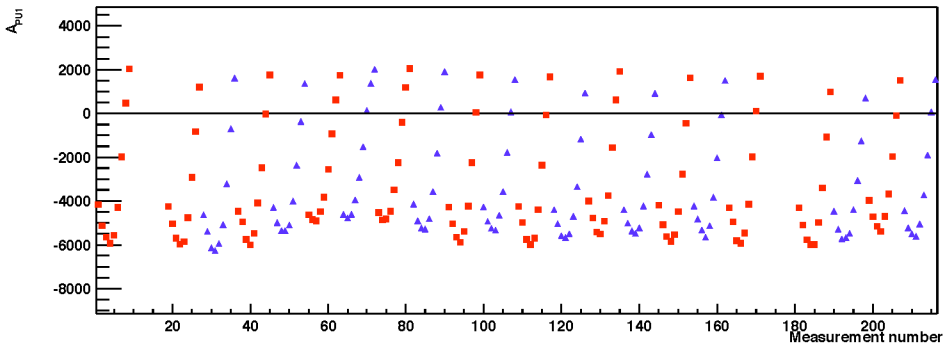

(c) A_{PU1}

Figure 3: Results of fits to constructed pileup spectrum by energy bin and by detector. These results are from the earliest allowed fit start time to 120 μs.

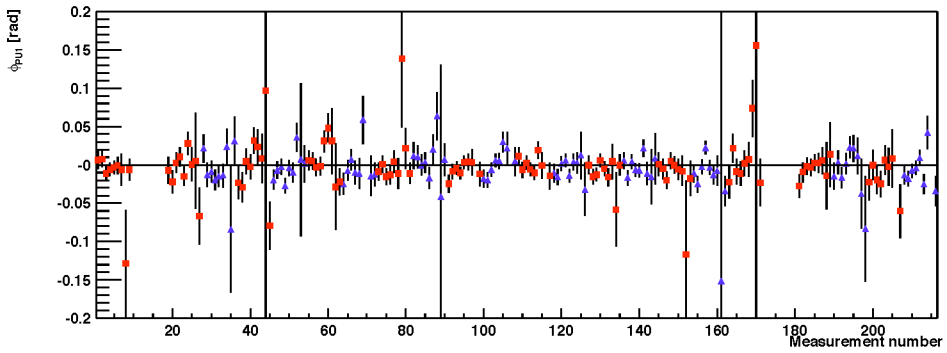

(a) ϕ_{PU1}

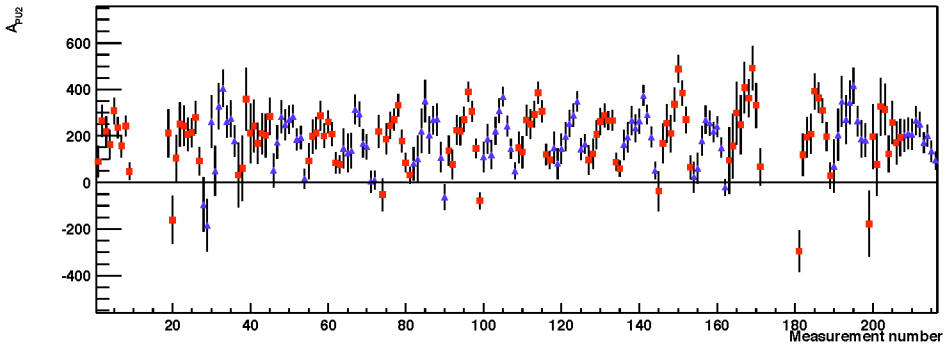

(b) A_{PU2}

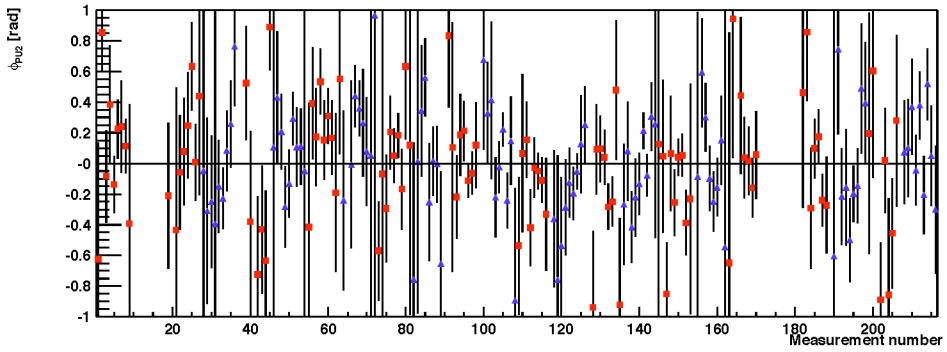

(c) ϕ_{PU2}

Figure 4: Results of fits to constructed pileup spectrum by energy bin and by detector. These results are from the earliest allowed fit start time to 120 μs.

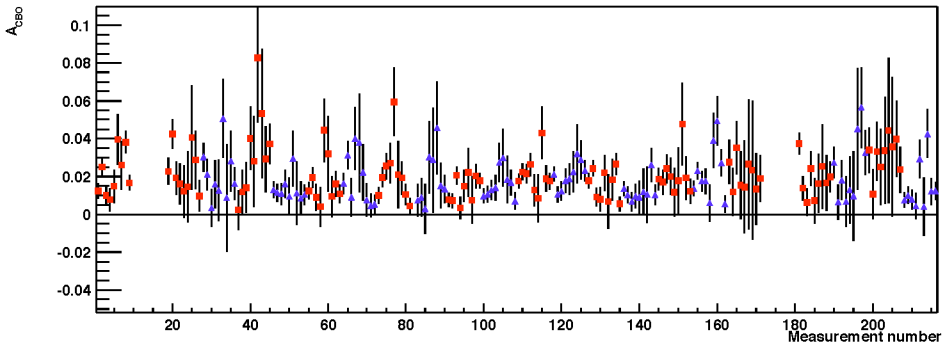

(a) A_{CBO}

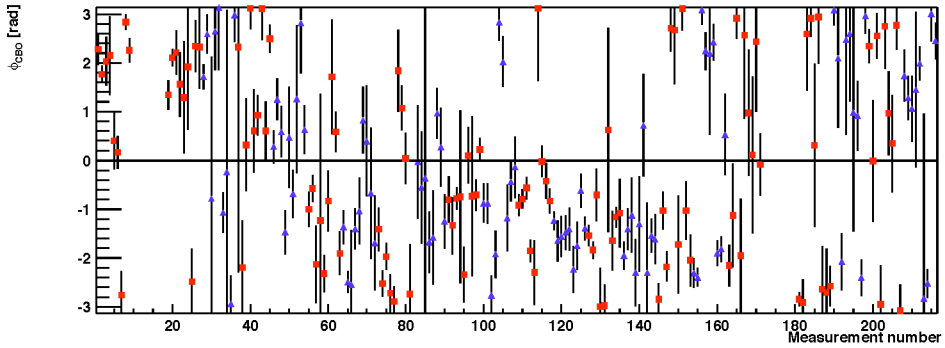

(b) ϕ_{CBO}

Figure 5: Results of fits to constructed pileup spectrum by energy bin and by detector. These results are from the earliest allowed fit start time to 120 μs.

6 Fitting procedures

The overall form of the function that is used to fit the data is

$$N(t) = e^{-t/\tau}\Lambda(t)[NC_1(t) - A(C_1(t) + C_2(t))\cos(\omega_a t + \phi)] + N_{PU}(t)$$

The CBO modulation of the rate and the apparent CBO modulation of the $g-2$ amplitude (i.e. the "Rob effect") are included in C_1 and C_2:

$$C_1(t) = 1 + e^{-t/\tau_{CBO}}E(t)[A_{CBO1C}\cos\omega_{CBO}t + A_{CBO1S}\sin\omega_{CBO}t]$$

$$C_2(t) = e^{-t/\tau_{CBO}}E(t)[A_{CBO2C}\cos\omega_{CBO}t + A_{CBO2S}\sin\omega_{CBO}t]$$

The modulation of the $g-2$ phase by the CBO ("Jim effect") is included by modifying the time throughout the fitting function:

$$t = t_{in} + C_3(t)$$

$$C_3(t) = e^{-t/\tau_{CBO3}}E(t)[A_{CBO3C}\cos\omega_{CBO}t + A_{CBO3S}\sin\omega_{CBO}t]$$

Parameterizing the CBO effects with sine and cosine amplitudes rather than with an amplitude and a phase leads to more reliable fit convergence when the phase is difficult to predict in advance.

The CBO frequency ω_{CBO} is assumed to be time-independent, although it is known that it changes slightly over the fill time. These changes occur at early times as the n values varies during the transition from scraping to non-scraping quadrupole voltages, and at late times because the quadrupole voltage slowly drops. Systematic uncertainties will be assigned for these effects. Also, the CBO frequency is now fixed in the fits, in contrast to previous versions of this analysis. A systematic uncertainty is also assigned for it.

Several variations of the fit function are occasionally used in this report. They differ in the CBO effects that are included:

- : "rate only": $C_1(t)$ included in fit; $C_2(t) = C_3(t) = 0$
- : "rate+asymmetry": $C_1(t)$ and $C_2(t)$ included in fit; $C_3(t) = 0$
- : "rate+asymmetry+phase": $C_1(t)$, $C_2(t)$, and $C_3(t)$ all included in fit
- : "rate+phase": $C_1(t)$ and $C_3(t)$ included in fit; $C_2(t) = 0$

The "rate+asymmetry+phase" function is used unless otherwise noted.

Muon losses are incorporated with the term

$$\Lambda(t) = \exp[-N_\Lambda/\tau\int_{t_0}^{t}(f_\Lambda(t') + N_{\delta\Lambda}\delta f_\Lambda(t'))dt']$$

$f_\Lambda(t)$ is the fractional muon loss rate measured by three-fold coincidences in the FSDs, as determined by Chris Polly in [3]. $\delta f_\Lambda(t)$ is his estimate of the error band on the shape. These functions are shown in Figure 6. The overall normalization factors N_Λ and $N_{\delta\Lambda}$ were

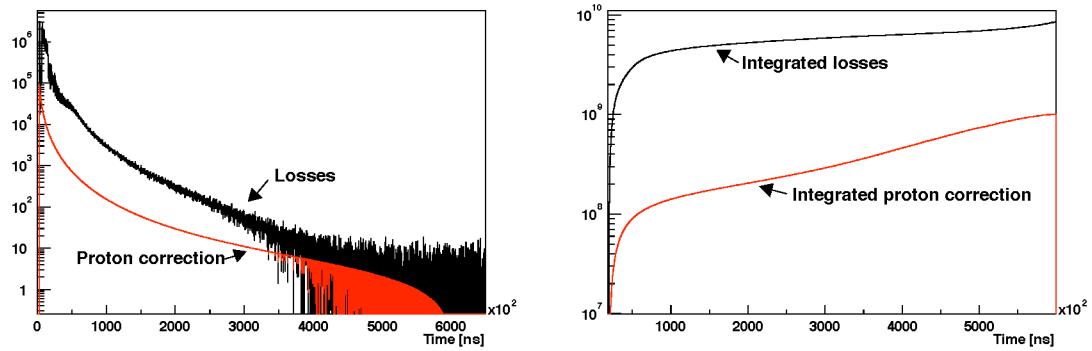

(a) Before time integration

(b) After time integration

Figure 6: Muon loss function $f_\Lambda(t)$ together with its uncertainty $\delta f_\Lambda(t)$. The label "proton correction" is not accurate; the lower curve is the uncertainty on the shape.

determined once from a global χ^2 minimization for start time set C. They are thus fixed at the values $N_\Lambda = 1.62 \times 10^{-7}$ (arbitrary units) and $N_{\delta\Lambda} = 2.53$.

Pileup is taken into account by including the term $N_{PU}(t)$ as defined in section on pileup fitting. All of the pileup parameters are now fixed, in contrast with previous versions of this analysis.

Previous versions of this analysis contained terms to account for vertical betatron, vertical waist, and double CBO modulations. Because all stations and energy bins have fit start times that are too late to be significantly affected by these oscillations, these terms were removed from the fitting function. Systematic uncertainties are assigned for these effects instead.

7 Fit start and stop times

Three sets of fit start times are used for the results cited in this report:

- **A**: All fits start at 49.1 μs. This result does not yield an acceptable χ^2/dof, so it is given for comparison with other ω_a analyses only.
- **B**: Each station starts at a different time. The earliest allowable fit start time was determined for each detector based on the flatness of its χ^2/dof as a function of time. The earliest χ^2/dof point at which 68.2 percent of the subsequent points fall within the one standard deviation correlated error band was chosen. However, no station was allowed to start before 45 μs. These start times are based on the average χ^2/dof across energy bins for each detector; plots of this quantity appear in Figures 7 through 10. The start times are moved later in time to the $(g-2)$ zero crossing immediately after the first acceptable point.
- **C**: An earliest start time is determined separately for each energy bin within each station. Again, the times are based on the stability of the χ^2/dof. However, the consistency requirement is tightened somewhat: to accept a start time, no more than 15.9 percent of the subsequent points may fall above the correlated error band, and no more than 15.9 percent may fall below it.

The correlated error between the χ^2/dof at time t_1 (with N_{DF1} degrees of freedom) and the same quantity at time t_2 (with N_{DF2} degrees of freedom) is taken to be

$$\frac{\sqrt{2(N_{DF1}-N_{DF2})}}{N_{DF2}}$$

Sergei Redin has written a rigorous proof [4] of this result, which I had written down semi-intuitively. Curiously, the formula seems to give approximately the same numerical result as the standard "Kawall band."

The average χ^2/dof values for each station are plotted in Figures 7 through 10. The earliest allowed fit start times are shown for each detector in Figure 11. They have been moved forward to the $g-2$ zero crossing immediately after the first acceptable point. As a cross-check (suggested by Ernst Sichtermann), the distributions of point-to-point differences in the χ^2/dof after the first acceptable fit start time are plotted in Figure 12. For both methods A and B, the mean of the distribution is indeed at 0. However, the distributions are distinctly asymmetric about the mean.

The stop time for each fit is at the first time bin to have fewer than 20 counts. This implies that higher-energy bins have an earlier stop time than lower-energy bins.

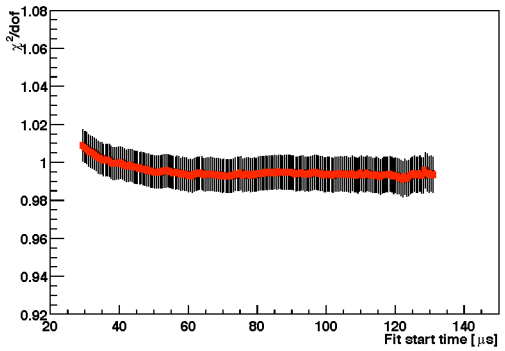

(a) Station 1

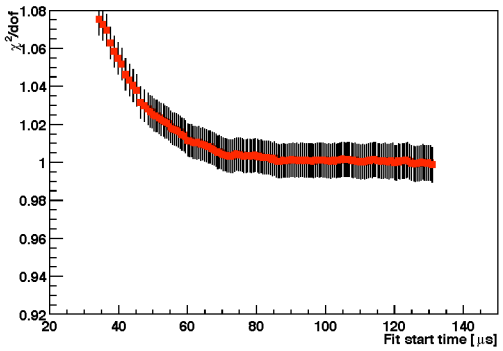

(b) Station 3

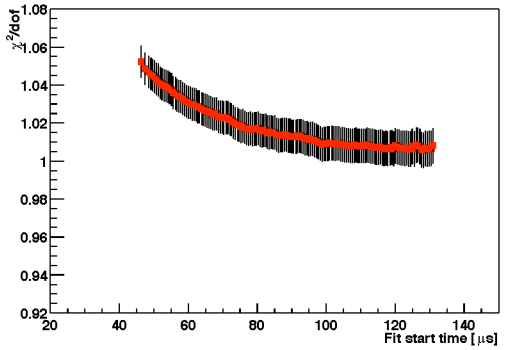

(c) Station 4

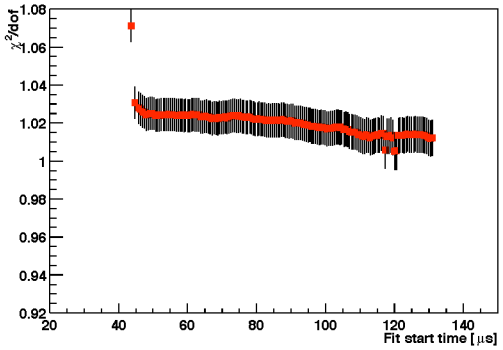

(d) Station 5

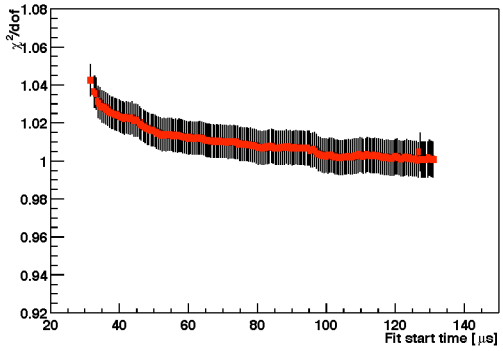

(e) Station 6

Figure 7: χ^2/dof averaged across energy bins for each station as a function of fit start time. Stations 1-6.

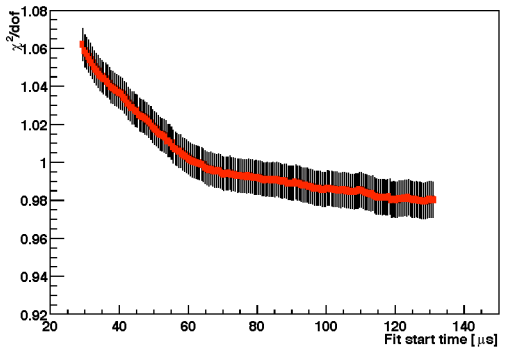

(a) Station 7

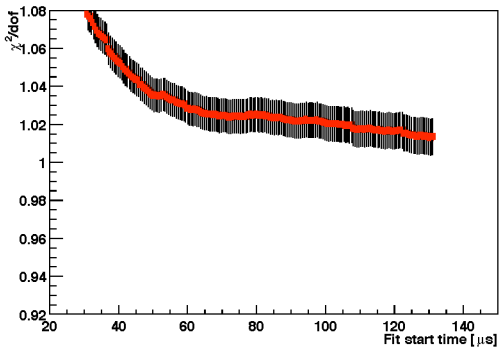

(b) Station 8

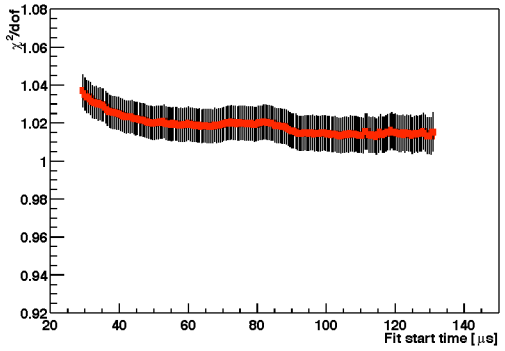

(c) Station 9

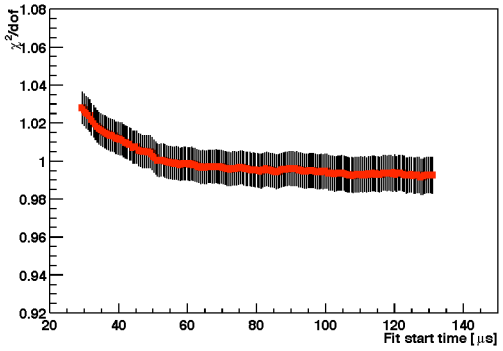

(d) Station 10

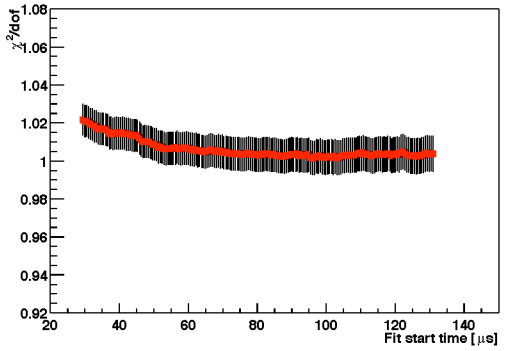

(e) Station 11

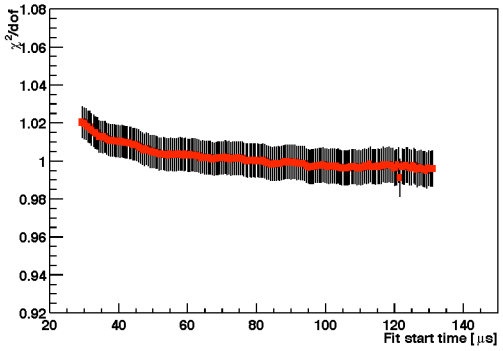

(f) Station 12

Figure 8: χ^2/dof averaged across energy bins for each station as a function of fit start time. Stations 7-12.

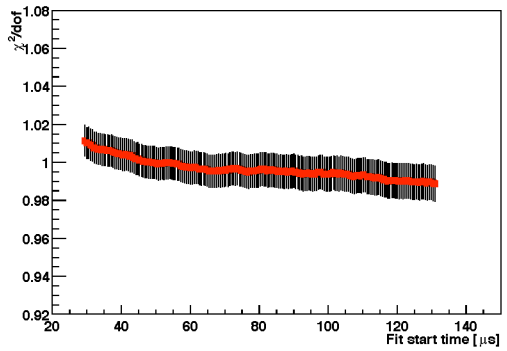

(a) Station 13

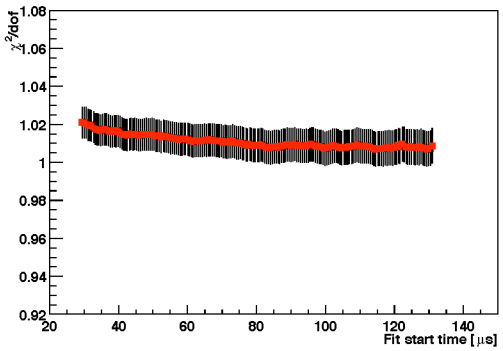

(b) Station 14

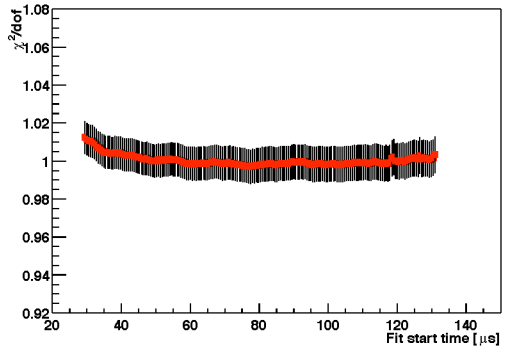

(c) Station 15

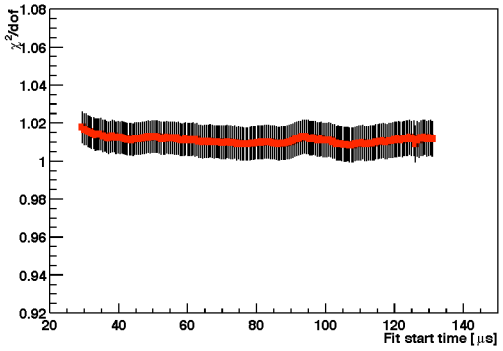

(d) Station 16

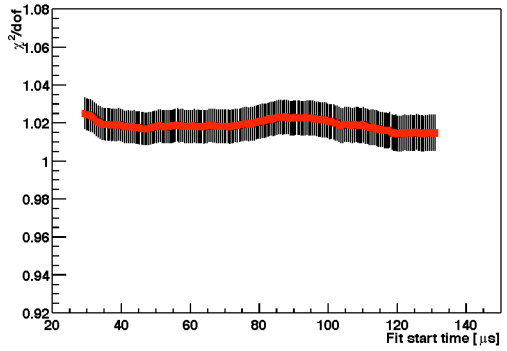

(e) Station 17

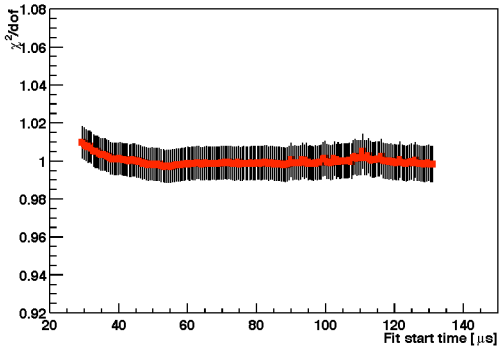

(f) Station 18

Figure 9: χ^2/dof averaged across energy bins for each station as a function of fit start time. Stations 13-18.

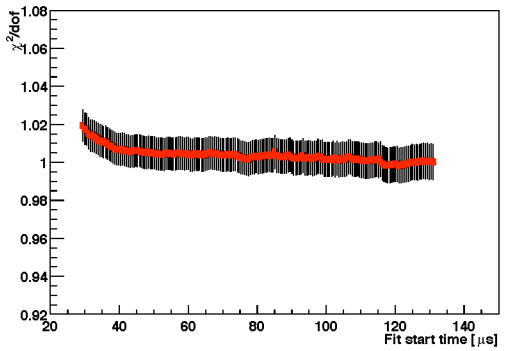

(a) Station 19

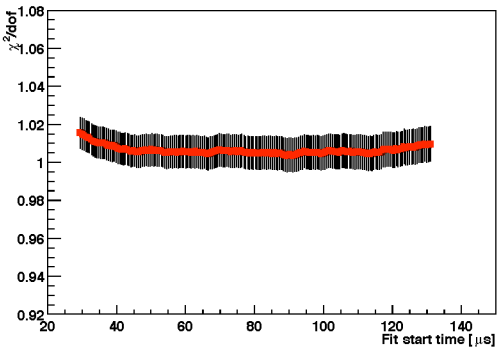

(b) Station 21

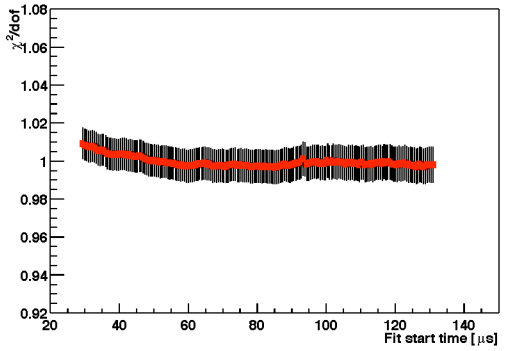

(c) Station 22

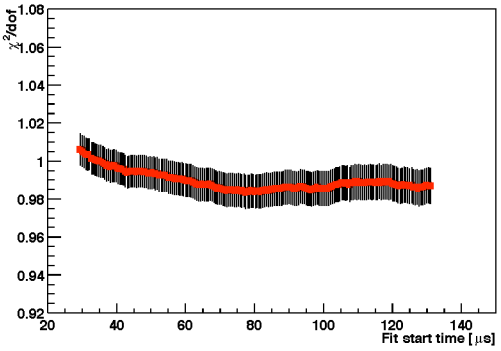

(d) Station 23

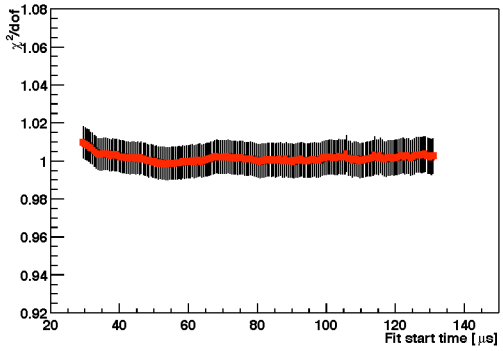

(e) Station 24

Figure 10: χ^2/dof averaged across energy bins for each station as a function of fit start time. Stations 19-24.

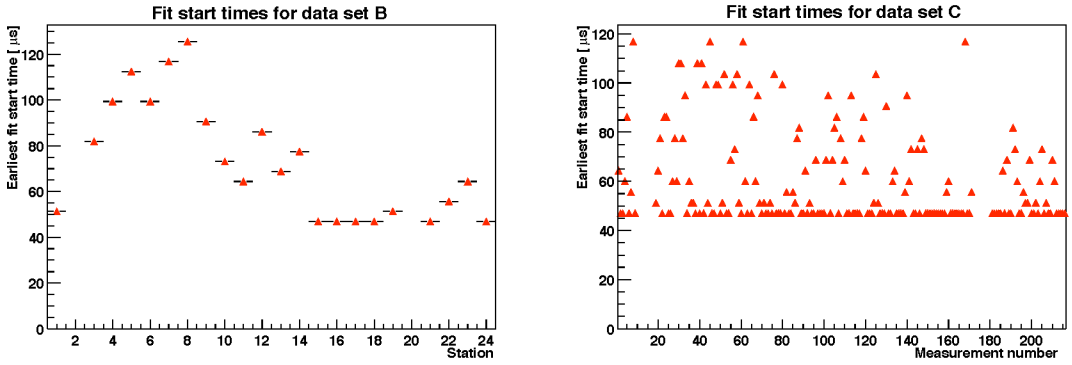

(a) Method B: by station

(b) Method C: by energy bin

Figure 11: Earliest start times used for each station (in method B) or each energy bin (in method C). Method A chooses all start times at 49.1 μs.

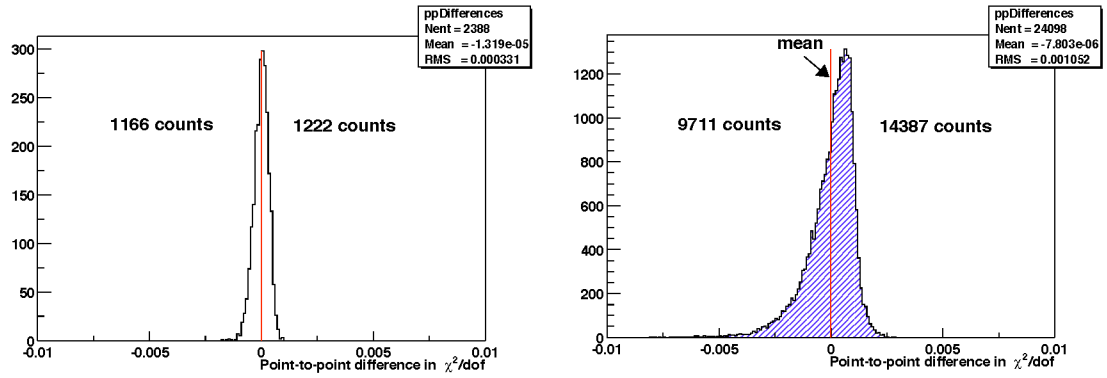

(a) Method B: by station

(b) Method C: by energy bin

Figure 12: Distributions of point-to-point differences between successive χ^2/dof values after the allowed fit start times ($\chi^2(t_i) - \chi^2(t_{i-1})$).

8 Fit results

Figures 13 through 18 show the fit parameters as a function of energy. For the parameters which are not related to CBO, an ordinary weighted average is used to combine the 22 included detectors. The CBO parameters require more care. CBO amplitudes are small quantities that are always positive. When they are averaged in this way, the result is biased towards larger values since the error bars on the input points are actually symmetric. Consequently, these parameters are rotated by $2\pi/(\text{station}-6)$ radians to align them geometrically with station 6, and the sine and cosine parts are then averaged separately. The amplitude and phase are computed from the combined sine and cosine parts.

It should be noted that all results presented in this section are for only a single random seed. The final R value quoted in Table 1 is averaged over five random seeds. Consequently, there are small apparent discrepancies.

The next set of figures shows fits for each station and energy bin. R and χ^2 are shown for each of the three start time determination methods in Figures 19. For conciseness, the other parameters are shown only for method C in Figures 21 through 24.

Start time consistency plots are shown for each of the results (A, A', B, B', C and C') in Figures 25 through 36. Most of the parameters vary dramatically by energy, so it is necessary to move the values onto the same scale in order to create a reasonable weighted average. Also, in order to avoid artificial inflation of the CBO-related amplitudes from the asymmetric error bars, the sine and cosine components are shown separately. (They are, indeed, the actual fit parameters, and the amplitude and phase are derived from them.) Parameters fall into three categories:

- R, τ, χ^2/dof: these parameters are in principle energy-independent, so they are not transformed.
- N, A, A_{CBO1C}, A_{CBO1S}, A_{CBO2C}, A_{CBO2S}, A_{CBO3C}, A_{CBO3S}: these parameters are amplitudes, and they vary with energy. The values in each energy bin are rescaled to pass through 1 at 49.1 μs, or at the earliest start time for the method if that is later. Consequently, the stability plot indicates *relative* changes.
- ϕ: this parameter is a phase, and it varies with energy. The values in each energy bin are shifted to pass through 0 at 49.1 μs, or at the earliest start time for the method if that is later. The stability plot shows phase changes in units of radians.

The consistency plots for methods A and A' are ordinary start time scans. For the other methods, the data from a station and energy bin is only included at times after the earliest allowed start time for that method. However, so that the statistical error bar increases monotonically with time, the value from the earliest start time is included in all previous points. Consequently, these are "pseudo-start time" scans. The correlated error band that is shown is computed from the standard Kawall formula $\sigma_{AB} = \sqrt{|\sigma_A^2 - \sigma_B^2|}$.

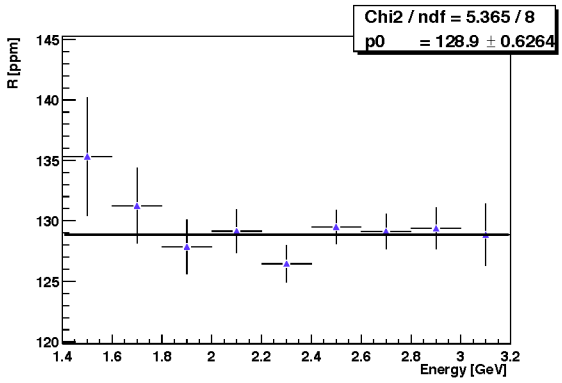

(a) R

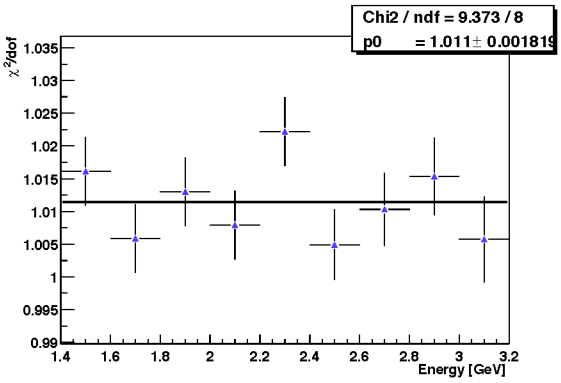

(b) χ^2/dof

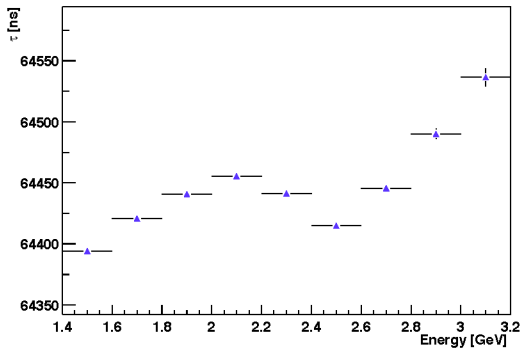

(c) τ

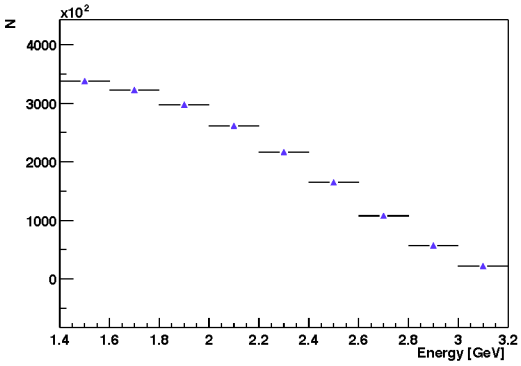

(d) N

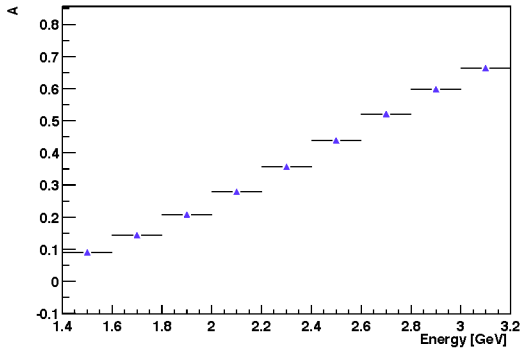

(e) A

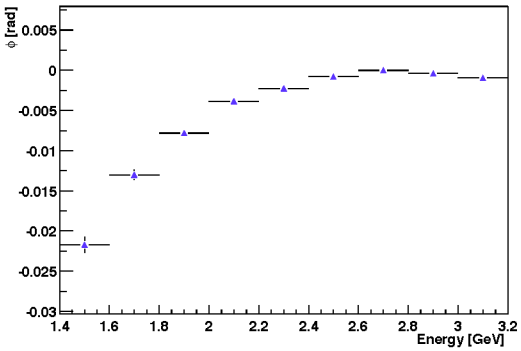

(f) ϕ

Figure 13: Non-CBO parameters as a function of energy for method A (all stations start at 49.1 μs).

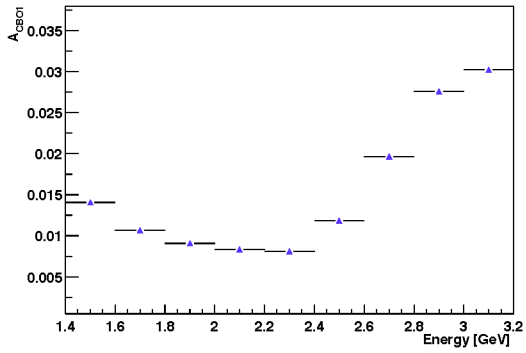

(a) A_{CBO1}

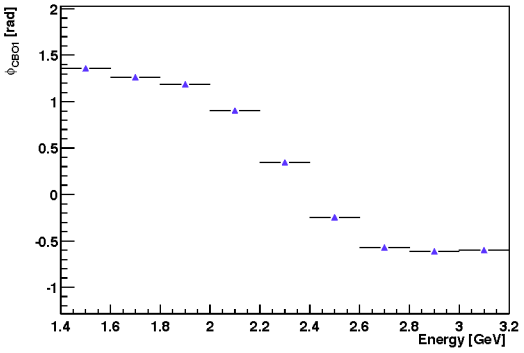

(b) ϕ_{CBO1}

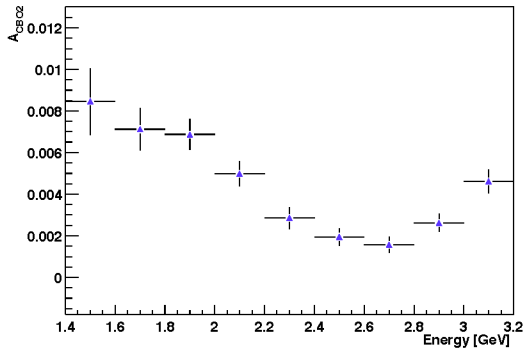

(c) A_{CBO2}

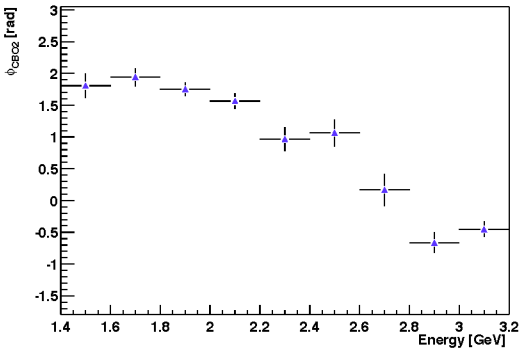

(d) ϕ_{CBO2}

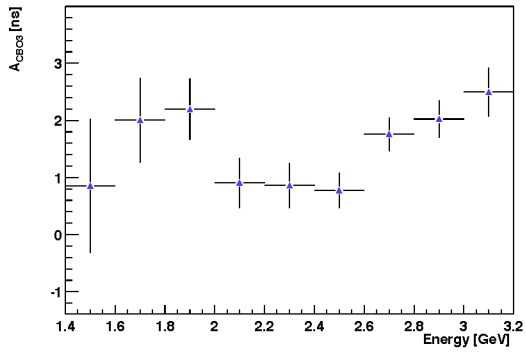

(e) A_{CBO3}

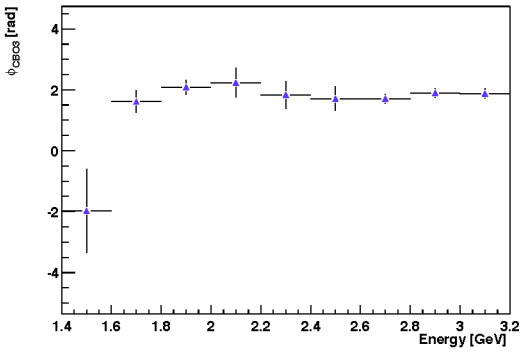

(f) ϕ_{CBO3}

Figure 14: CBO parameters as a function of energy for method A (all stations start at 49.1 μs). Stations have been combined with a vector sum after geometric phase alignment.

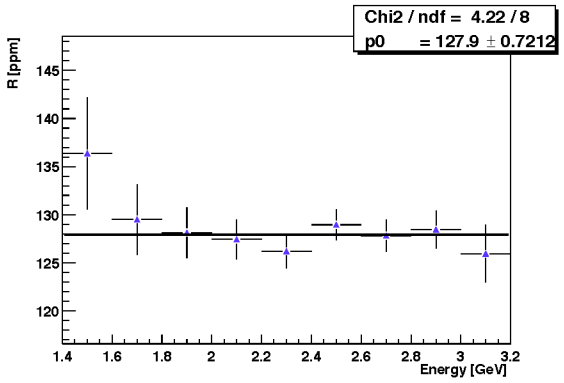

(a) R

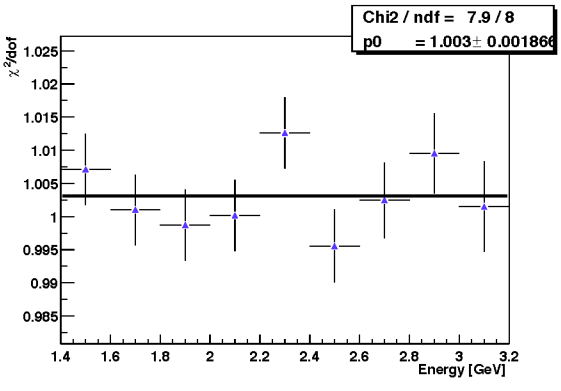

(b) χ^2/dof

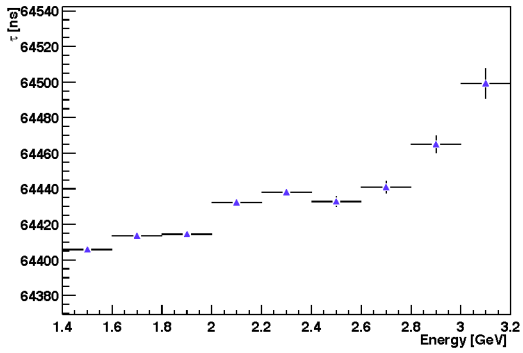

(c) τ

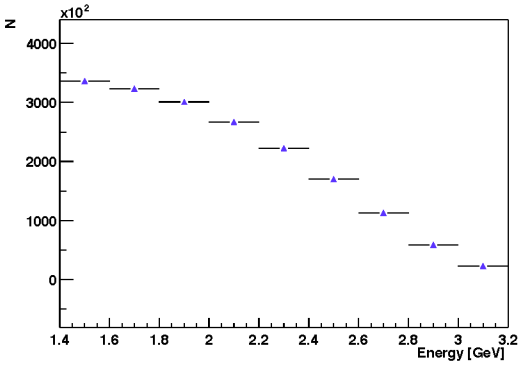

(d) N

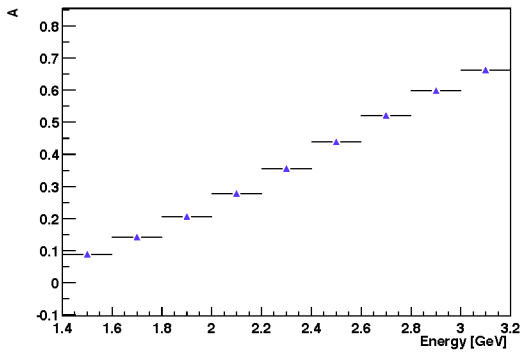

(e) A

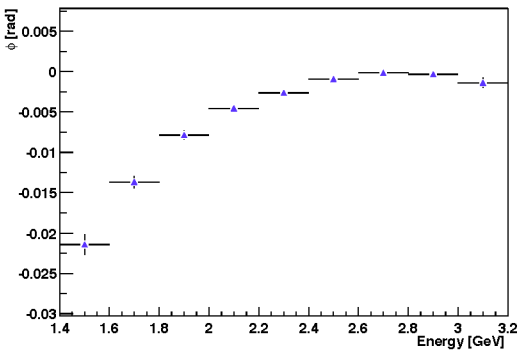

(f) ϕ

Figure 15: Non-CBO parameters as a function of energy for method B (each station at its own start time).

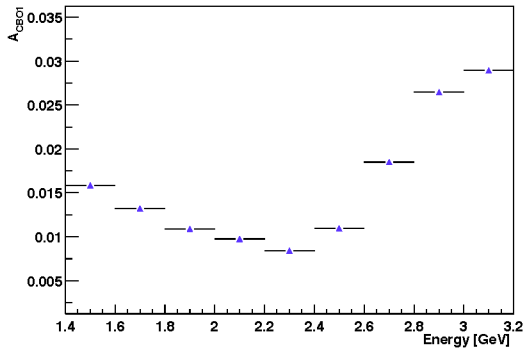

(a) A_{CBO1}

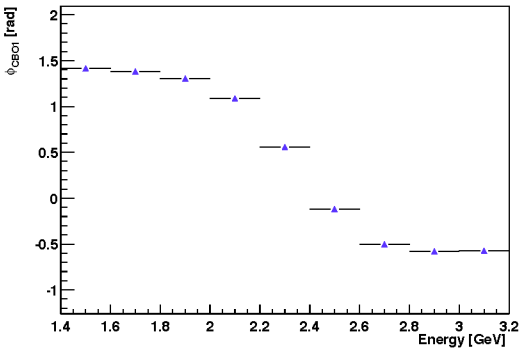

(b) ϕ_{CBO1}

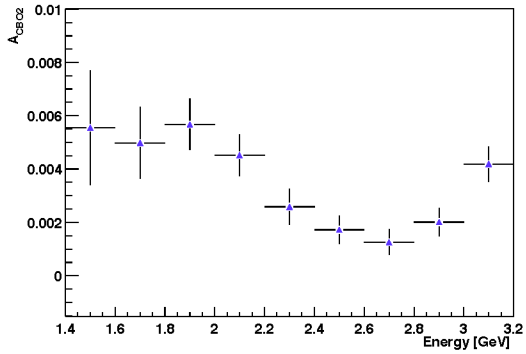

(c) A_{CBO2}

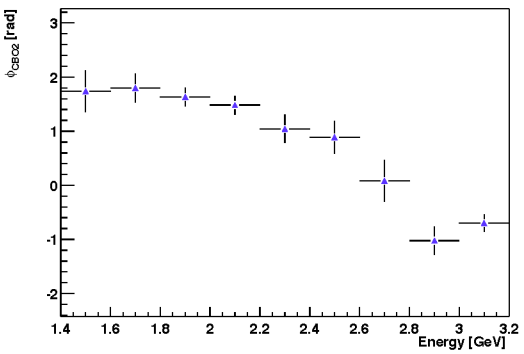

(d) ϕ_{CBO2}

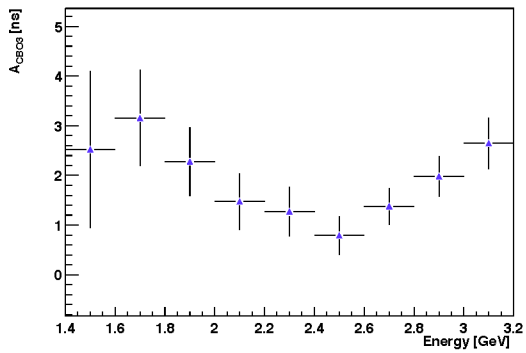

(e) A_{CBO3}

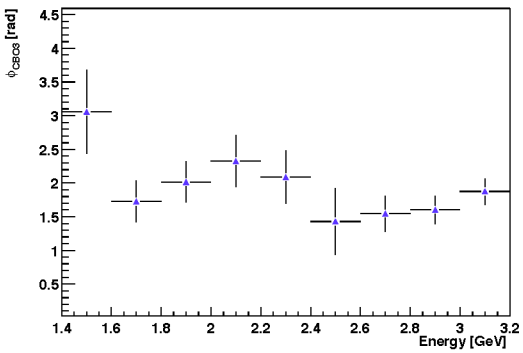

(f) ϕ_{CBO3}

Figure 16: CBO parameters as a function of energy for method B (each station at its own start time). Stations have been combined with a vector sum after geometric phase alignment.

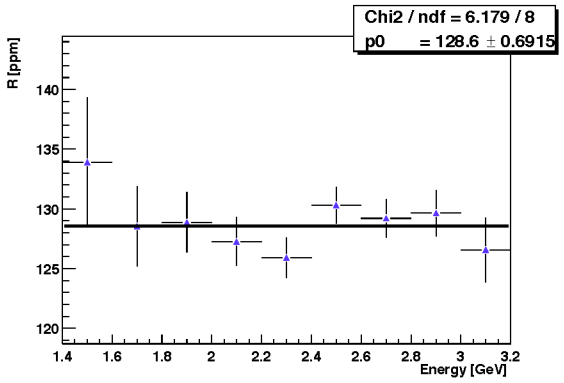

(a) R

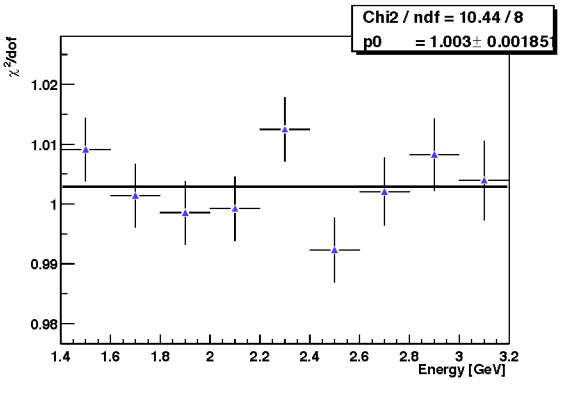

(b) χ^2/dof

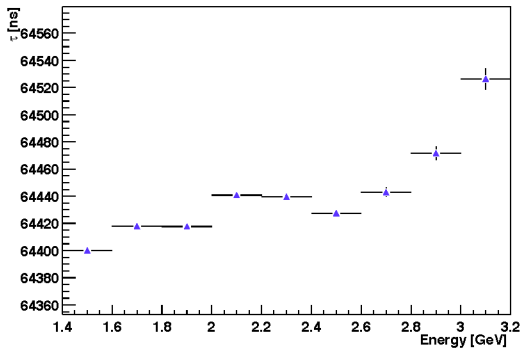

(c) τ

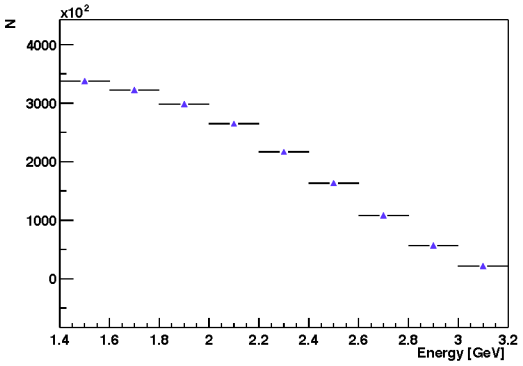

(d) N

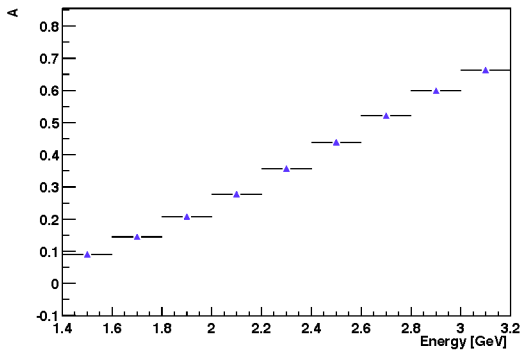

(e) A

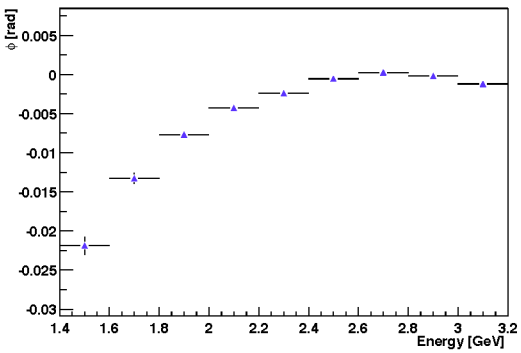

(f) ϕ

Figure 17: Non-CBO parameters as a function of energy for method C (each energy bin at its own start time).

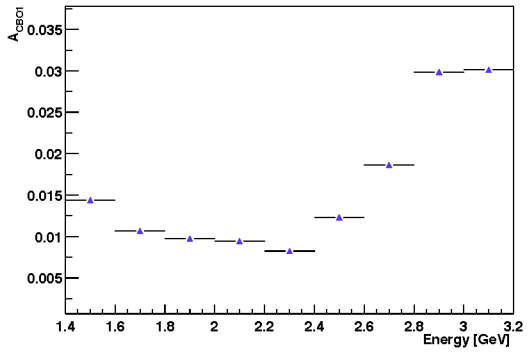

(a) A_{CBO1}

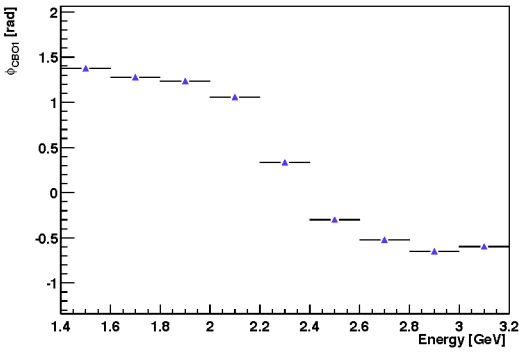

(b) ϕ_{CBO1}

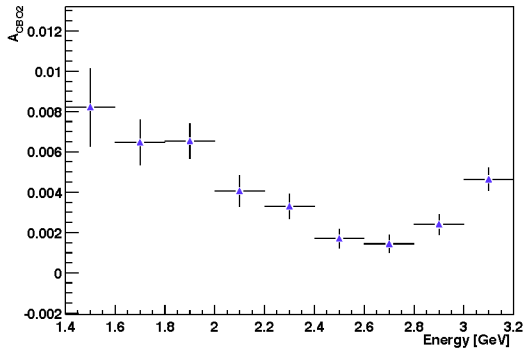

(c) A_{CBO2}

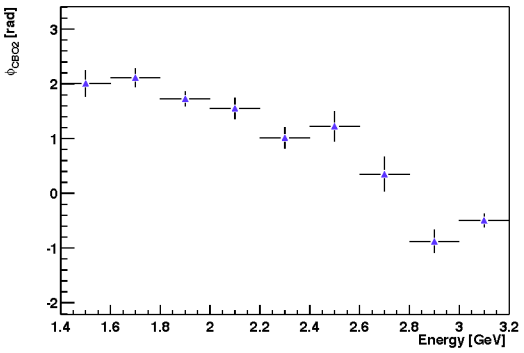

(d) ϕ_{CBO2}

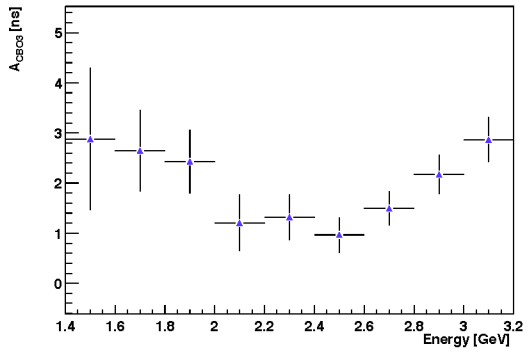

(e) A_{CBO3}

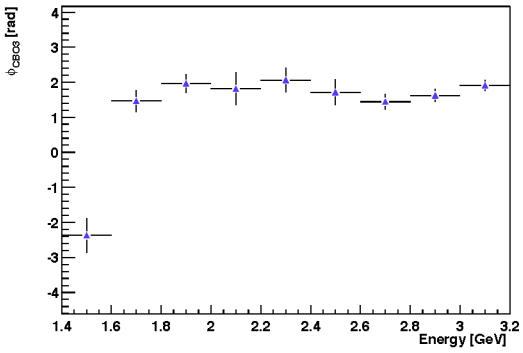

(f) ϕ_{CBO3}

Figure 18: CBO parameters as a function of energy for method C (each energy bin at its own start time). Stations have been combined with a vector sum after geometric phase alignment.

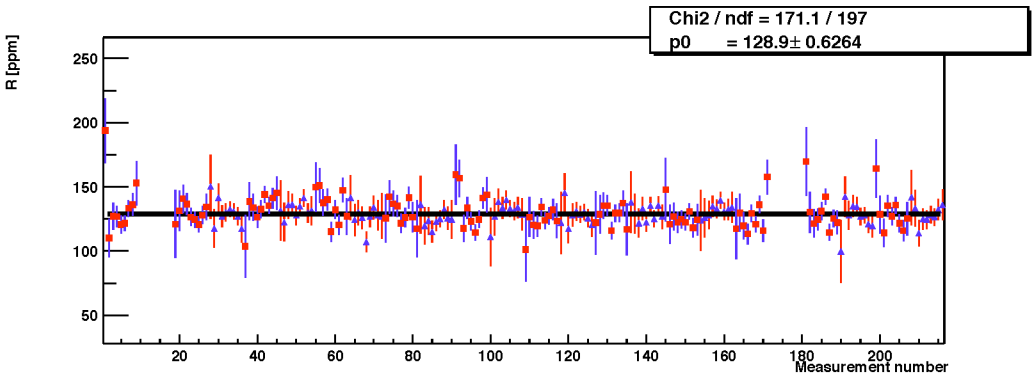

(a) R (method A)

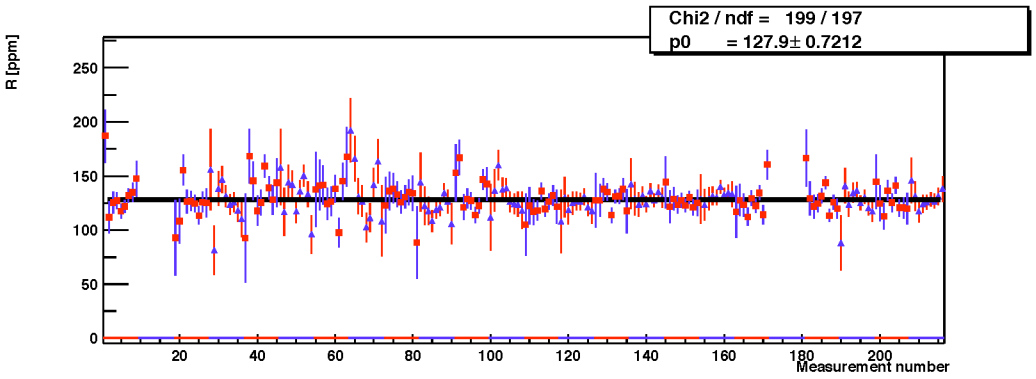

(b) R (method B)

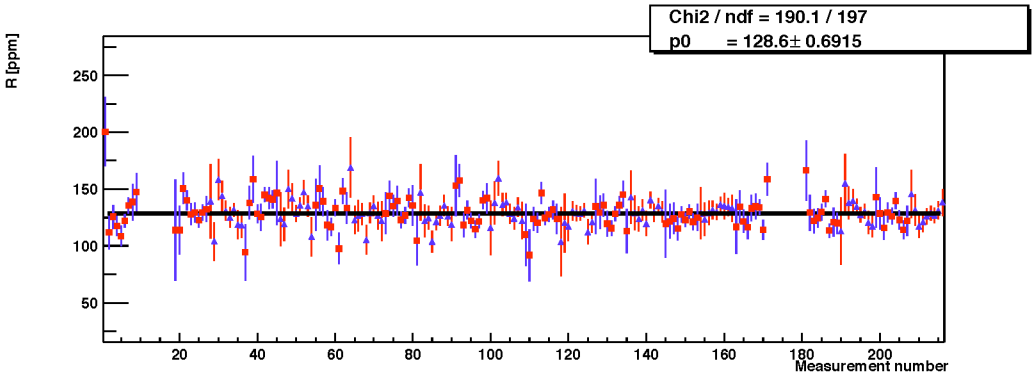

(c) R (method C)

Figure 19: R for fits by energy bin, for each station and energy bin.

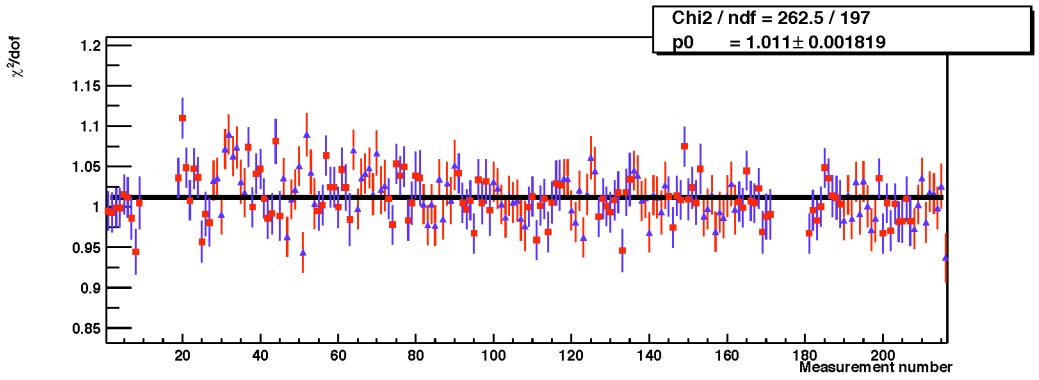

(a) χ^2/dof (method A)

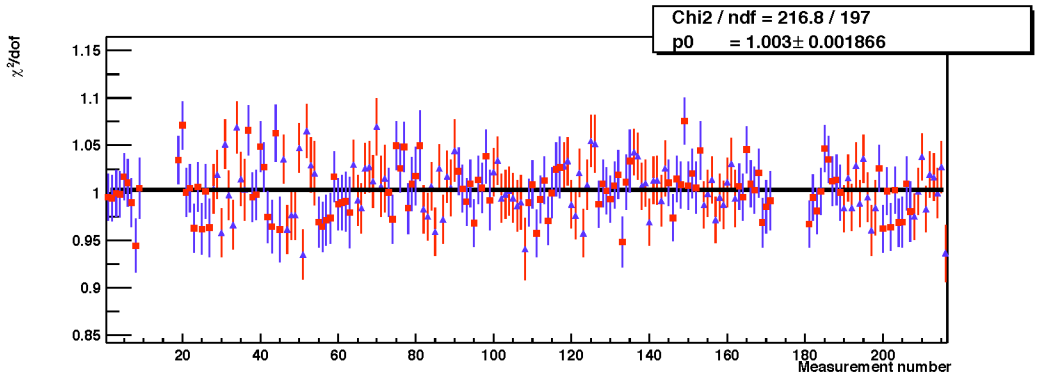

(b) χ^2/dof (method B)

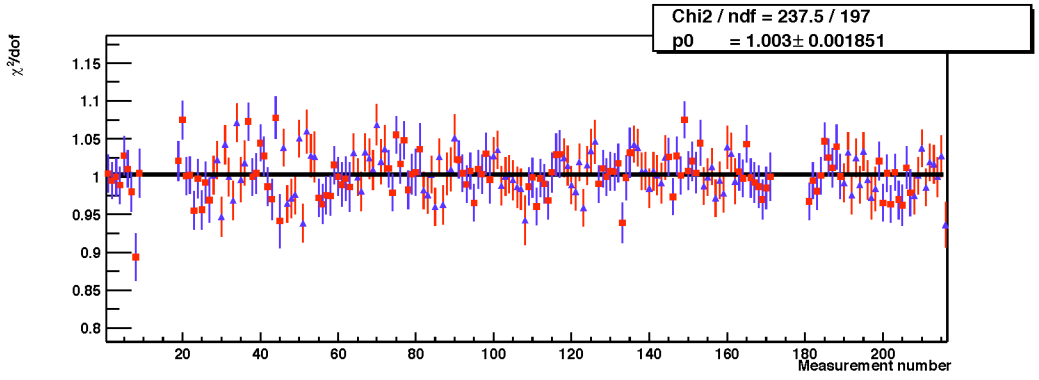

(c) χ^2/dof (method C)

Figure 20: χ^2/dof for fits by energy bin, for each station and energy bin.

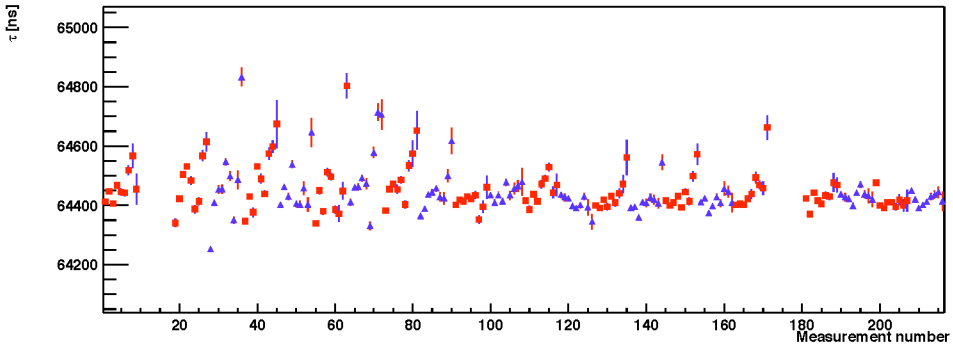

(a) τ

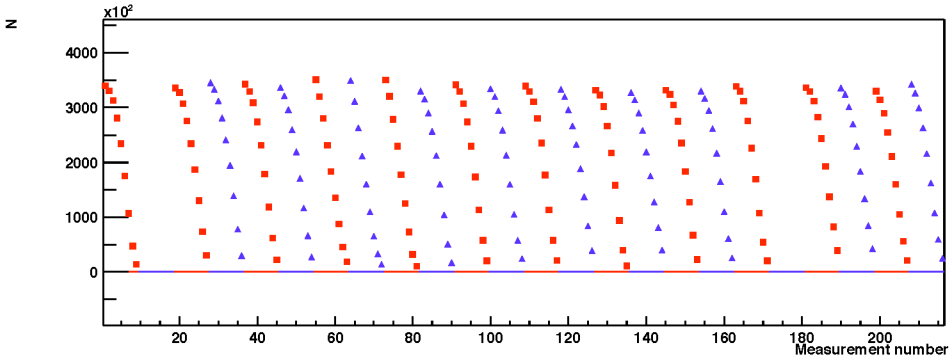

(b) N

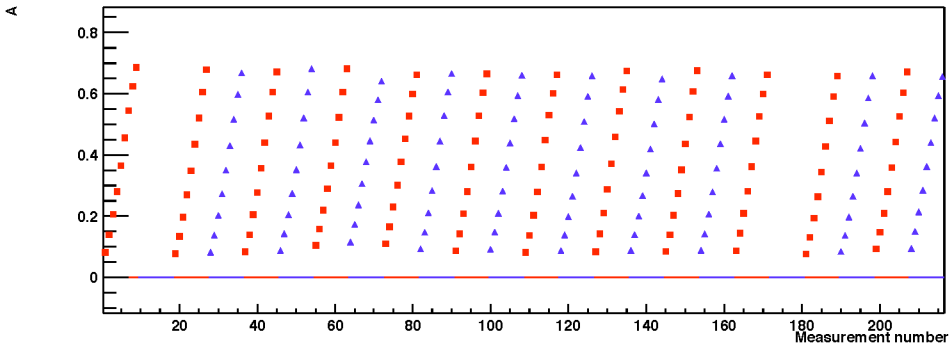

(c) A

Figure 21: τ, N, and A for fits by energy bin, for each station and energy bin (method C).

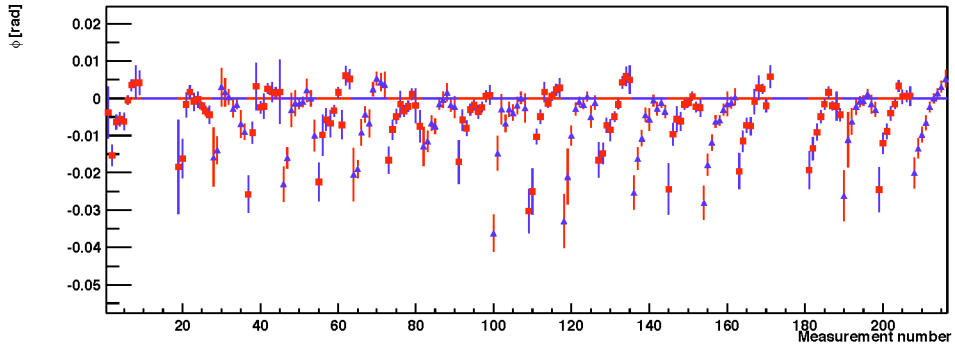

(a) ϕ

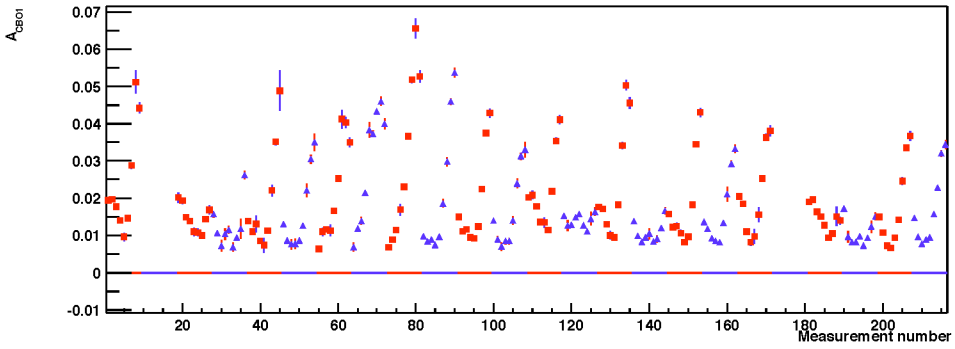

(b) A_{CBO1}

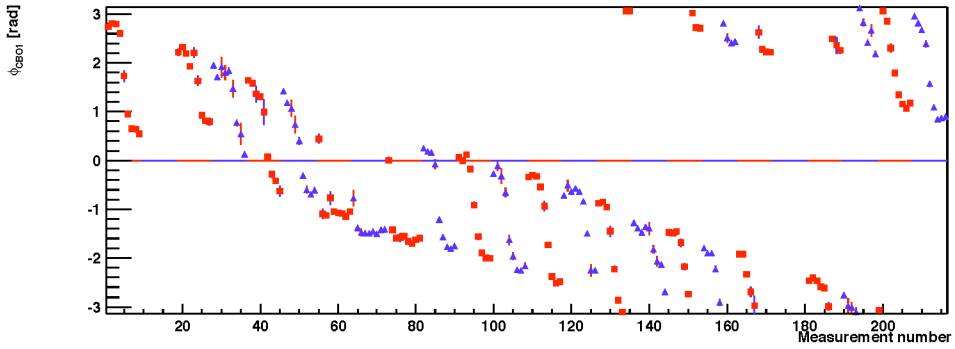

(c) ϕ_{CBO1}

Figure 22: ϕ, A_{CBO1}, and ϕ_{CBO1} for fits by energy bin, for each station and energy bin (method C).

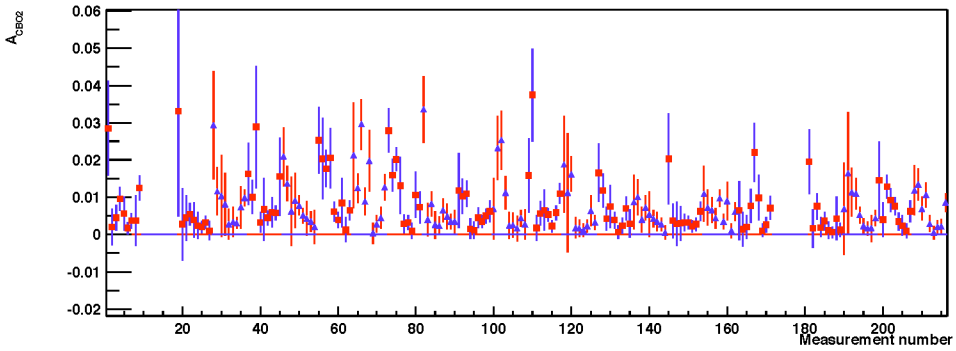

(a) A_{CBO2}

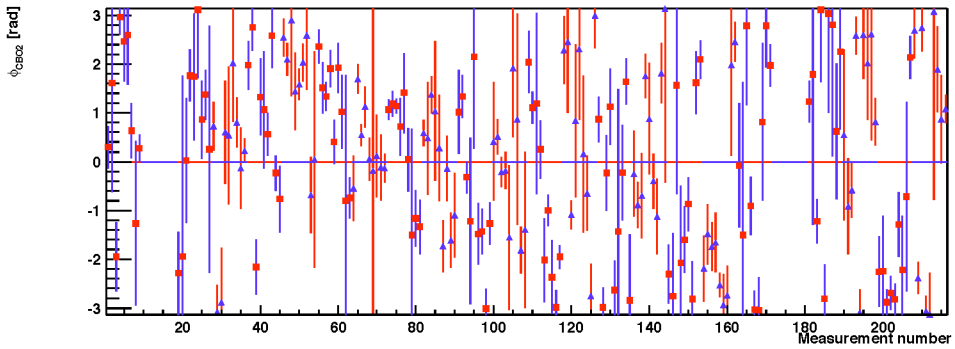

(b) ϕ_{CBO2}

Figure 23: A_{CBO2} and ϕ_{CBO2} for fits by energy bin, for each station and energy bin (method C)

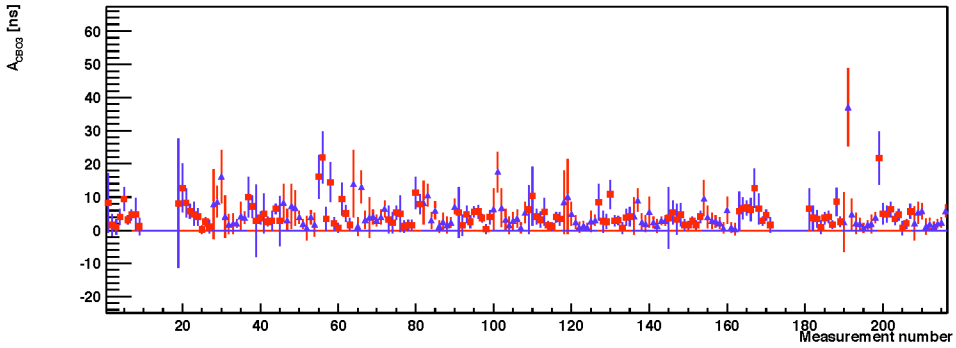

(a) A_{CBO3}

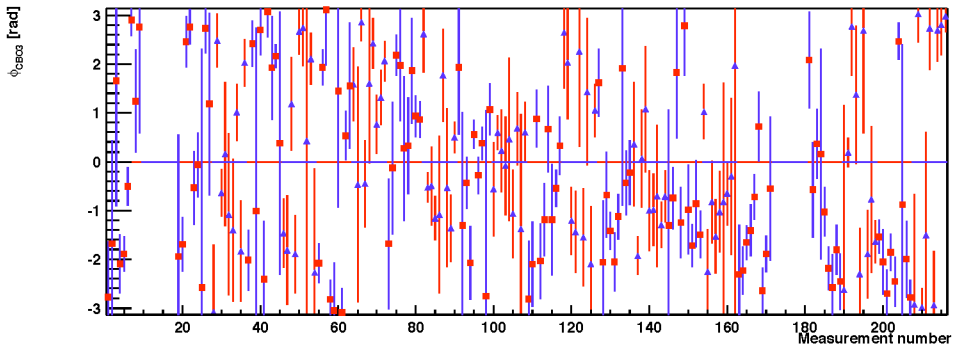

(b) ϕ_{CBO3}

Figure 24: A_{CBO3} and ϕ_{CBO3} for fits by energy bin, for each station and energy bin (method C)

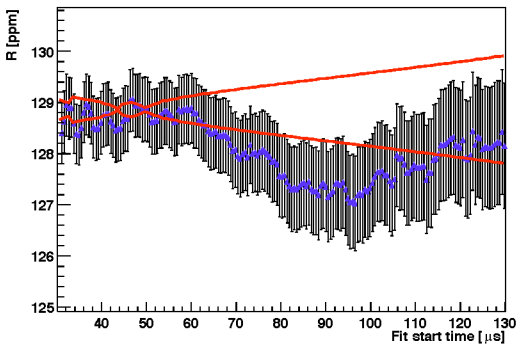

(a) R (method A)

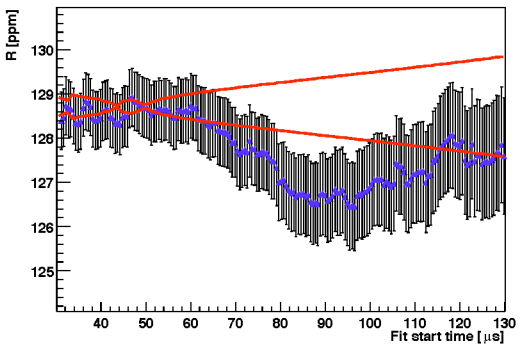

(b) R (method A')

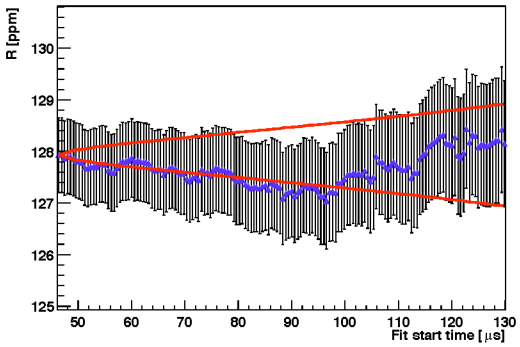

(c) R (method B)

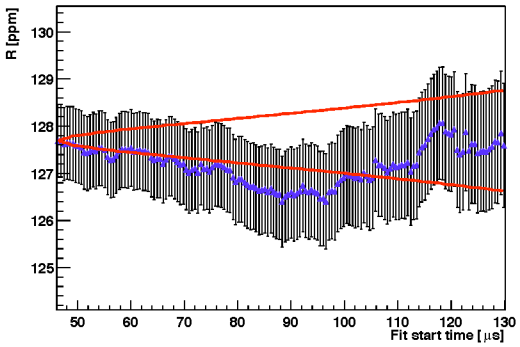

(d) R (method B')

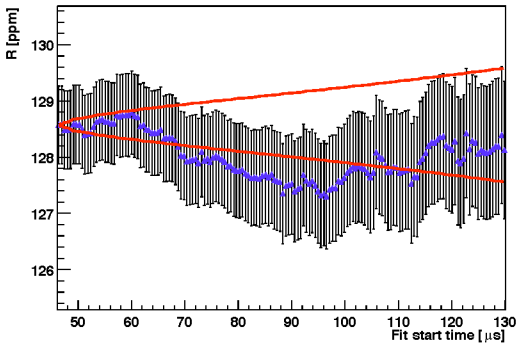

(e) R (method C)

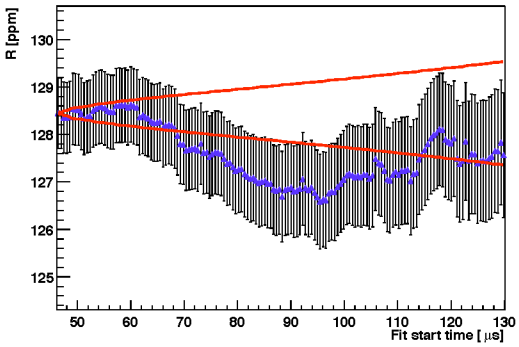

(f) R (method C')

Figure 25: (Pseudo-)start time scans for R, for various start time methods.

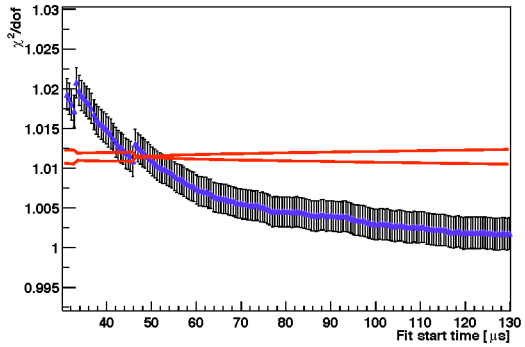

(a) χ^2/dof (method A)

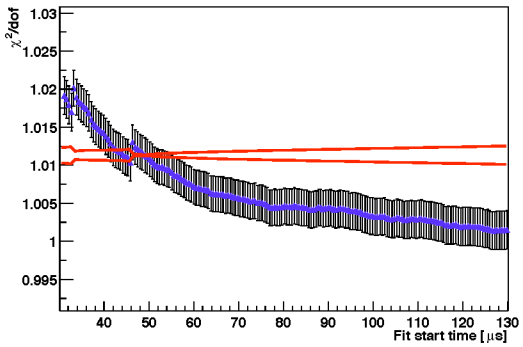

(b) χ^2/dof (method A')

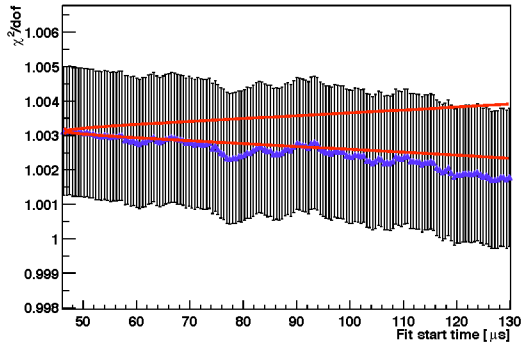

(c) χ^2/dof (method B)

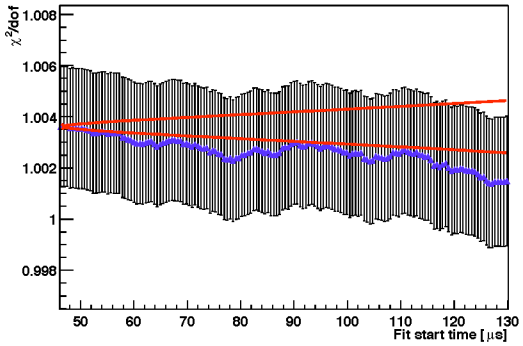

(d) χ^2/dof (method B')

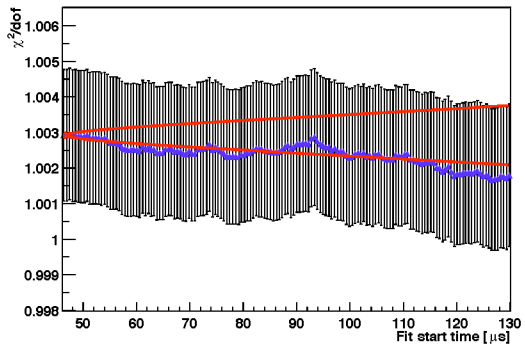

(e) χ^2/dof (method C)

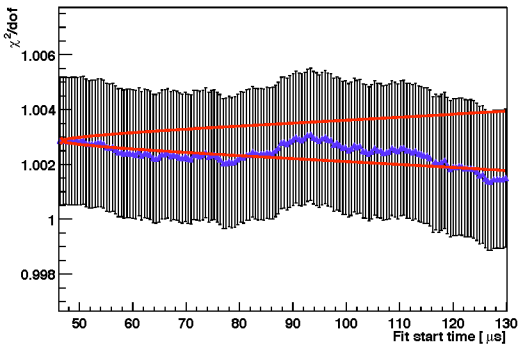

(f) χ^2/dof (method C')

Figure 26: (Pseudo-)start time scans for χ^2/dof, for various start time methods.

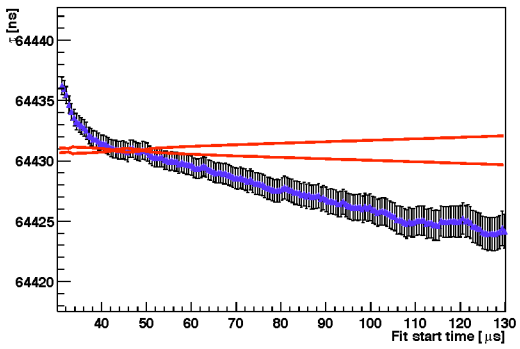

(a) τ (method A)

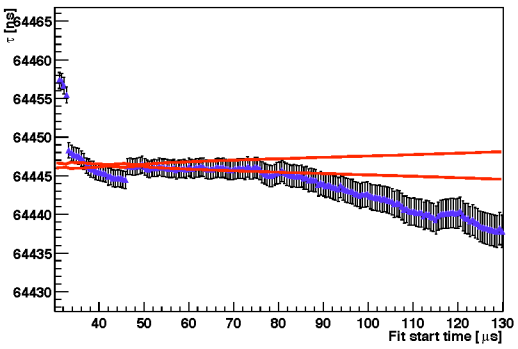

(b) τ (method A')

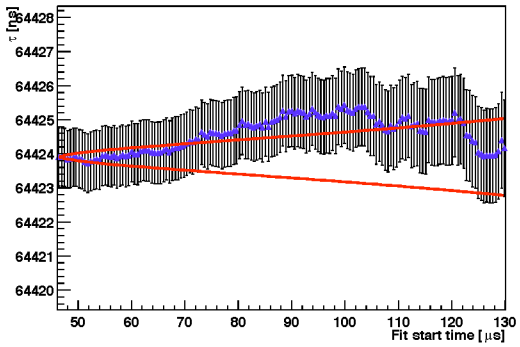

(c) τ (method B)

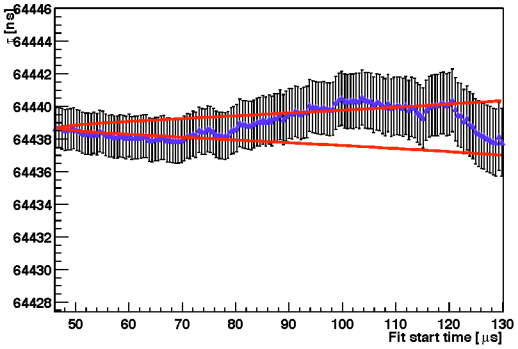

(d) τ (method B')

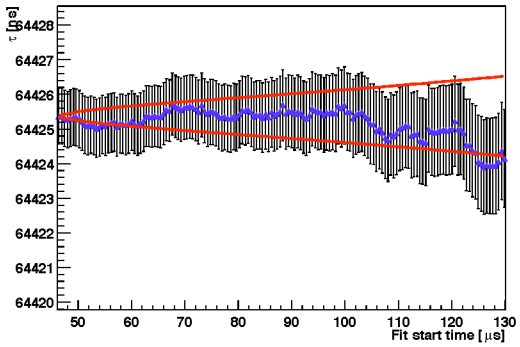

(e) τ (method C)

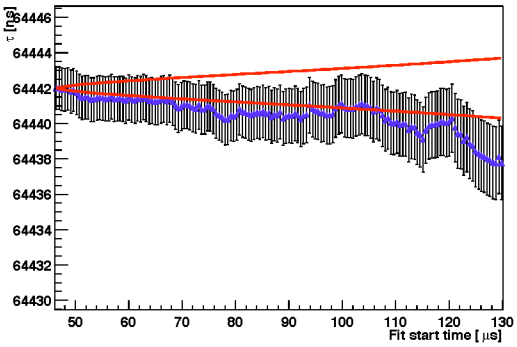

(f) τ (method C')

Figure 27: (Pseudo-)start time scans for τ, for various start time methods.

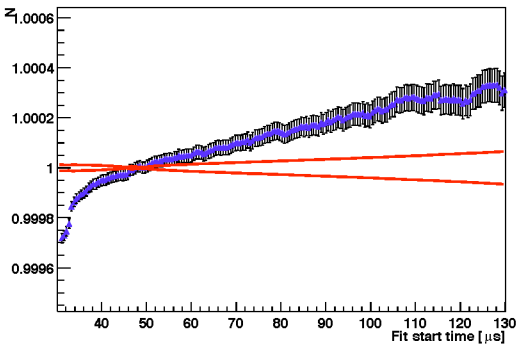

(a) N (method A)

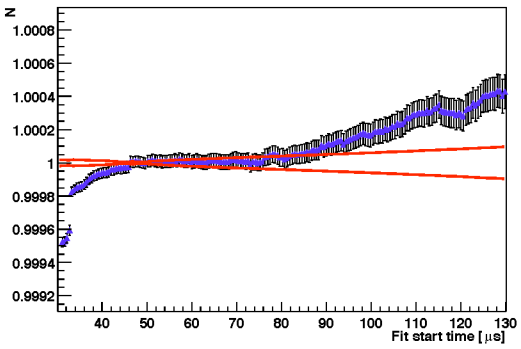

(b) N (method A')

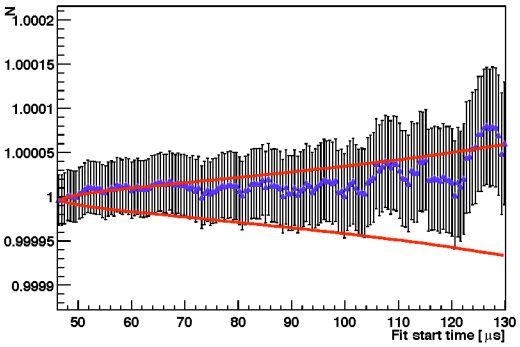

(c) N (method B)

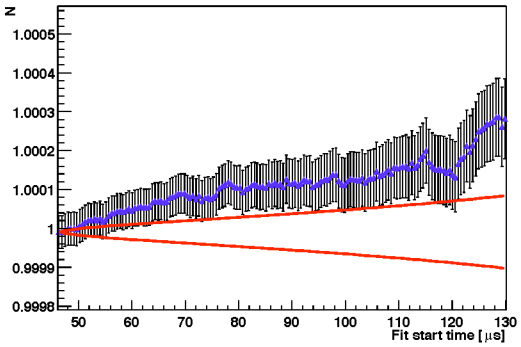

(d) N (method B')

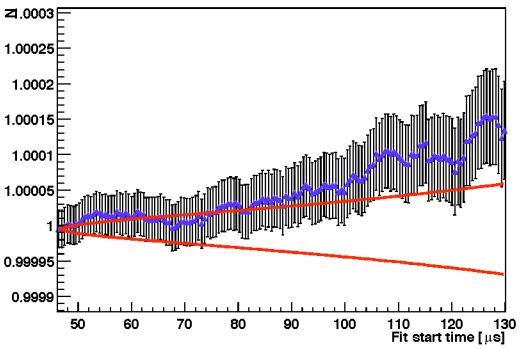

(e) N (method C)

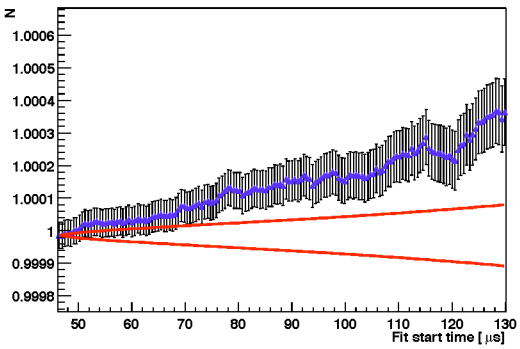

(f) N (method C')

Figure 28: (Pseudo-)start time scans for N, for various start time methods.

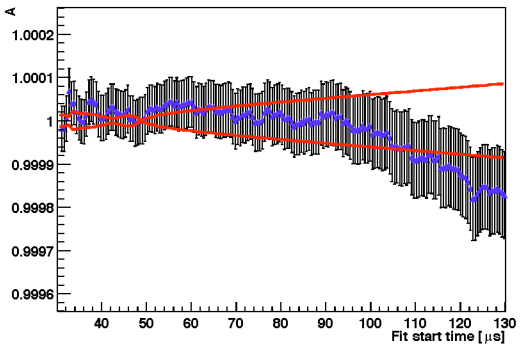

(a) A (method A)

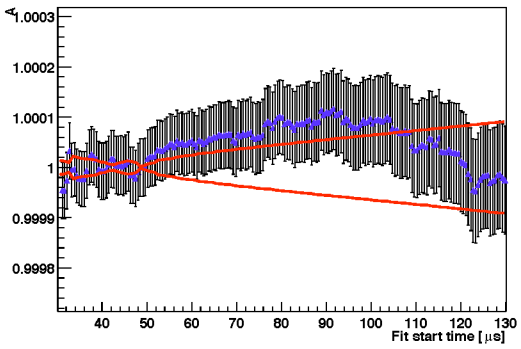

(b) A (method A')

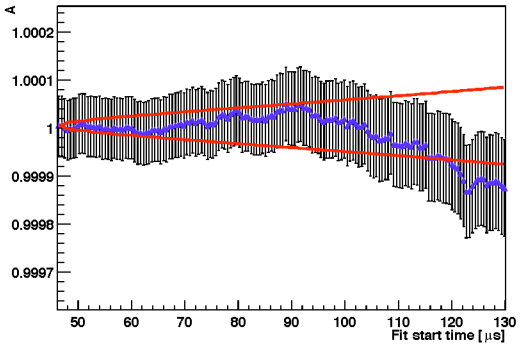

(c) A (method B)

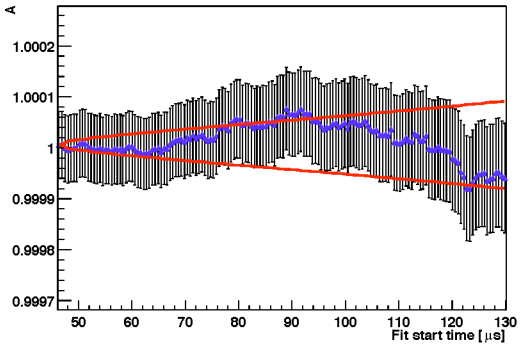

(d) A (method B')

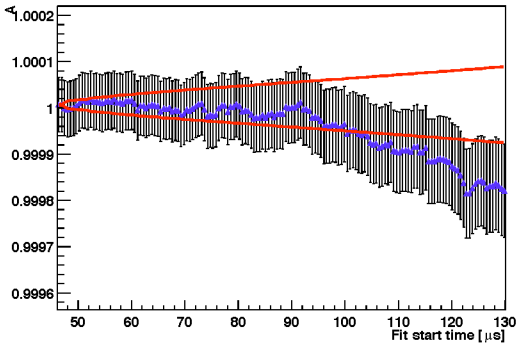

(e) A (method C)

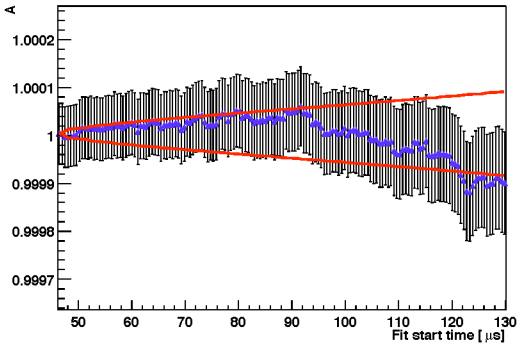

(f) A (method C')

Figure 29: (Pseudo-)start time scans for A, for various start time methods.

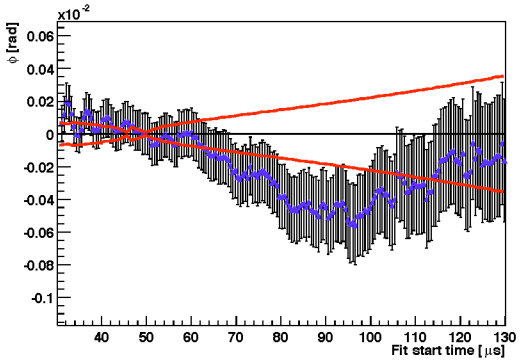

(a) ϕ (method A)

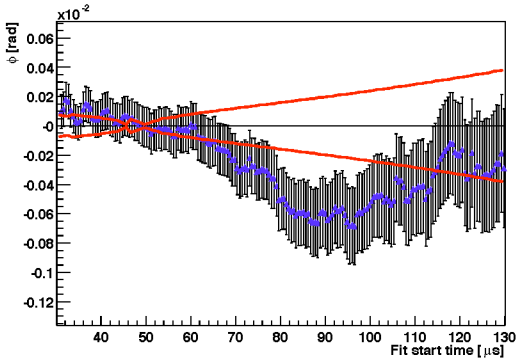

(b) ϕ (method A')

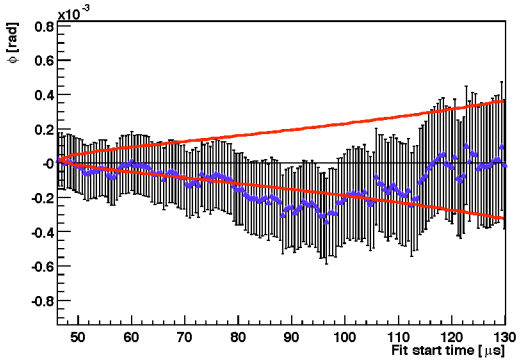

(c) ϕ (method B)

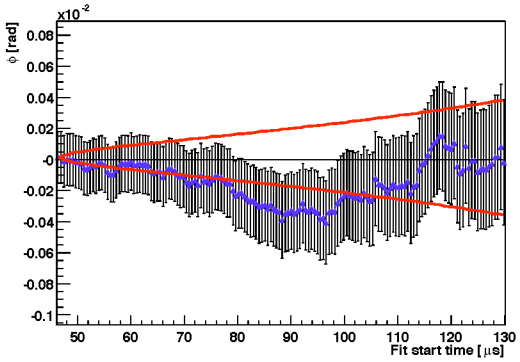

(d) ϕ (method B')

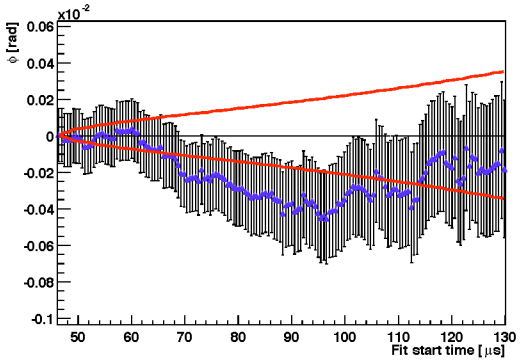

(e) ϕ (method C)

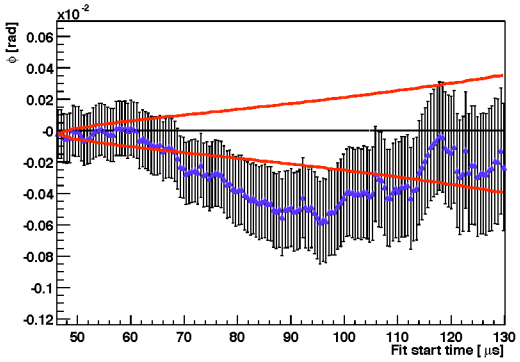

(f) ϕ (method C')

Figure 30: (Pseudo-)start time scans for ϕ, for various start time methods.

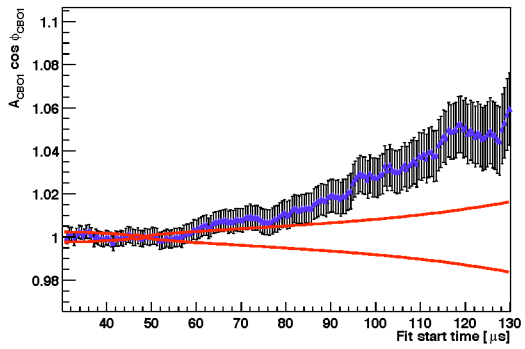

(a) A_{CBO1C} (method A)

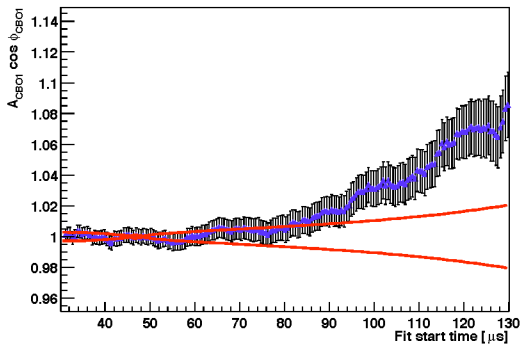

(b) A_{CBO1C} (method A')

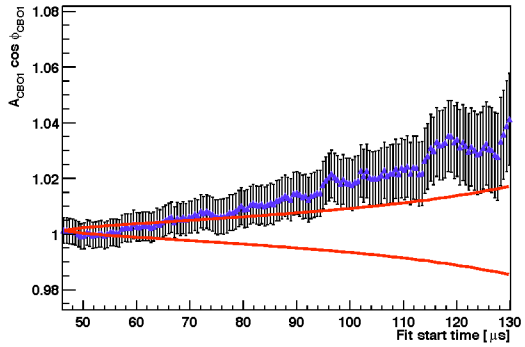

(c) A_{CBO1C} (method B)

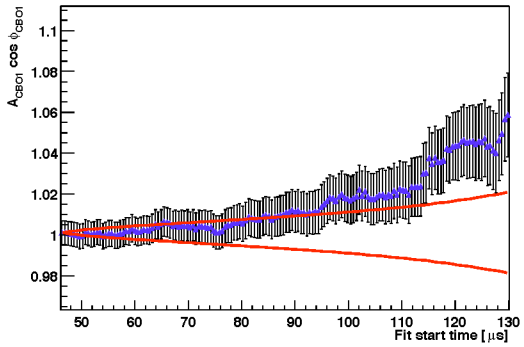

(d) A_{CBO1C} (method B')

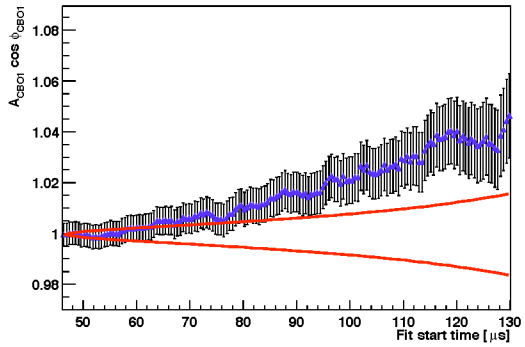

(e) A_{CBO1C} (method C)

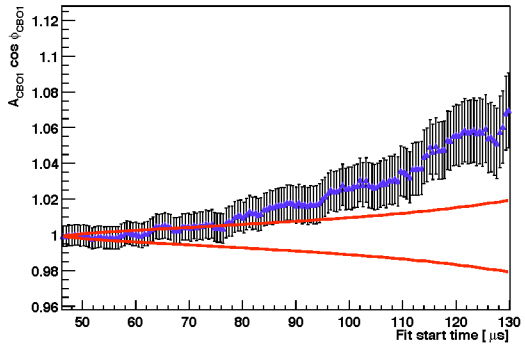

(f) A_{CBO1C} (method C')

Figure 31: (Pseudo-)start time scans for A_{CBO1C}, for various start time methods.

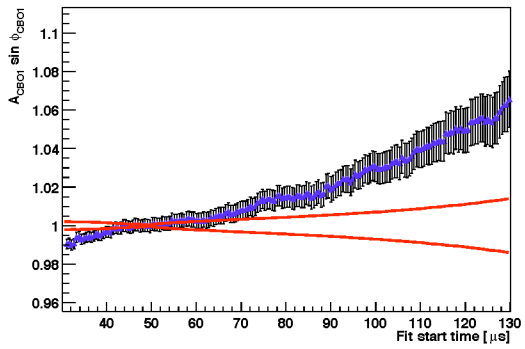

(a) A_{CBO1S} (method A)

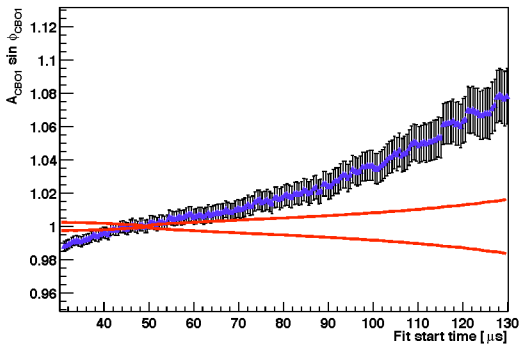

(b) A_{CBO1S} (method A')

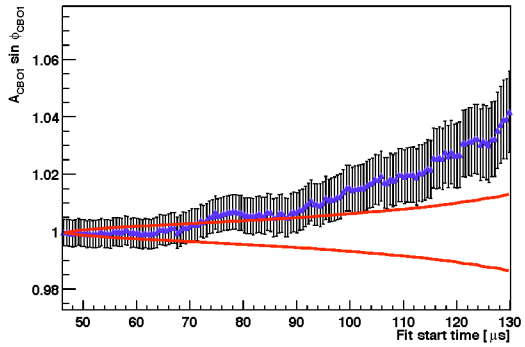

(c) A_{CBO1S} (method B)

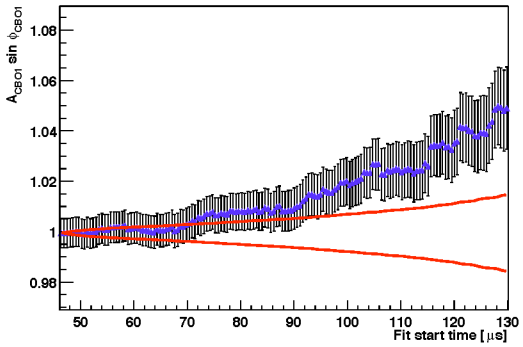

(d) A_{CBO1S} (method B')

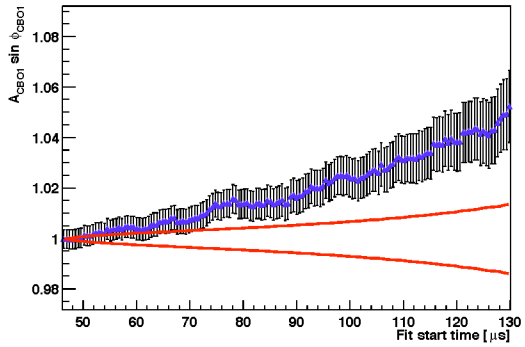

(e) A_{CBO1S} (method C)

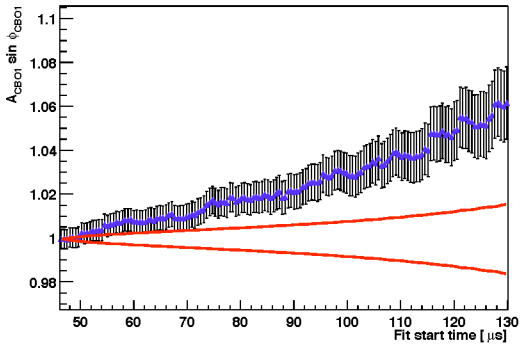

(f) A_{CBO1S} (method C')

Figure 32: (Pseudo-)start time scans for A_{CBO1S}, for various start time methods.

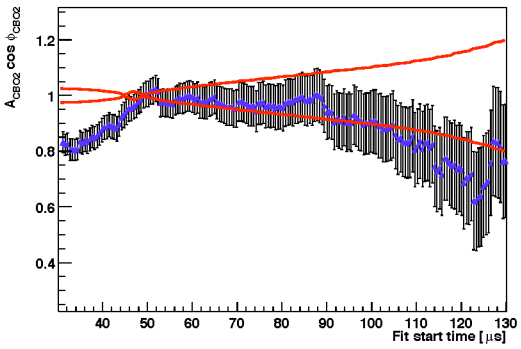

(a) A_{CBO2C} (method A)

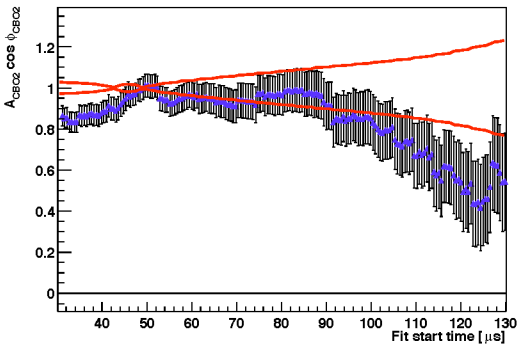

(b) A_{CBO2C} (method A')

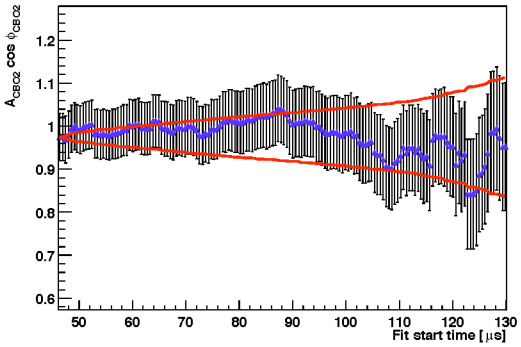

(c) A_{CBO2C} (method B)

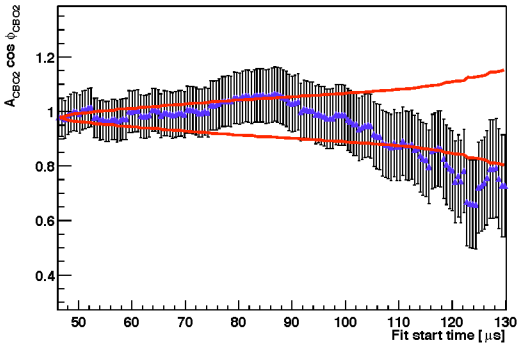

(d) A_{CBO2C} (method B')

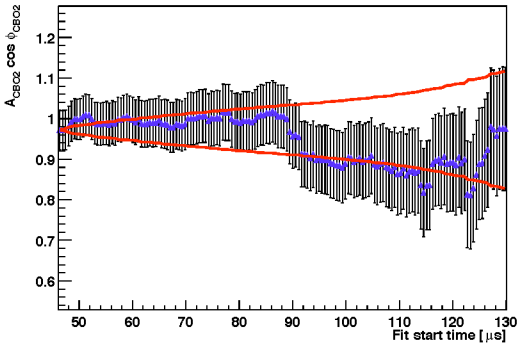

(e) A_{CBO2C} (method C)

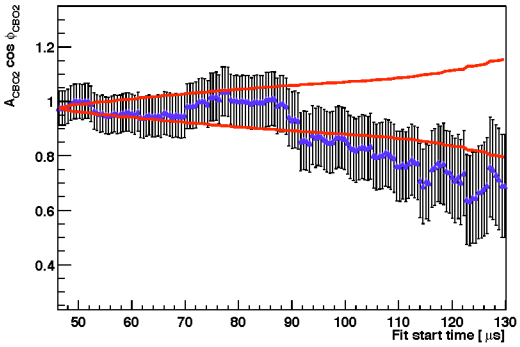

(f) A_{CBO2C} (method C')

Figure 33: (Pseudo-)start time scans for A_{CBO2C}, for various start time methods.

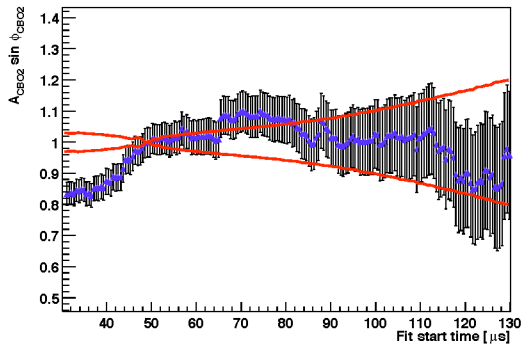

(a) A_{CBO2S} (method A)

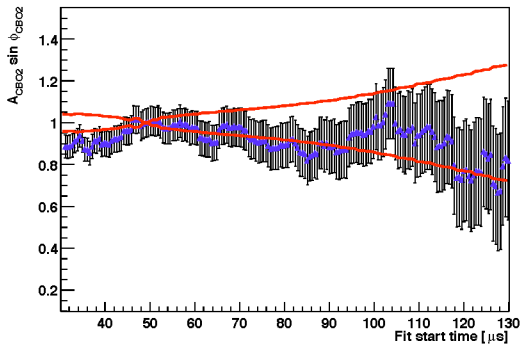

(b) A_{CBO2S} (method A')

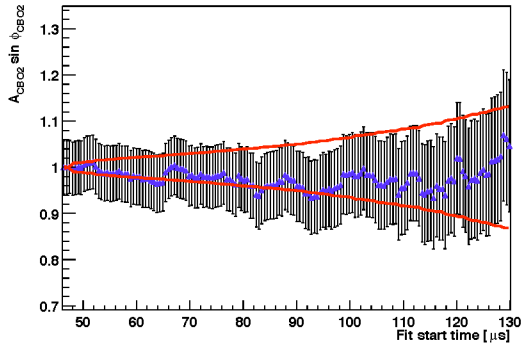

(c) A_{CBO2S} (method B)

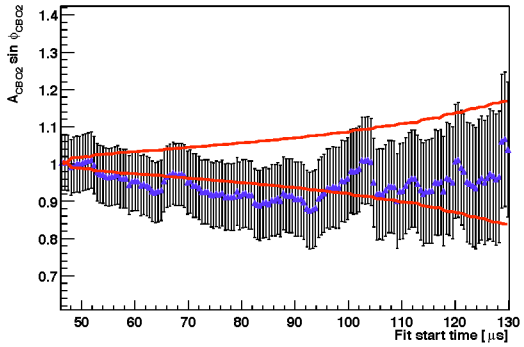

(d) A_{CBO2S} (method B')

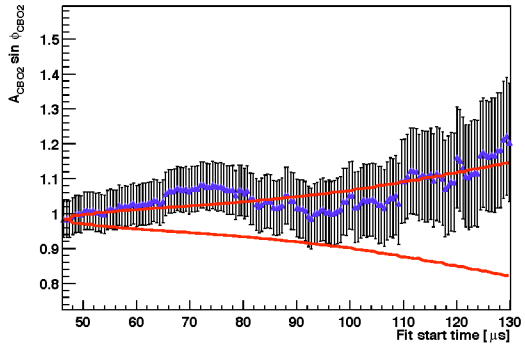

(e) A_{CBO2S} (method C)

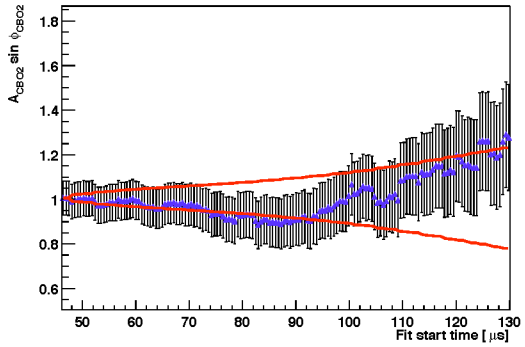

(f) A_{CBO2S} (method C')

Figure 34: (Pseudo-)start time scans for A_{CBO2S}, for various start time methods.

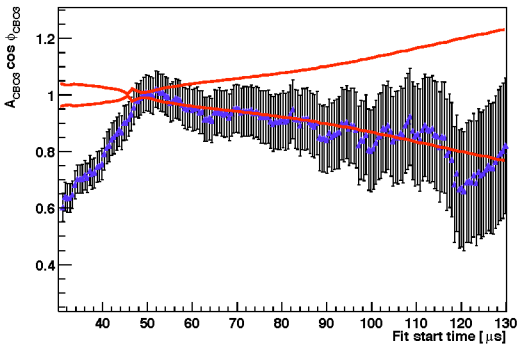

(a) A_{CBO3C} (method A)

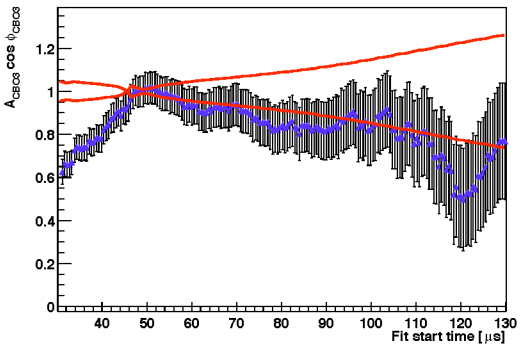

(b) A_{CBO3C} (method A')

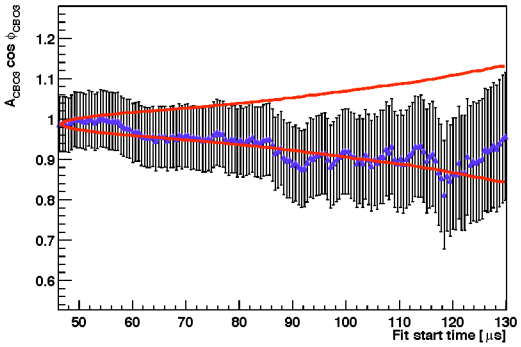

(c) A_{CBO3C} (method B)

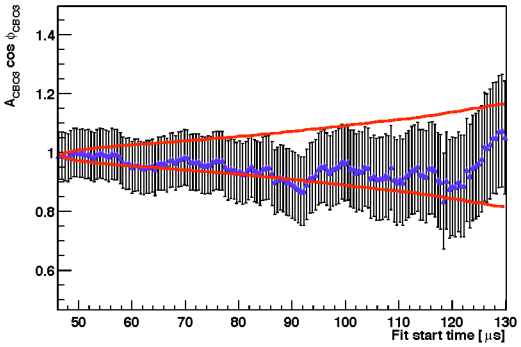

(d) A_{CBO3C} (method B')

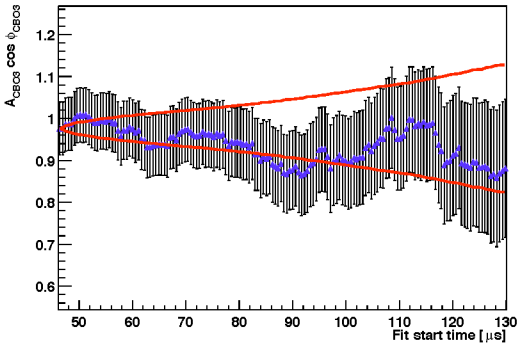

(e) A_{CBO3C} (method C)

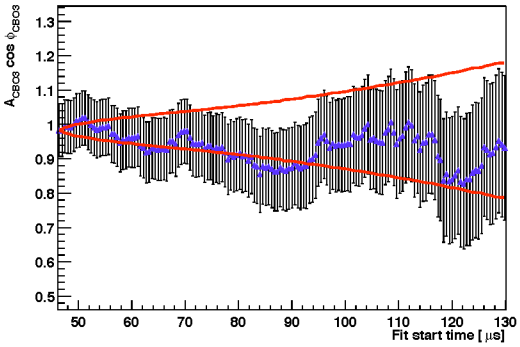

(f) A_{CBO3C} (method C')

Figure 35: (Pseudo-)start time scans for A_{CBO3C}, for various start time methods.

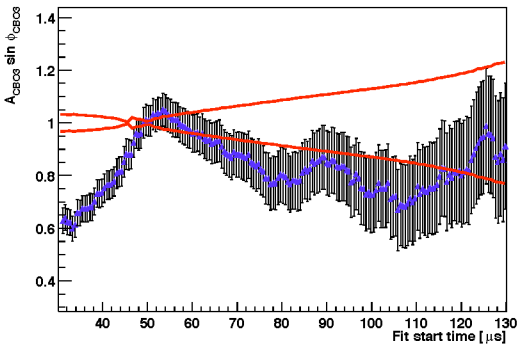

(a) A_{CBO3S} (method A)

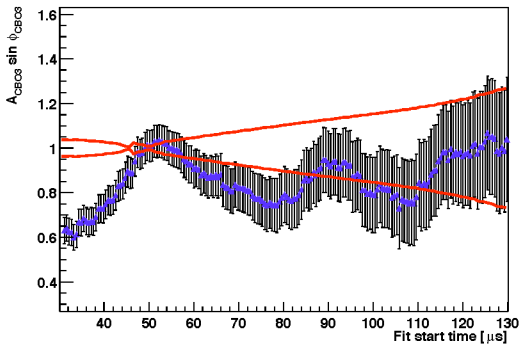

(b) A_{CBO3S} (method A')

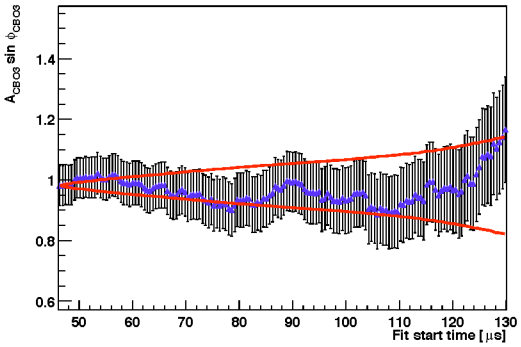

(c) A_{CBO3S} (method B)

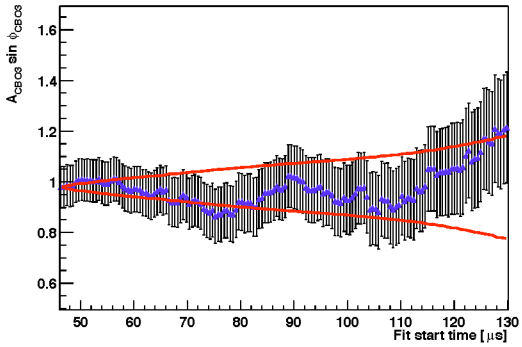

(d) A_{CBO3S} (method B')

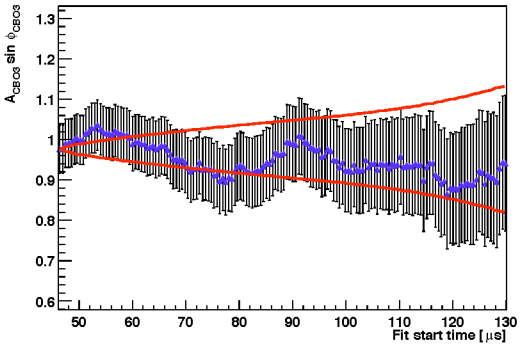

(e) A_{CBO3S} (method C)

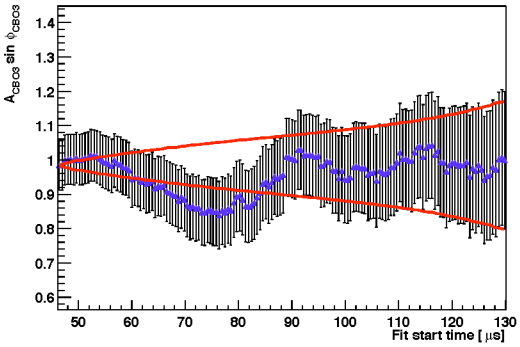

(f) A_{CBO3S} (method C')

Figure 36: (Pseudo-)start time scans for A_{CBO3S}, for various start time methods.

Figure 37 shows the distributions of point-to-point differences between R values at consecutive fit start times, normalized to the correlated error. The distributions are all centered at 0, suggesting that there is not a statistically significant trend to lower values versus fit start time. However, the distributions are approximately 10 percent too wide (they should have an RMS of 1), and they are not quite Gaussian. This is typically the signature of phase pulling.

Similar plots were examined for the R value after combining the 198 separate fits. They show the same features, only with much lower statistics.

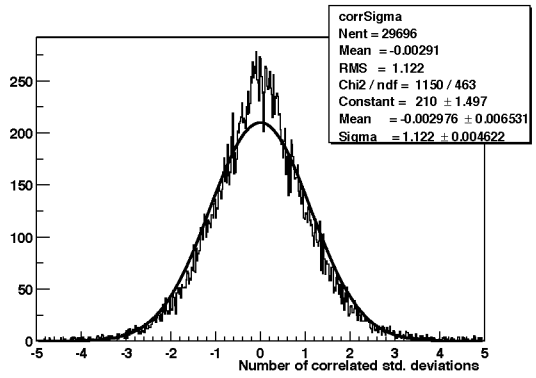

(a) Method A

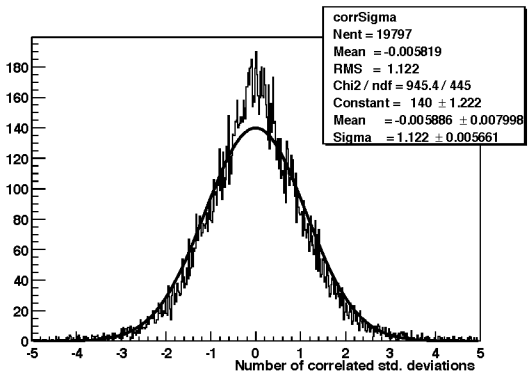

(b) Method A'

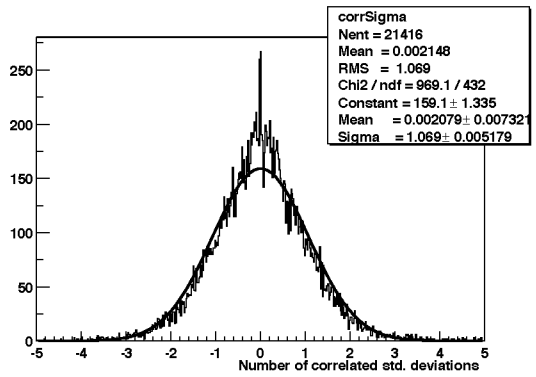

(c) Method B

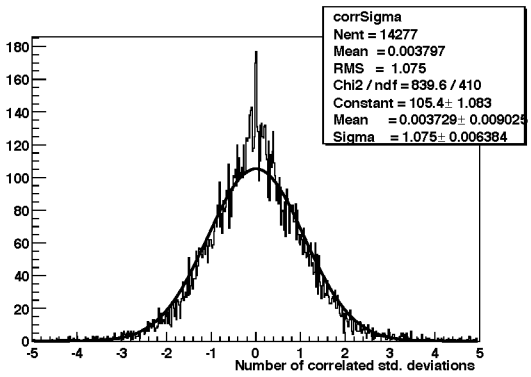

(d) Method B'

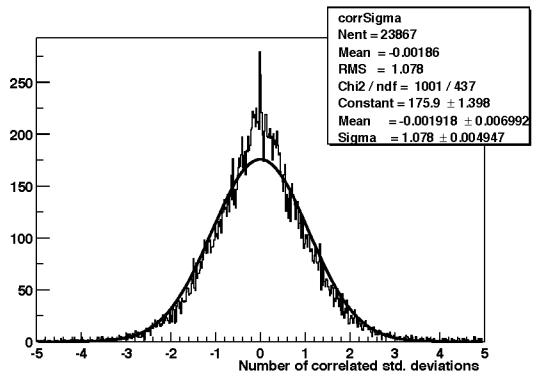

(e) Method C

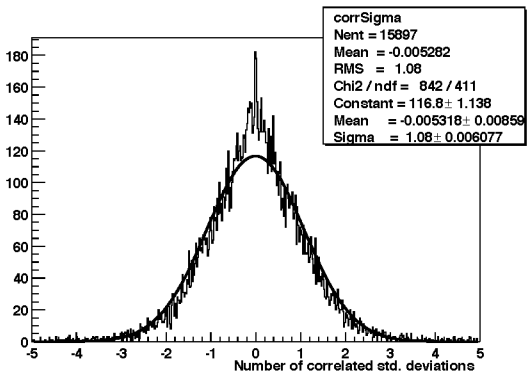

(f) Method C'

Figure 37: Distributions of point-to-point differences between R values at successive fit start times in each energy bin, normalized to the correlated error.

9 Half-ring effects

The systematic uncertainties from the half-ring effects (CBO modulations of the $g-2$ asymmetry and phase) are absorbed as an increased statistical error because they are included in the fitting function.

The alternative approach, neglecting the half-ring effects and attributing a systematic uncertainty to them, was considered and rejected. The cancellation of the effects from averaging around the ring is not sufficiently complete.

Cancellation factors were obtained by taking a weighted average of the sine and cosine parts of the CBO amplitude. The factor is computed by taking the ratio of the combined amplitude for half the ring to the combined amplitude for the entire ring:

$$f_c = \frac{\sqrt{(< A\cos\phi >_{1-24})^2 + (< A\sin\phi >_{1-24})^2}}{\frac{1}{2}(\sqrt{(< A\cos\phi >_{1-12})^2 + (< A\sin\phi >_{1-12})^2} + \sqrt{(< A\cos\phi >_{13-24})^2 + (< A\sin\phi >_{13-24})^2})}$$

The weighted average for each parameter (generically called P) is done according to the uncertainty on R as follows:

$$< P >= \frac{\sum_{i\in\text{Energy}} \sum_{j\in\text{Station}} \frac{P_{ij}}{\delta R_{ij}}}{\sum_{i\in\text{Energy}} \sum_{j\in\text{Station}} \frac{1}{\delta R_{ij}}}$$

The cancellation factors that were found are shown in Table 4. They are quite large. Bill Morse has pointed out that they are dominated by resolution effects, and that this study therefore represents an upper limit on the possible systematic error.

Figure 38 illustrates the half-ring effect for various fitting functions; the combined R values for stations 1-12 and 13-24 are shown. The apparent half-ring effect for the "rate only" function is approximately ± 2 ppm (that is, the full width is 4 ppm). For all of the other fitting functions (including the rate+asymmetry+phase version, for which there should be no half-ring effect), there is a discrepancy between the two halves at the level of about ± 1 ppm. It is thus not clearly distinguishable from a statistical fluctuation. However, the most reasonable assumption is that approximately 1 ppm of the half-ring effect may be attributed to to the CBO modulation of the $g-2$ asymmetry and about 1 ppm to the CBO modulation of the $g-2$ phase.

Multiplying the cancellation factors for the asymmetry and phase modulations by 1 ppm then gives the estimated half-ring systematic uncertainty from neglecting these effects. The estimates are quite large, of order 1 ppm. Consequently, there is no choice with the energy binned method other than to fit for all of the CBO effects.

The difference between the fitted statistical uncertainties for the rate+asymmetry+phase and "rate only" functions gives another estimate of the systematic error from the half-ring effect. Unfolded in quadrature, it is approximately 0.3 ppm.

	(I)	(II)	(III)	(IV)	increase in stat. error from I to III
A	128.058 ± 0.565	128.606 ± 0.590	128.861 ± 0.626	128.145 ± 0.590	0.270
A'	128.153 ± 0.608	128.415 ± 0.635	128.717 ± 0.673	128.340 ± 0.634	0.289
B	128.523 ± 0.650	128.089 ± 0.679	127.931 ± 0.721	128.474 ± 0.679	0.312
B'	128.133 ± 0.697	127.808 ± 0.729	127.693 ± 0.773	128.094 ± 0.727	0.334
C	128.119 ± 0.624	128.481 ± 0.652	128.573 ± 0.691	128.121 ± 0.651	0.297
C'	128.265 ± 0.671	128.389 ± 0.702	128.447 ± 0.743	128.291 ± 0.699	0.319

Table 3: R values for fitting functions with different CBO-related terms. Fitting functions: (I) rate only, (II) rate+asymmetry, (III) rate+asymmetry+phase, (IV) rate+phase.

CBO:	Rate	Asymmetry	Phase	δR (I)	δR (II)	δR (IV)
A	0.476 ± 0.008	0.324 ± 0.096	0.456 ± 0.171	0.77	0.46	0.32
A'	0.425 ± 0.008	0.200 ± 0.127	0.336 ± 0.170	0.53	0.34	0.20
B	0.475 ± 0.012	0.174 ± 0.129	0.807 ± 0.295	0.97	0.81	0.17
B'	0.418 ± 0.012	0.455 ± 0.223	0.961 ± 0.401	1.41	0.96	0.46
C	0.495 ± 0.010	0.302 ± 0.131	0.718 ± 0.249	1.02	0.72	0.30
C'	0.439 ± 0.010	0.271 ± 0.173	0.727 ± 0.269	1.00	0.73	0.27

Table 4: Cancellation factors when half-ring effects are averaged over all available stations, together with the estimated systematic uncertainties on R that would be applicable if these effects were neglected. Fitting functions: (I) rate only, (II) rate+asymmetry, (IV) rate+asymmetry+phase.

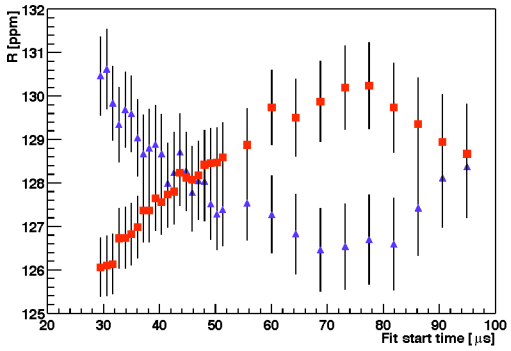

(a) rate only

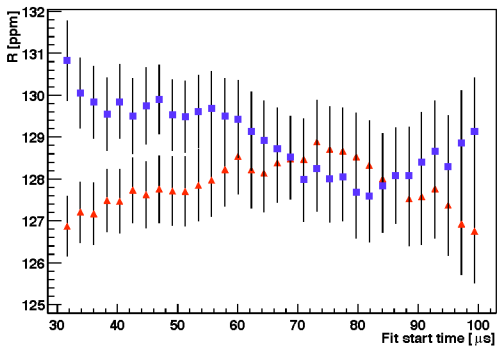

(b) rate+asymmetry

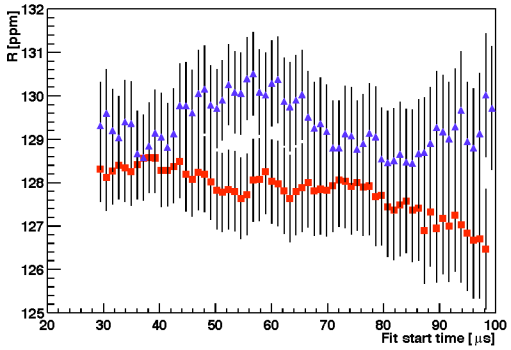

(c) rate+asymmetry+phase

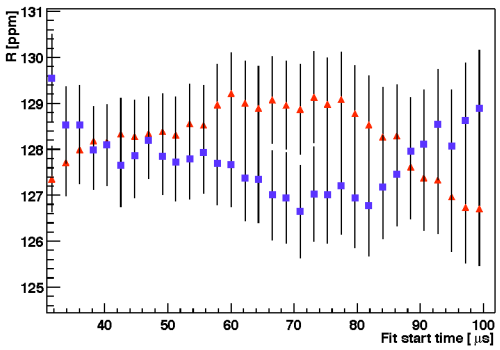

(d) rate+phase

Figure 38: R versus fit start time for stations 1-12 and 13-24 for various fitting functions. This illustrates the magnitude of the half-ring effect for the various fitting functions.

10 Gain corrections

The gain stability of the detector and pulse fitter comes from the average energy versus time after pileup subtraction:

$$< E_{PUS} > (t) = \frac{\int_{E_{low}}^{E_{high}} E[N(E) - N_{PU}(E)]dE}{\int_{E_{low}}^{E_{high}} N(E) - N_{PU}(E)dE}$$

These plots are made for $E_{low} = 2$ GeV, with two different upper cuts $E_{high} = 3.2$ GeV and $E_{high} = 6.2$ GeV. They appear in Figures 39 through 42. The different upper energy cuts provide some measure of the systematic error from residual pileup in $< E > (t)$.

These gain corrections were parameterized with two exponentials:

$$G(t) = 1 + A_1 e^{-t/\tau_1} + A_2 e^{-t/\tau_2}$$

The coefficients A_1 and τ_1 are defined by the behavior after 90 μs. They are then held fixed and A_2 and τ_2 are determined starting at very early times (the start time is station-dependent, but is 15 μs for most stations). In a final step, all four parameters are allowed to vary. The parameters that are determined from these fits are listed in Table 5.

To determine the systematic error from the time-dependent gain, fits were performed on three slightly different data sets:

- one without gain corrections applied (set 0), and
- one with gain corrections applied (set 1),
- one with five times the gain corrections applied (set 5)

The data set with gain corrections (set 1) is taken to be the central value. $\frac{dR}{dG}$ is taken from the slope of a line fit through the R values, as illustrated in Figure 43(a). The results of these fits for the various start time groups are shown in Table 6.

A level of confidence in the gain corrections is estimated from two different sources. First, the difference between $G(t)$ with upper energy cuts at 3.2 GeV and 6.2 GeV can be quantified by taking

$$\frac{G_{low} - G_{high}}{G_{low} - 1}$$

at each point from 50 μs to 200 μs. An appropriately weighted average over the time points is taken for each station, yielding the results shown in Figure 44. Averaged over all stations, the value is 34 percent.

This level of confidence is approximately confirmed by the position of the χ^2 minima as illustrated in Figure 43(b) and listed in Table 6. The maximum deviation from 1 unit of gain correction is 41 percent, and most of the groups are within 15 percent.

The value of 41 percent is the largest deviation noted, so it is the level of confidence in the gain corrections that is assumed for calculating the systematic effect on R.

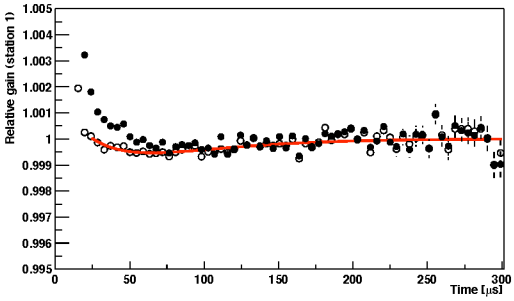

(a) Station 1

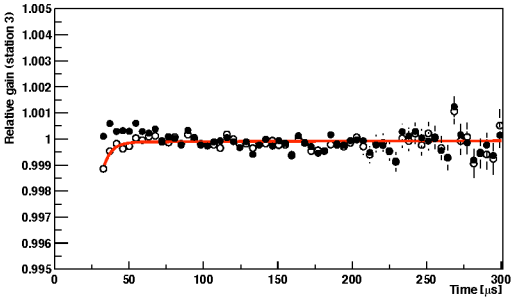

(b) Station 3

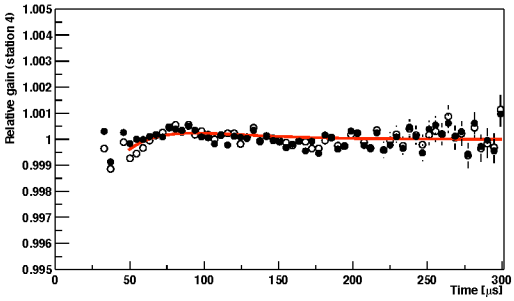

(c) Station 4

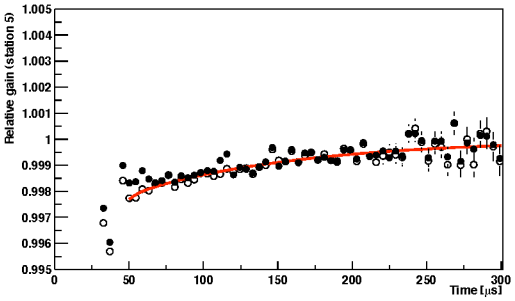

(d) Station 5

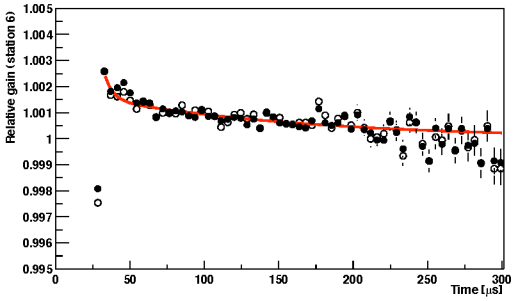

(e) Station 6

Figure 39: $G(t)$ after pileup subtraction; the open circles are integrated from 2.0 to 3.2 GeV while the closed circles are integrated from 2.0 to 6.2 GeV. The conversion factor from $< E >$ to gain is already applied. Stations 1-6.

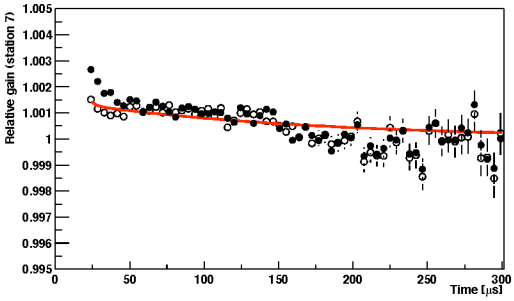

(a) Station 7

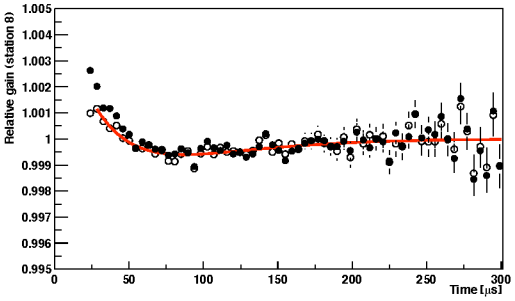

(b) Station 8

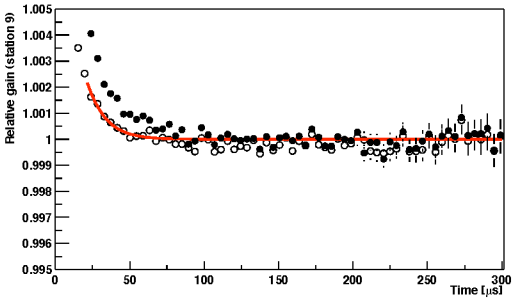

(c) Station 9

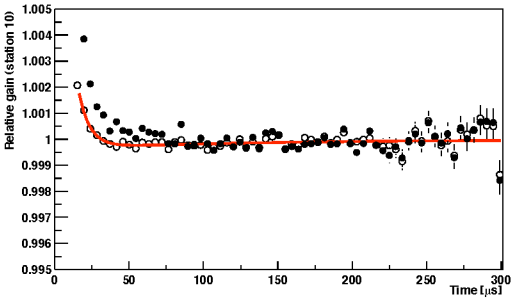

(d) Station 10

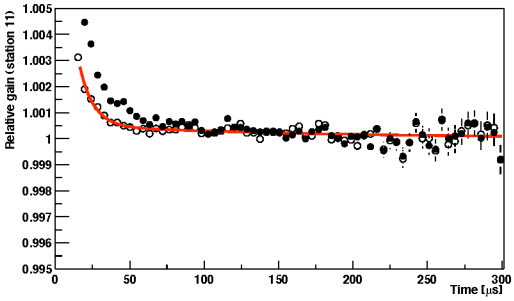

(e) Station 11

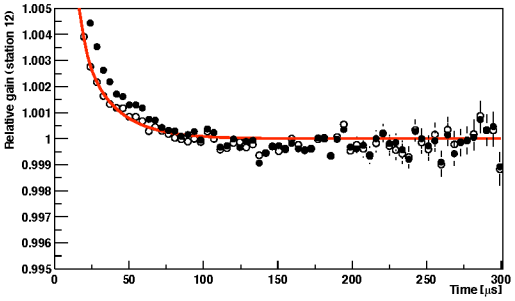

(f) Station 12

Figure 40: $G(t)$ after pileup subtraction; the open circles are integrated from 2.0 to 3.2 GeV while the closed circles are integrated from 2.0 to 6.2 GeV. The conversion factor from $< E >$ to gain is already applied. Stations 7-12.

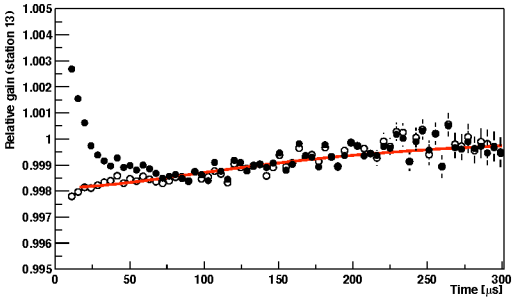

(a) Station 13

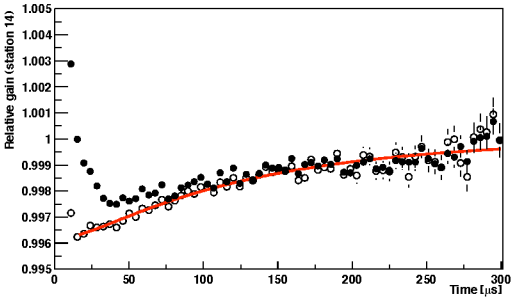

(b) Station 14

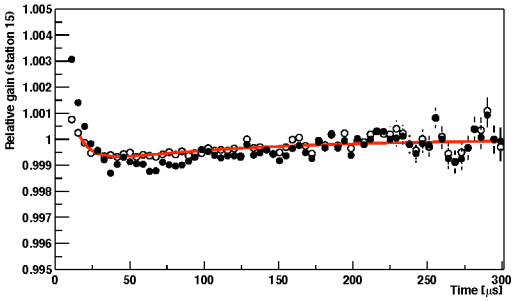

(c) Station 15

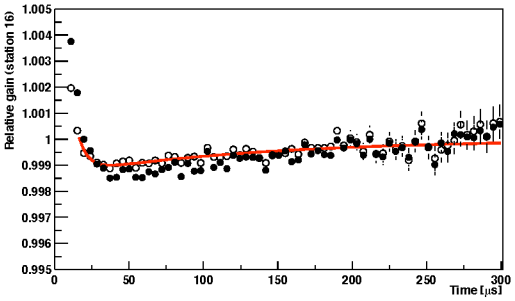

(d) Station 16

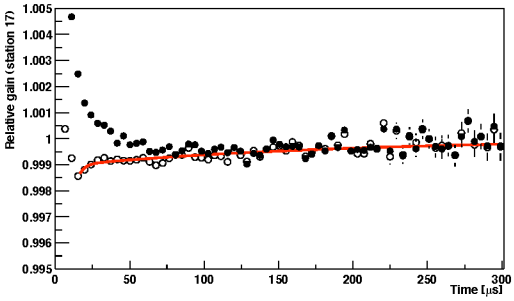

(e) Station 17

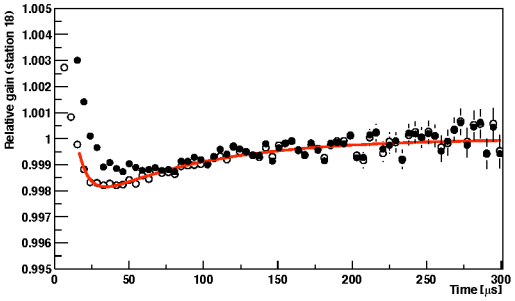

(f) Station 18

Figure 41: $G(t)$ after pileup subtraction; the open circles are integrated from 2.0 to 3.2 GeV while the closed circles are integrated from 2.0 to 6.2 GeV. The conversion factor from $< E >$ to gain is already applied. Stations 13-18.

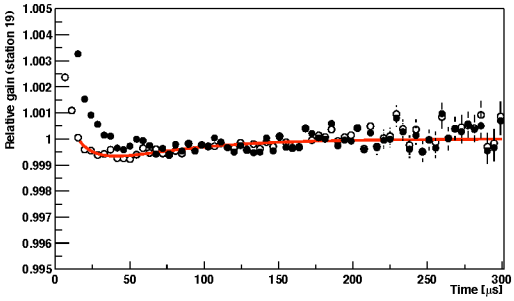

(a) Station 19

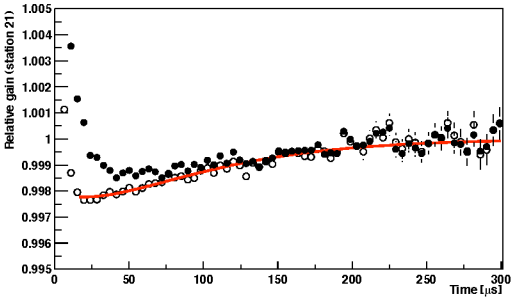

(b) Station 21

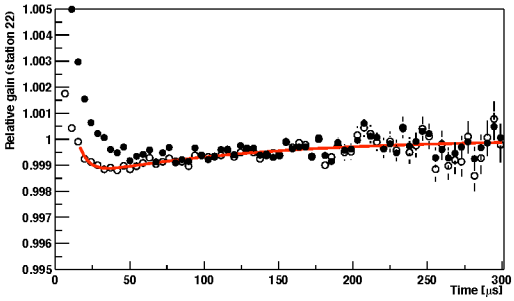

(c) Station 22

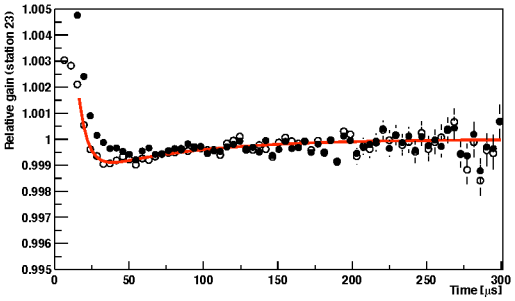

(d) Station 23

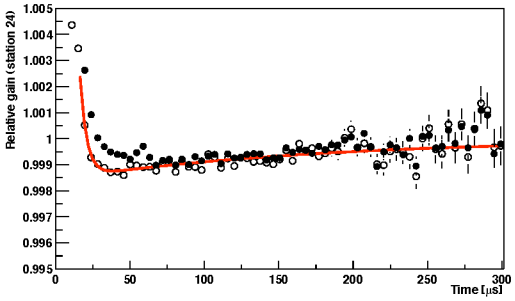

(e) Station 24

Figure 42: $G(t)$ after pileup subtraction; the open circles are integrated from 2.0 to 3.2 GeV while the closed circles are integrated from 2.0 to 6.2 GeV. The conversion factor from $< E >$ to gain is already applied. Stations 19-24.

Station	A_1	τ_1 [μs]	A_2	τ_2 [μs]	$g(50\ \mu s)$ [%]
1	-1.51×10^{-1}	40.4	1.53×10^{-1}	39.7	-0.04
3	-1.26×10^{-4}	500.0	-4.00×10^{-1}	5.4	-0.02
4	3.73×10^{-1}	31.6	-3.82×10^{-1}	31.2	-0.05
5	-3.24×10^{-3}	115.6	-4.00×10^{-1}	6.6	-0.23
6	1.91×10^{-3}	139.0	4.00×10^{-1}	5.5	0.14
7	1.47×10^{-3}	163.9	4.00×10^{-1}	3.1	0.11
8	-2.50×10^{-1}	40.9	2.56×10^{-1}	40.1	0.00
9	-2.42×10^{-1}	10.0	2.51×10^{-1}	10.2	0.02
10	-3.64×10^{-4}	138.2	1.81×10^{-2}	7.6	-0.02
11	1.31×10^{-2}	9.4	5.29×10^{-4}	171.9	0.05
12	7.46×10^{-2}	4.3	7.40×10^{-3}	22.2	0.08
13	-1.99×10^{-1}	87.1	1.97×10^{-1}	86.2	-0.18
14	-4.52×10^{-3}	122.3	7.13×10^{-4}	16.9	-0.30
15	-1.07×10^{-3}	110.4	6.03×10^{-3}	9.3	-0.07
16	-1.39×10^{-3}	132.5	1.65×10^{-2}	6.5	-0.09
17	-1.07×10^{-3}	187.0	-1.87×10^{-2}	4.2	-0.08
18	-3.18×10^{-3}	78.4	1.73×10^{-2}	7.7	-0.17
19	-1.74×10^{-3}	58.1	4.11×10^{-3}	13.4	-0.06
21	-9.44×10^{-2}	55.0	9.24×10^{-2}	53.2	-0.20
22	-1.60×10^{-3}	116.7	1.19×10^{-2}	6.9	-0.10
23	-1.72×10^{-3}	68.4	3.84×10^{-2}	6.4	-0.08
24	-1.60×10^{-3}	171.8	1.33×10^{-1}	4.6	-0.12

Table 5: Coefficients in the parameterization of the gain corrections $G(t) = 1 + A_1 e^{-t/\tau_1} + A_2 e^{-t/\tau_2}$.

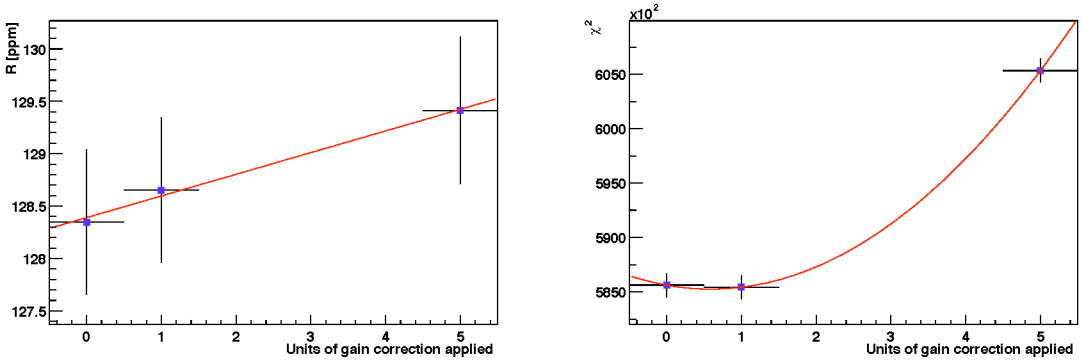

(a) R (b) χ^2

Figure 43: R and χ^2 for fits with different amounts of gain correction applied. (Start time group C.)

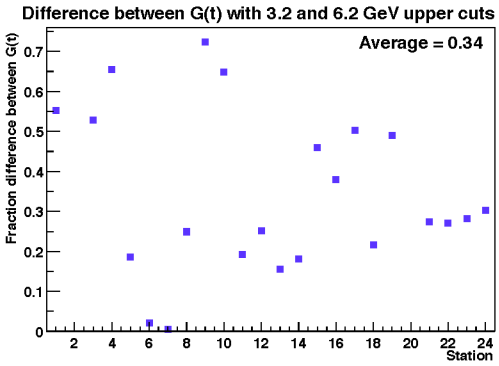

Figure 44: Difference between $G(t)$ for two upper energy cuts, quantified as $| < (G_{low} - G_{high})/(G_{low} - 1) > |$. This quantity sets the level of confidence in the gain corrections.

	A	A'	B	B'	C	C'
$\frac{dR}{dG}$ [ppm/unit of gain correction]	0.09	0.11	0.17	0.21	0.21	0.25
χ^2 minimum [unit of gain correction]	0.85	0.94	0.65	1.02	0.59	0.91
χ^2 width [unit of gain correction]	0.02	0.02	0.04	0.04	0.03	0.02
δR_{gain} [ppm]	0.037	0.045	0.070	0.086	0.086	0.100

Table 6: Estimate of the gain systematic error.

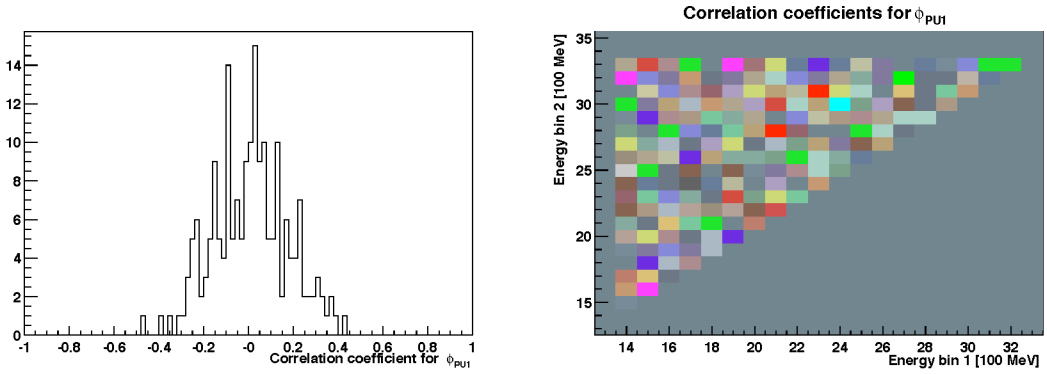

(a) (b)

Figure 45: Correlation coefficients between energy bins for the pileup phase ϕ_{PU1}.

11 Systematic errors from pileup

Several separate systematic uncertainties are assigned for pileup. The first is really a renamed statistical error; it folds the statistical uncertainties from the pileup fits into the uncertainty of the ordinary fits. It is the moral equivalent of the correction of the χ^2 at early times from pileup subtraction as described in [1]. The second value accounts for a possible global under- or over-estimation of pileup. Such an effect could be caused, for instance, by non-uniformities in the pulse fitter as a function of the time separation between pulses. The third value accounts for a possible energy dependence of the pileup construction efficiency. The final pileup-related systematic uncertainty accounts for the "unseen" pileup below the hardware threshold.

Gerco Onderwater has found that the fitted pileup phases are substantially uncorrelated from one energy bin to the next. He used the following procedure (some of the following text is drawn from a work-in-progress draft of his note):

- Cut up the full data set into 40 subsets of essentially uniform size.
- For each subset, construct the pileup spectrum as a function of energy and time.
- In each energy bin within each subset, fit the pileup spectrum as usual.
- For every pair of energy bins i and j, plot ϕ^i_{PU1} versus ϕ^j_{PU1}. Obtain the correlation factor $\rho = \sigma_{ij}/(\sigma_i \cdot \sigma_j)$. Average ρ over the full energy range from 1.4 to 3.2 GeV.

The distributions of correlation factors are shown in Figure 45. They form a Gaussian distribution about 0, and there is no apparent trend as a function of energy.

Consequently, the statistical part of the pileup systematic error can be determined by independently varying each of the pileup phases over the range of their uncertainties. The other parameters (N_{PU}, A_{PU1}, and so on) are varied together in the same way. The procedure

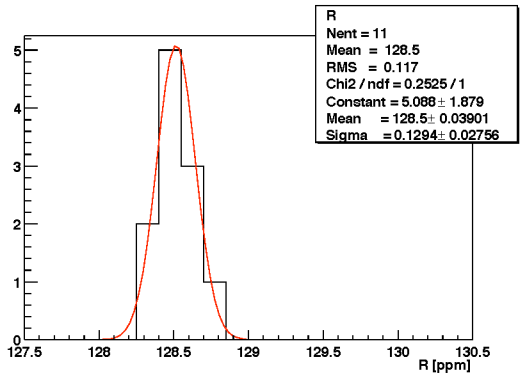

Figure 46: Distribution of R values obtained from fits with pileup parameters chosen randomly over their 1 σ range. (Start time group C.)

that was actually used was to perform the fit several times with each of the pileup parameters modified independently by adding a random number. The random numbers were chosen from a Gaussian distribution whose width is the statistical uncertainty of the parameter. The RMS of the resulting distribution of R values is then taken as the result. The results are shown in Figure 46 and summarized in Table 8. When presented in the overall error table, this uncertainty is combined with the statistical error rather than the systematic error.

The global pileup efficiency systematic error was evaluated by performing the fit with the pileup terms $N_{PU}(E,t)$ multiplied by various scale factors M_{PU}. $\frac{dR}{dM_{PU}}$ was determined from the slope of a line fit through the points, as illustrated in Figure 47(a). The results for the various start time groups are given in Table 8. For all of the start time groups, the slope is approximately 5 ppm per unit of pileup. Consequently, it is important to know the efficiency of the pileup construction procedure.

This efficiency has been established as 3.4 percent based on three different sources of information. First, the difference between the energy spectra at early and late times gives an estimate of how well the procedure works at high energies. The early-time data is taken from 49.11 μs to 66.57 μs (4 precession cycles) and the late-time data from 300 μs to 439.69 μs (32 precession cycles). The spectra are normalized relative to each other based on energies from 1.8 GeV to 2.2 GeV. The data for each station are shown in Figures 48 through 51. The residual pileup is the ratio of the sums of the absolute values of the two curves. This quantity is plotted versus station number in Figure 52. The average inefficiency determined with this method is 3.4 percent; that figure is used to quantify the systematic error.

An additional contribution accounts for the possible energy dependence of the pileup subtraction efficiency. It is assumed that the change in this efficiency over the range from 1.4 to 3.2 GeV is less than approximately twice the global inefficiency. The systematic uncertainty was evaluated by comparing the fitted R values for several efficiency functions:

$$(\mathrm{A})\epsilon_{PU} = 1$$

$$(\mathrm{B})\epsilon_{PU} = 1 + 0.034\frac{E - 2.3GeV}{0.9GeV}$$

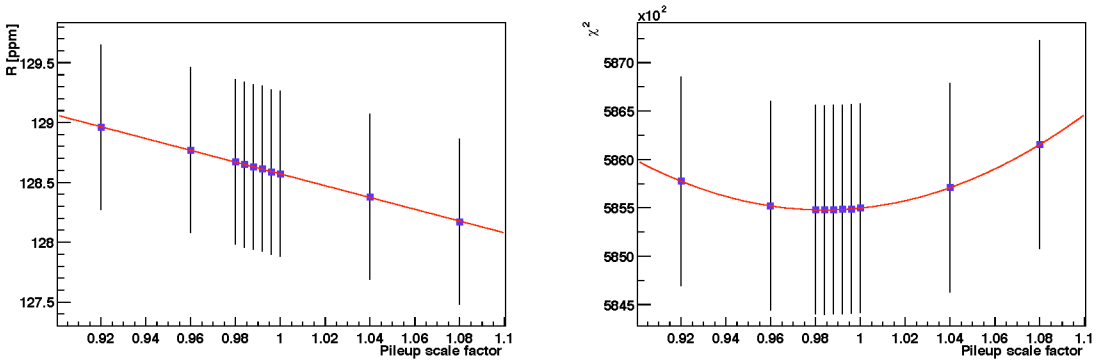

(a) R (b) χ^2

Figure 47: R and χ^2 for fits with varying pileup scale factors applied. (Start time group C.)

$$(\mathrm{C})\epsilon_{PU} = 1 - 0.034\frac{E - 2.3GeV}{0.9GeV}$$

It was found that $R_B - R_A = -0.08$ ppm and that $R_C - R_A = 0.07$ ppm. Consequently, an uncertainty of 0.08 ppm is attributed to the energy dependence of the pileup subtraction efficiency. This systematic error was only estimated for analysis method C, though it has been copied to all lines of the table.

A second view of the pileup construction efficiency is provided by the difference between the gain corrections $G(t)$ with two different upper energy cuts, at 3.2 GeV and 6.2 GeV. The sum of the squares of the differences between these curves over the range from 40 μs to 100 μs is plotted as a function of the pileup subtraction scale factor M_{PU}. It forms a parabolic minimum as shown in Figure 53(a). The positions of these minima are shown for each station in Figure 53(b). The largest discrepancy from 1 is 3.5%, and the average is 2%.

Finally, this level of confidence is supported by the positions of the fit χ^2 minima, which differ from 1 by at most 2 percent. These results are shown in Table 8.

The first step in the "unseen" pileup systematic error analysis is to use a simulation to compute the changes in the spectrum caused by pulses that are too small to be considered by MilliFit. The simulation first chooses an ordinary event from the "real" (E, t) distribution (the pileup-subtracted spectrum of station 18) weighted by an additional factor of

$$e^{-t/\tau}[1 + A_{unseen}\cos(\omega_a t + \phi_{unseen})].$$

The parameters A_{unseen} and ϕ_{unseen} are chosen quite conservatively as $A_{unseen} = 0.08$ and $\phi_{unseen} = 100$ mrad. It then chooses the energy of the unseen pulse from the portion of the GEANT energy distribution below 200 MeV. A simulated WFD island containing the two pulses is created and processed with MilliFit. The original (E, t) pair is filled into a histogram with weight -1 and the modified (E, t) is filled with weight +1. The energy and time distributions of the simulated unseen pileup are shown in Figure 54.

The second step in this analysis is to observe the effect of the unseen pileup on the stability of the $(g - 2)$ asymmetry. The simulated unseen pileup distribution is added to

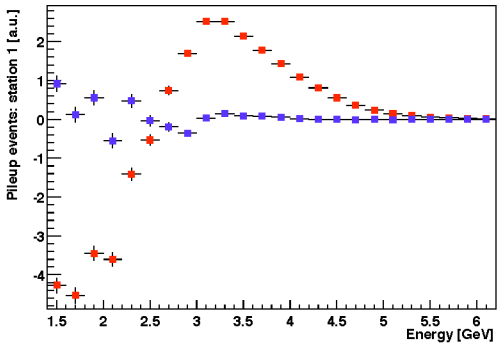

(a) Station 1

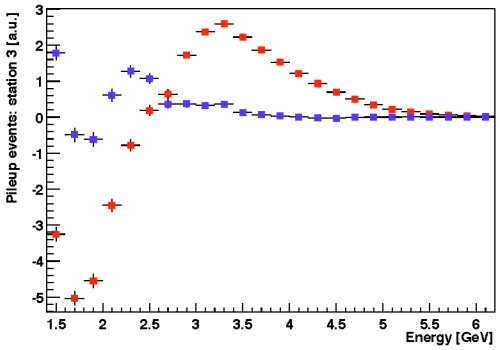

(b) Station 3

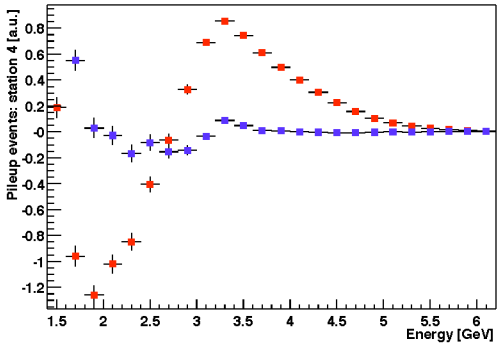

(c) Station 4

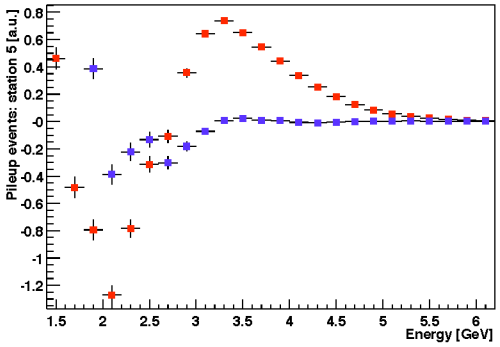

(d) Station 5

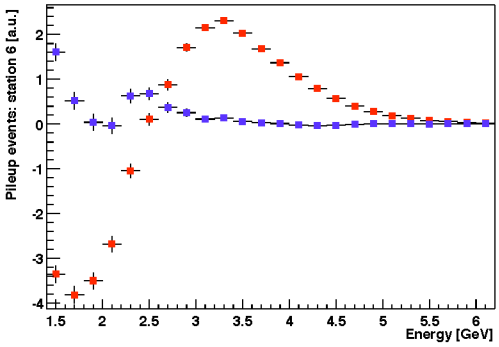

(e) Station 6

Figure 48: Difference between energy distributions at early and late times with and without pileup subtraction. Stations 1-6.

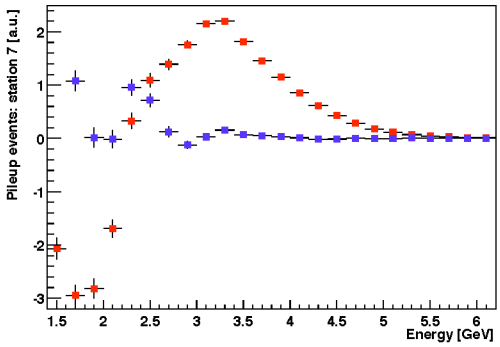

(a) Station 7

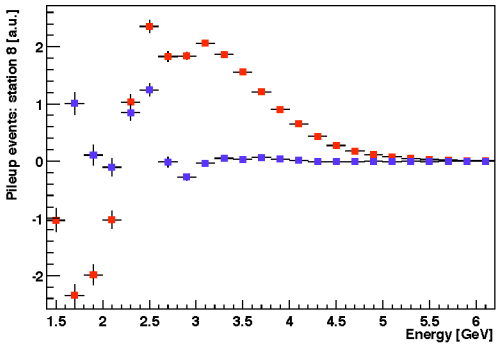

(b) Station 8

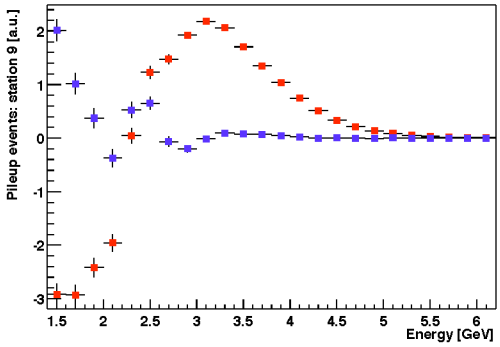

(c) Station 9

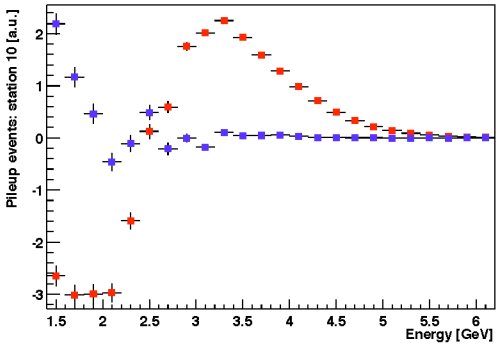

(d) Station 10

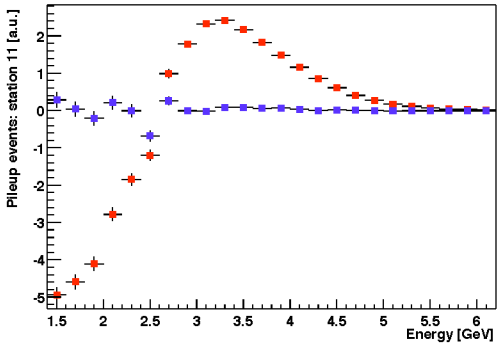

(e) Station 11

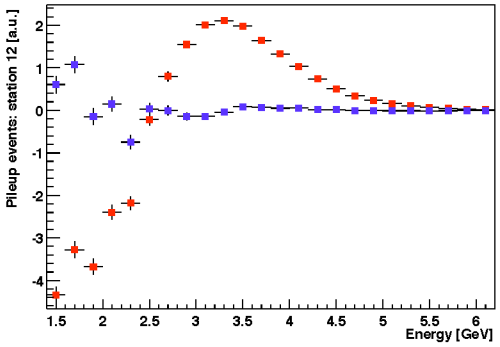

(f) Station 12

Figure 49: Difference between energy distributions at early and late times with and without pileup subtraction. Stations 7-12.

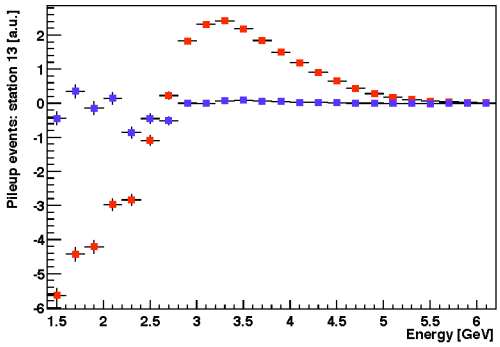

(a) Station 13

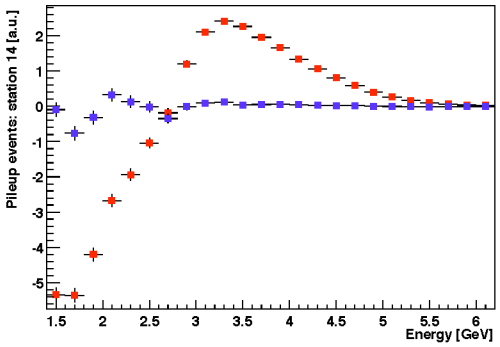

(b) Station 14

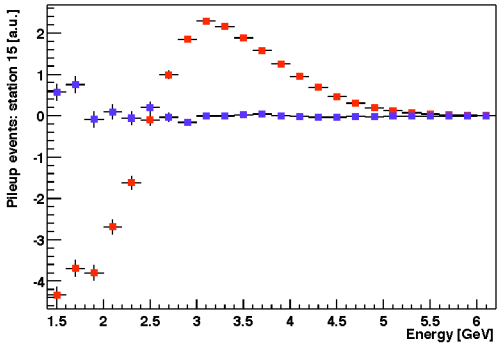

(c) Station 15

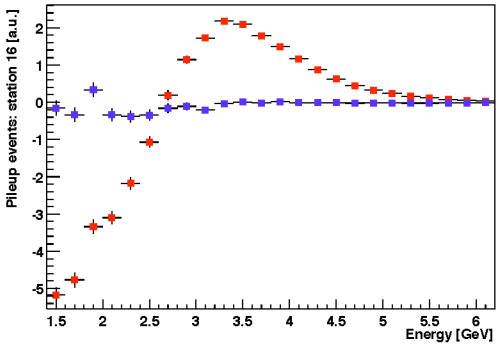

(d) Station 16

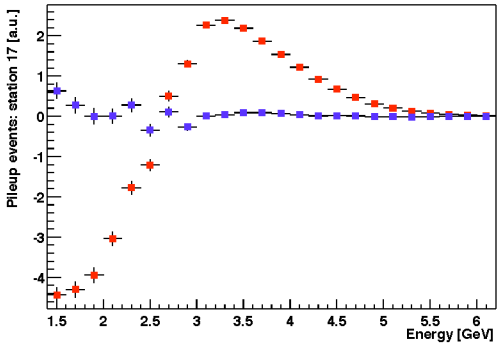

(e) Station 17

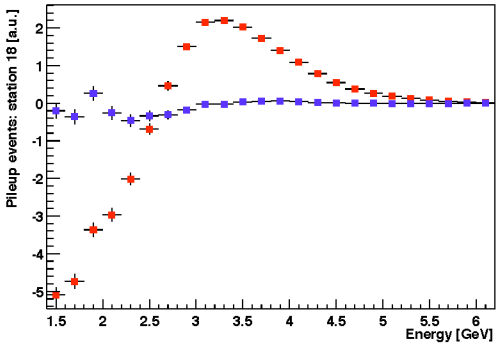

(f) Station 18

Figure 50: Difference between energy distributions at early and late times with and without pileup subtraction. Stations 13-18.

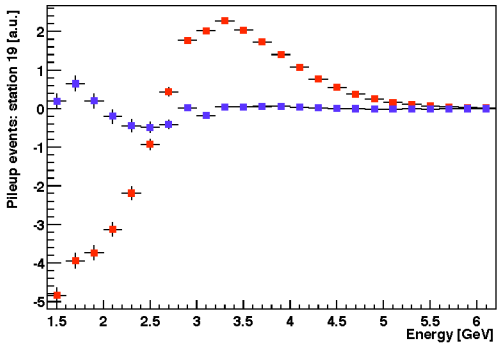

(a) Station 19

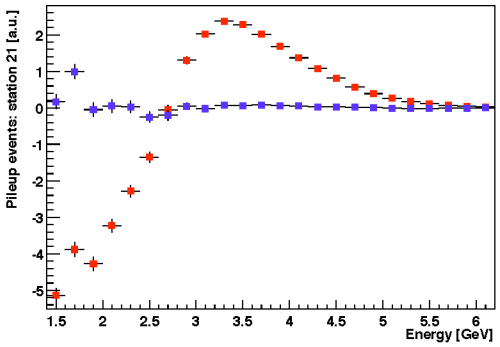

(b) Station 21

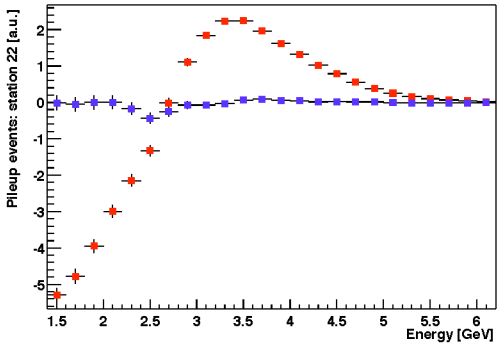

(c) Station 22

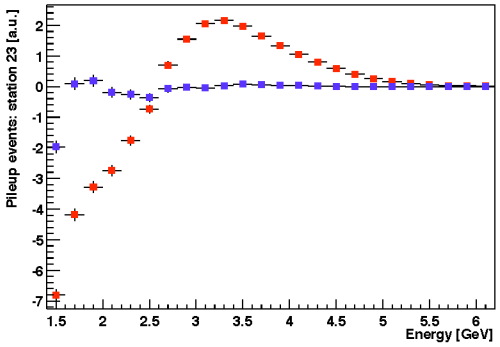

(d) Station 23

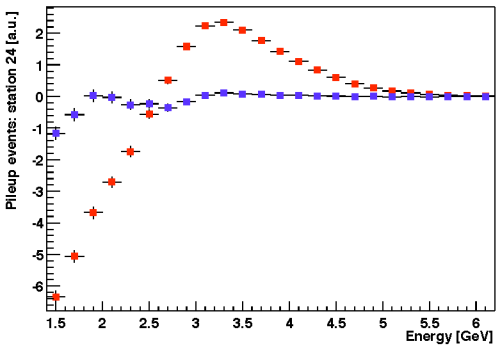

(e) Station 24

Figure 51: Difference between energy distributions at early and late times with and without pileup subtraction. Stations 19-24.

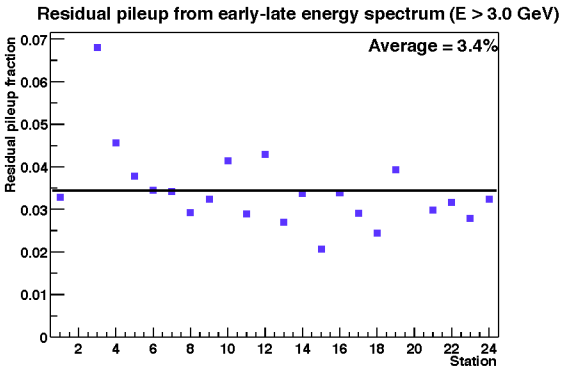

Figure 52: Residual pileup fractions for each station for energies above 3 GeV based on early-late energy spectrum differences.

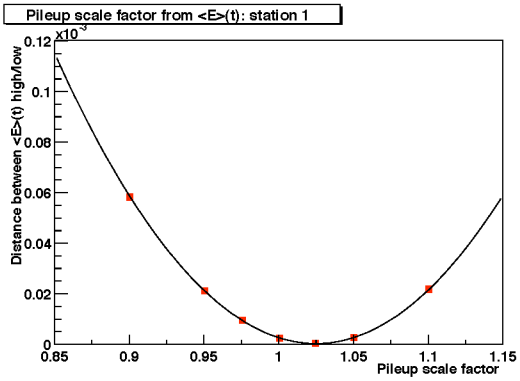

(a) Example parabolic minimum (for station 1)

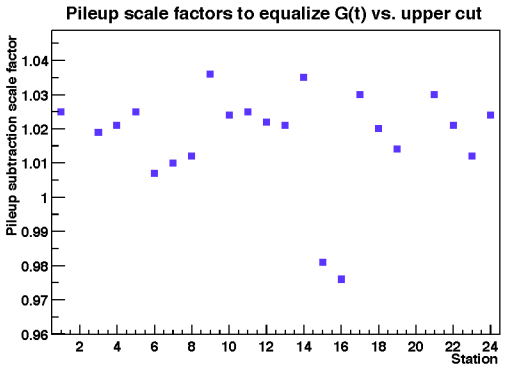

(b) Residual pileup fractions giving minimum χ^2 for each station

Figure 53: Results from sweeping pileup subtraction scale factors and comparing $G(t)$ for different upper energy cuts.

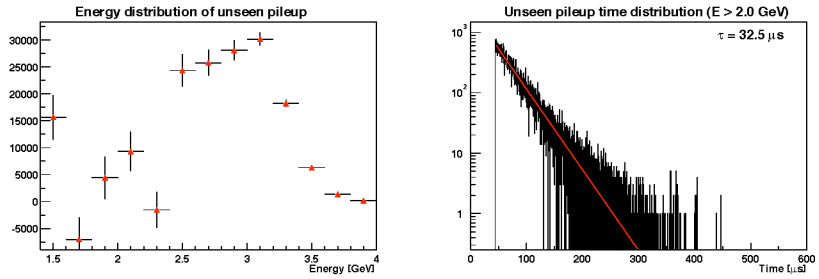

(a) Energy distribution (b) Time distribution

Figure 54: Energy and time distributions of simulated unseen pileup. The statistics of these plots correspond to 10 "units" per station.

each station's histogram, multiplied by factors of 0, 1, 3, and 5. Fits are done at each of the ordinary fit start times and at 129.9 μs. The difference between the average asymmetry at 49.1 μs and 129.9 μs is plotted versus energy for each unseen pileup multiplier. To compute this average, the asymmetry for each station is rescaled to be 1 at 49.1 μs, and an arithmetic mean is taken. The correlated error bars are from the standard difference-of-quadratures Kawall formula. Several things are evident from this plot, which appears in Figure 55.

- Over this time range, the unperturbed spectrum has an average asymmetry which is consistent from early to late times in each energy band above 2.2 GeV.
- For energies less than 2.2 GeV, the asymmetry in the unperturbed spectrum decreases as a function of fit start time. One mechanism that would account for this is lost protons. Their distribution cuts off near 1.8 GeV, they are non-wiggling, and they become a larger fraction of the data at later times. (Another point of interest is that protons also have different CBO properties from muons, possibly accounting for some of the interesting trends of CBO parameters versus energy.)
- The asymmetry consistency is much more sensitive to unseen pileup at very high energies than at lower energies. Consequently, we can set the best limit on unseen pileup by looking at these energies.

The amount of unseen pileup in the data was estimated to be 0.29±0.26 units, where each unit corresponds to 1.5×10^8 generated events after 45 μs. This estimate was constructed from the values shown in Table 7. In this table, ΔA represents the change in the asymmetry of the unperturbed data while ΔA_{unseen} stands for the asymmetry change that would be caused by 1 unit of unseen pileup.

The fitted R value is also plotted versus number of units of added unseen pileup, as illustrated in Figure 56. The resulting slope varies by start time group from 0.20 to 0.36 ppm per unit of unseen pileup. This slope is multiplied by 0.29 to obtain the final systematic error estimate.

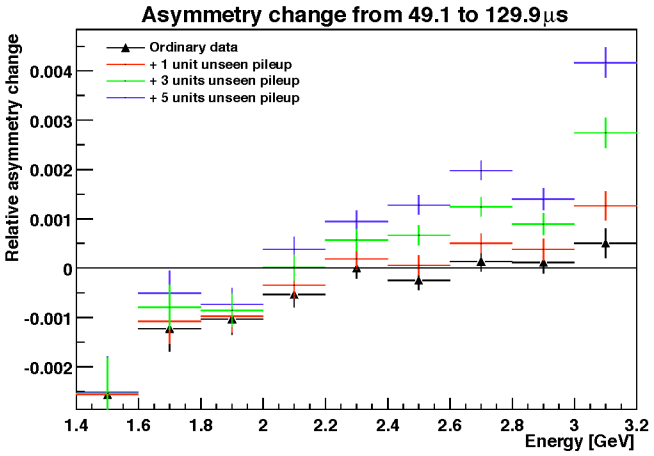

Figure 55: Change in the fitted asymmetry between fit start times of 49.1 μs to 129.9 μs, for the unperturbed data and with various amounts of added unseen pileup.

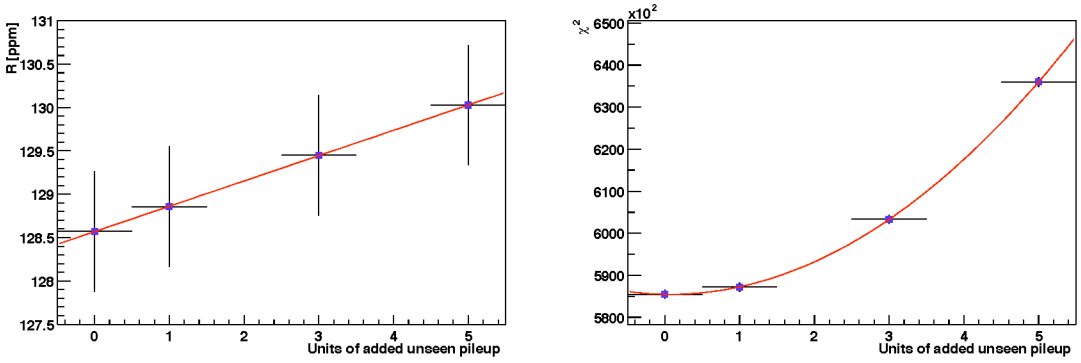

(a) R (b) χ^2

Figure 56: R and χ^2 for fits with varying amounts of added unseen pileup. (Start time group C.)

Energy	$\Delta A/\Delta A_{unseen}$
2.2-2.4	0.03 ± 1.15
2.4-2.6	-0.82 ± 0.64
2.6-2.8	0.36 ± 0.52
2.8-3.0	0.45 ± 0.85
3.0-3.2	0.67 ± 0.40
Weighted average	0.29 ± 0.26

Table 7: Change in asymmetry (ΔA) from a fit start time of 49.1 μs to 129.9 μs, as a fraction of the amount expected from one arbitrary unit of unseen pileup (ΔA_{unseen}). The error bars only take into account the uncertainty of ΔA, not that of ΔA_{unseen}.

	A	A'	B	B'	C	C'
δR_{PU}: statistical part [ppm]	0.112	0.131	0.095	0.114	0.117	0.131
$\frac{dR}{dM_{PU}}$ [ppm/unit of pileup]	-5.71	-5.15	-4.59	-4.99	-4.93	-5.15
χ^2 minimum [unit of pileup]	0.992	0.980	0.991	0.999	0.984	0.980
χ^2 width [unit of pileup]	0.003	0.004	0.004	0.005	0.004	0.004
δR_{PU}: global scale part [ppm]	0.194	0.175	0.156	0.170	0.167	0.175
δR_{PU}: unseen part [ppm]	0.057	0.076	0.073	0.090	0.085	0.104

Table 8: Estimated systematic errors from pileup.

12 Muon losses

The muon losses as measured by triple coincidences in the FSDs are supplied by Chris Polly. The supplied data is in the form of a histogram $f_\Lambda^{abs}(t)$ which is proportional to the absolute muon loss rate. It is first necessary to convert it to a fractional muon loss rate $f_\Lambda(t) = f_\Lambda^{abs}(t)e^{t/\tau}$. In this calculation, an assumed lifetime $\tau = 64.367$ μs is used. Now, during a time interval dt where the number of stored muons is $N(t)$, the absolute number of lost muons is proportional to $f_\Lambda(t)\ N(t)\ dt$.

In the absence of muon losses (and, for simplicity, averaging over the $g-2$ cycle), the differential equation that is solved is

$$\frac{dN}{dt} = -\frac{N}{\tau}$$

This is a separable first-order ordinary differential equation that is solved like this:

$$\int_{N_0}^{N} \frac{1}{N'}\ dN' = \int_{t_0}^{t} -\frac{1}{\tau}\ dt'$$

$$\log N_0 - \log N = -\frac{t_0}{\tau} + \frac{t}{\tau}$$

$$N(t) = N_0 \exp\left(-(t-t_0)/\tau\right)$$

Now including muon losses, the differential equation is modified:

$$\frac{dN}{dt} = -N(\frac{1}{\tau} + N_\Lambda f_\Lambda(t))$$

$$\int_{N_0}^{N} \frac{1}{N'}\ dN' = -\int_{t_0}^{t} \frac{1}{\tau} + N_\Lambda f_\Lambda(t')\ dt'$$

$$\log N_0 - \log N = -\frac{t_0}{\tau} + \frac{t}{\tau} - N_\Lambda \int_{t_0}^{t} f_\Lambda(t')\ dt'$$

$$N(t) = N_0 \exp\left(-(t-t_0)/\tau\right) \exp\left(-N_\Lambda \int_{t_0}^{t} f_\Lambda(t')\ dt'\right)$$

Note that we can choose any value of t_0 that might be convenient. We can even choose t_0 independently in the decay term and in the muon loss term; when we do so, we only modify N_0, which is a floating parameter in the fit. Since we don't know the absolute efficiency of

	A	A'	B	B'	C	C'
$\frac{dR}{dN_\Lambda}$ [ppm/unit of loss]	0.60	0.48	-0.36	-0.28	-0.40	-0.31
$\frac{dR}{dN_{\delta\Lambda}}$ [ppm/unit of loss error]	0.009	0.008	0.004	0.004	0.003	0.002
N_Λ χ^2 minimum [unit of loss]	0.921	0.960	1.002	0.885	0.981	0.886
N_Λ χ^2 width [unit of loss]	0.014	0.021	0.020	0.030	0.017	0.026
$N_{\delta\Lambda}$ χ^2 minimum [unit of loss error]	-4.34	-3.43	-4.80	-4.08	-4.60	-3.87
$N_{\delta\Lambda}$ χ^2 width [unit of loss error]	0.35	0.52	0.35	0.53	0.35	0.53
δR_Λ [ppm]	0.072	0.058	0.043	0.034	0.048	0.037
$\delta R_{\delta\Lambda}$ [ppm]	0.014	0.019	0.019	0.016	0.014	0.008

Table 9: Estimated systematic errors from muon losses.

the FSD triple coincidence counter, N_Λ must also be a floating term in the fit. In fact, t_0 in the loss term is chosen to be 20 μs.

In addition to the muon loss rate, Chris Polly also supplies an error band that is based primarily on the uncertainty in the proton correction. The loss shape is allowed to vary by a multiple of the error band; the parameter $N_{\delta\Lambda}$ provides this. The final form of the muon loss factor is therefore

$$\Lambda(t) = \exp[-N_\Lambda/\tau \int_{t_0}^{t} (f_\Lambda(t') + N_{\delta\Lambda}\delta f_\Lambda(t'))dt']$$

R and χ^2 were plotted versus the a scale factor by which the nominal N_Λ was multiplied, as shown in Figure 57. The slope is of order 0.5 ppm per nominal loss unit, as given in Table 9.

There is one possible source of external evidence for a level of confidence in N_Λ. By taking an appropriately constructed difference between the data before and after the radial field change (when the loss rate dropped by an order of magnitude), it may be possible to obtain an independent absolute calibration. However, this analysis has not yet been done. Consequently, the only information available for this systematic error is internal to the fit.

The value of N_Λ that is used for the final results was determined from a global χ^2 minimization at the start times determined by method C. However, it is found that the position of the χ^2 minimum for the N_Λ scale factor varies from 0.88 to 1.00 depending on the start time method. Slightly different procedures therefore give normalizations that differ by up to 12 percent. Consequently, 12 percent is adopted as the level of confidence in this parameter. The resulting systematic uncertainty for R is of order 0.05 ppm.

A similar procedure was performed for $N_{\delta\Lambda}$. This parameter ought to be 0, since all relevant corrections to the muon loss shape have already been applied, but the value from the fit is around -4. The entire difference from 0 is used as a level of confidence. Nevertheless, the resulting systematic uncertainty for R is small, at most of order 0.04 ppm.

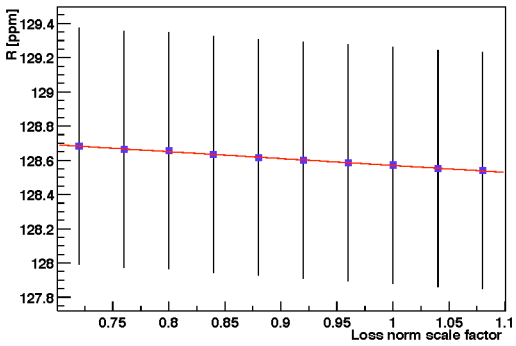

(a) R for loss scale

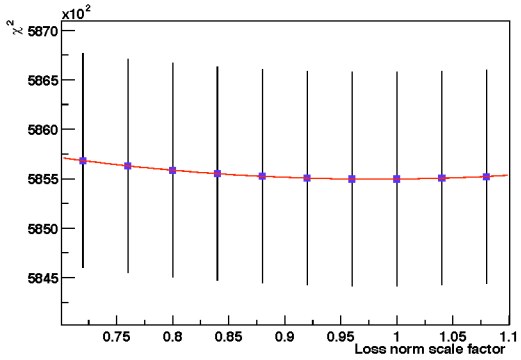

(b) χ^2 for loss scale

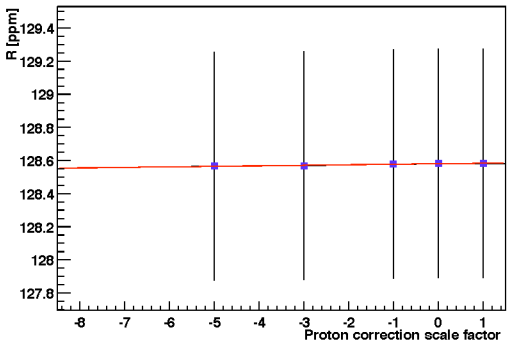

(c) R for loss shape

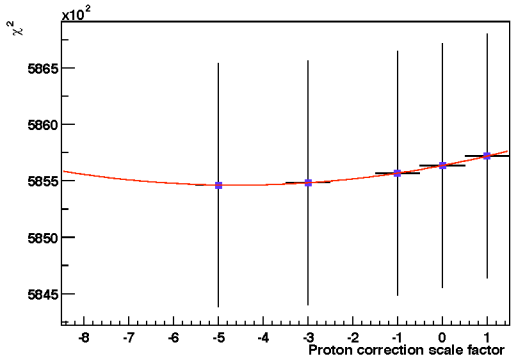

(d) χ^2 for loss shape

Figure 57: R and χ^2 for fits with varying muon loss scales and shapes. (Start time group C.)

13 CBO systematic uncertainties

It should be kept in mind that the largest component of the CBO-related systematic error is actually included in the statistical error because the half-ring effects are included in the fitting function. However, there are other systematic issues that must be accounted for separately.

The CBO modulations of the $(g-2)$ normalization and asymmetry have an envelope function which is taken to be $e^{-t/\tau_{CBO}}E(t)$. $E(t)$ measures the deviation from a purely exponential form. This envelope arises from the time dependences of the position and width oscillations of the beam, which have lifetimes that probably differ by a factor of two. It is also influenced significantly by the combination of data with different CBO frequencies.

The procedure for determining the envelope was first to determine the approximate exponential lifetime τ_{CBO} and then to measure deviations from that exponential. τ_{CBO} is determined from a fit with a start time of 49.1 μs, where it was allowed to vary in the fit. It varies with energy as shown in Figure 58. It is then fixed in fits to each energy bin, with a different lifetime for each energy. In these fits, first the full function (with a CBO rate modulation only) is applied to the entire time range. Then all of its parameters are frozen except for a scale factor that multiplies the CBO amplitude, and fits of that single parameter to short time intervals are performed. The scale factors are averaged across energy bins to give the CBO envelope $E(t)$ which is shown in Figure 59. $E(t)$ is parameterized as a polynomial and inserted into the fitting function. It is cut off at times after 245 μs, where the envelope is assumed to be purely exponential.

Two separate systematic errors are assigned for the main CBO envelope; they are added linearly to obtain the quoted result. First, the procedure for constructing the envelope perturbations $E(t)$ from the data is not completely defensible. Consequently, an uncertainty is assigned for the entire difference between the fitted R values with and without the $E(t)$ factor. Fortunately, it is very small, of order 0.01 ppm.

The variation of the fitted exponential CBO lifetime with energy also seems too large to understand fully; it moves by 30 percent from very low to very high energies. Consequently, a systematic error will be assigned to cover this range. A scale factor $A_{\tau CBO}$ is introduced to multiply the energy-dependent CBO lifetime in the fit. This scale factor is varied over the range from 0.7 to 1.3; the effect on R and χ^2 is shown in Figure 61. The slope of R versus $A_{\tau CBO}$ is determined, and it is multiplied by 0.15 to obtain the systematic error estimate. This value is half of the 30 percent lifetime variation.

There are two systematic errors assigned for the CBO frequency ω_{CBO}. The first accounts for the uncertainty in the value of the frequency. It varies with energy from 465.79 kHz to 466.11 kHz as shown in Figure 60. A conservative systematic error is evaluated to take into account this entire range of ± 0.16 kHz. A scan is made, fixing ω_{CBO} for all energy bins together at three different settings, which are chosen to be the endpoints and midpoint of this range. The slope of R as a function of ω_{CBO} is then measured; depending on start time group, it ranges from 0.01 to 0.4 ppm per kHz. The final systematic error estimate is 0.16 kHz times this slope. The results are shown in Table 10.

The envelope of the CBO modulation of the $(g-2)$ phase is derived from the same underlying effects as that of the other CBO effects, but it probably mixes the position and

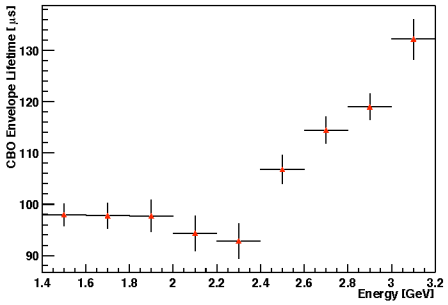

Figure 58: CBO lifetime τ_{CBO} as a function of energy.

width modes in different proportions. Consequently, its lifetime may differ from that of the other modulations by up to a factor of 2. Unfortunately, this lifetime cannot be determined from the data with any precision. Consequently, it is necessary to attribute a systematic uncertainty to this envelope. Fits were performed with various values for the ratio of this lifetime to the ordinary CBO lifetime. The χ^2 minimum, as shown in Figure 62(b), is very shallow, but R does not depend heavily on this parameter. The systematic uncertainty is determined by taking half the difference between the maximum and minimum R values over the range from 0.5 to 2 in the ratio of the two envelope lifetimes.

There are two physical sources for the CBO phase modulation. First, the time of flight is modulated by the radial beam motion. However, GEANT simulations have shown that this cannot be the dominant effect. Another model, the so-called "FBI effect," holds that the angle between the muon's momentum vector and the central orbit is modulated at the CBO frequency. As the momentum is rotated, the spin moves along with it. There is a subtle difference between the functional forms associated with the two models. If the time of flight is modulated, then the time should be altered by the CBO throughout the fitting function. In the "FBI effect" model, though, only the $g-2$ phase is modified. Fits were performed with both fitting functions. For all start time methods, the effect is less than 0.01 ppm; for the preferred method C it is less than 0.001 ppm. Consequently, this difference is not even listed in the systematic error table.

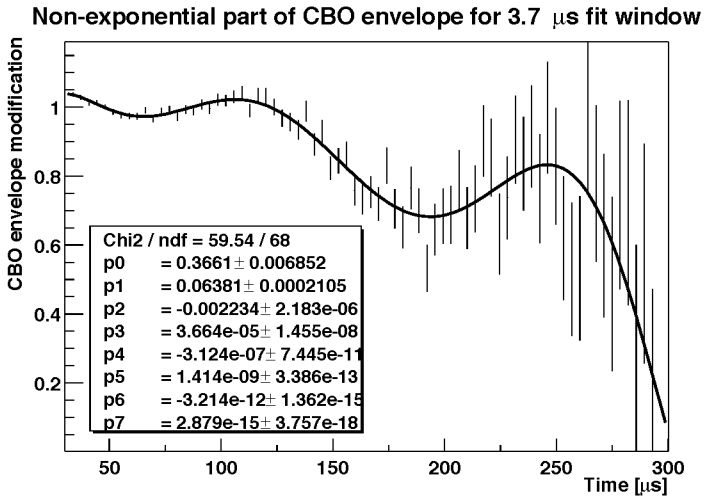

Figure 59: Empirical CBO envelope modification $E(t)$. This function multiplies an exponential with an energy-dependent lifetime.

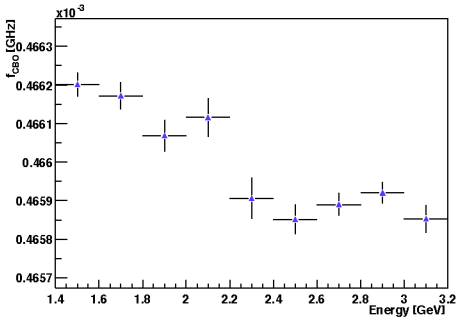

Figure 60: CBO frequency f_{CBO} as a function of energy.

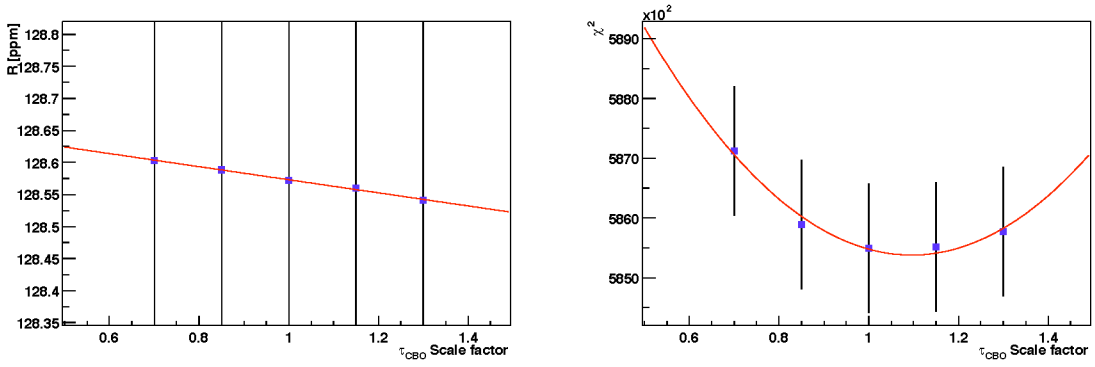

(a) R (b) χ^2

Figure 61: R and χ^2 for fits with varying (primary) CBO oscillation envelope lifetimes. (Start time group C.)

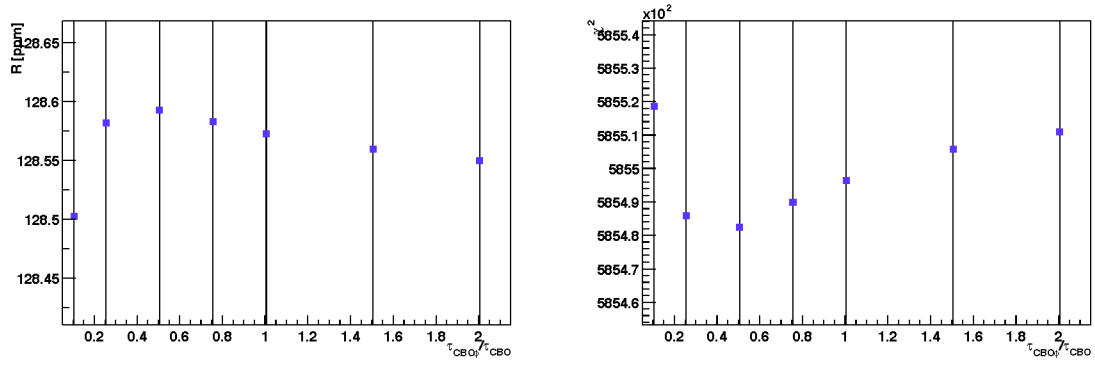

(a) R (b) χ^2

Figure 62: R and χ^2 for fits with varying CBO phase oscillation envelope ("Jim effect") lifetimes. (Start time group C.)

	A	A'	B	B'	C	C'
δR from $E(t)$	0.013	0.011	0.013	0.010	0.001	0.002
$dR/dA_{\tau CBO}$	-0.292	-0.282	0.070	0.048	-0.10	-0.02
χ^2 minimum	1.094	1.103	1.087	1.099	1.090	1.110
χ^2 width	0.0083	0.010	0.011	0.014	0.010	0.012
δR from τ_{CBO}	0.044	0.042	0.011	0.007	0.015	0.003
Total δR from main CBO envelope	0.057	0.053	0.024	0.017	0.016	0.005
$dR/d\omega_{CBO}$	0.158	0.219	0.381	0.445	-0.062	0.007
δR for ω_{CBO} value	0.025	0.035	0.061	0.071	0.010	0.001
δR for time variation of ω_{CBO}	0.008	0.004	0.024	0.027	0.032	0.004
Total δR from ω_{CBO}	0.033	0.039	0.085	0.098	0.042	0.005
δR from CBO phase modulation	0.102	0.095	0.079	0.032	0.021	0.032

Table 10: Systematic uncertainties assigned for various CBO-related effects.

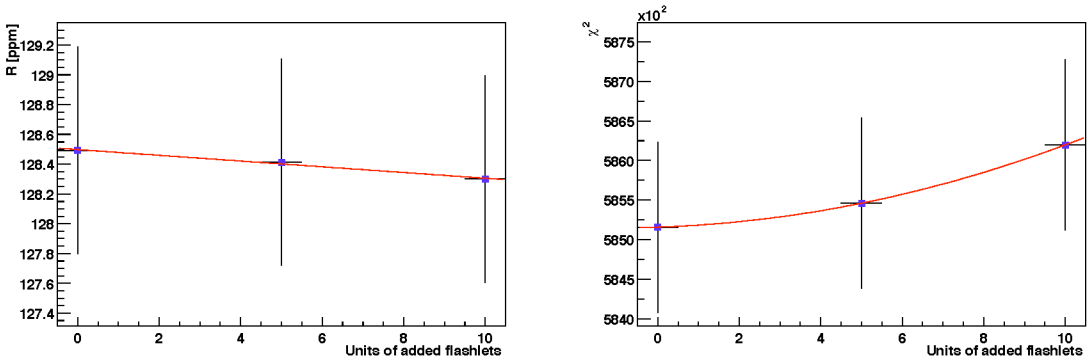

(a) R (b) χ^2

Figure 63: R and χ^2 for fits with varying amounts of simulated flashlets added. (Start time group C.)

	A	A'	B	B'	C	C'
$dR/dN_{flashlets}$ [ppm/unit of flashlets]	-0.011	-0.013	-0.002	-0.002	-0.019	-0.021

Table 11: Results of fits to spectra with artificially enhanced flashlets.

14 Systematic error from flashlets

The data from the fills in which the quadrupole firing was suppressed provides a measure of both the total number of flashlets and their distributions in time and ring position. These distributions are shown in Figure 64. (They have been multiplied by the ratio of the numbers of quadrupole-on to quadrupole-suppressed fills.)

Simulated flashlet distributions were constructed based on these distributions. Flashlets were added to the data at 0, 5, and 10 times their actual level, and the slope of the graph of R vs. flashlet level was determined. Table 11 shows the magnitude of this effect.

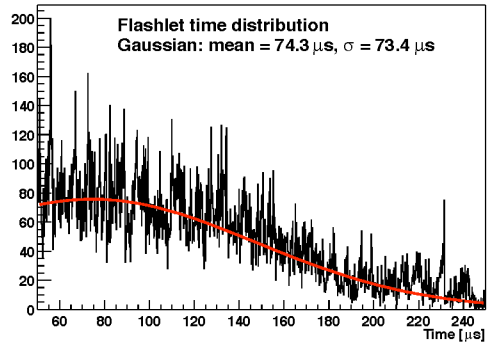

(a) Long-scale time distribution

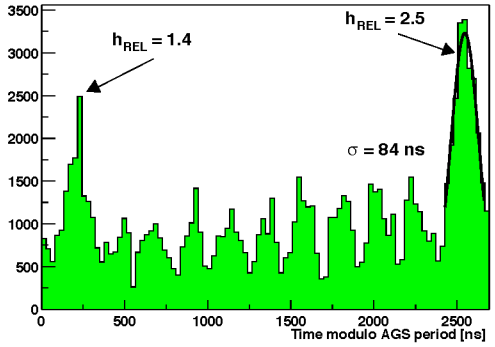

(b) Time distribution modulo the AGS cyclotron period

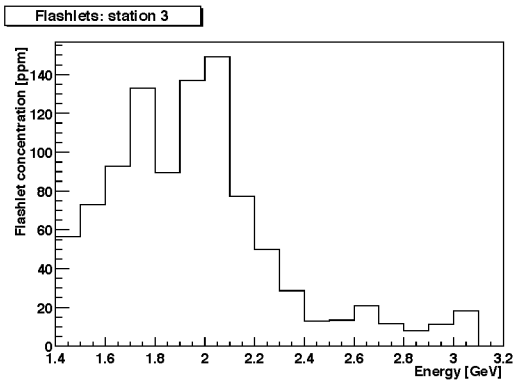

(c) Energy distribution in station 3

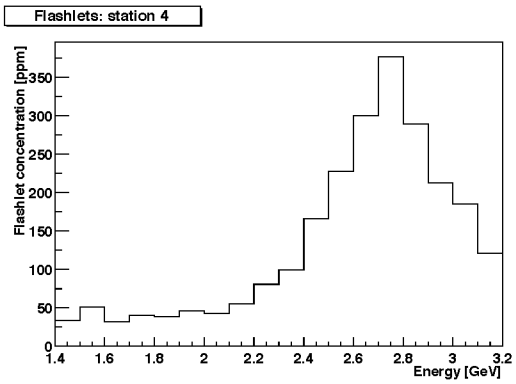

(d) Energy distribution in station 4

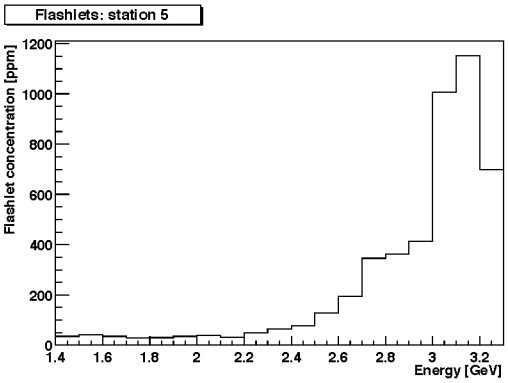

(e) Energy distribution in station 5

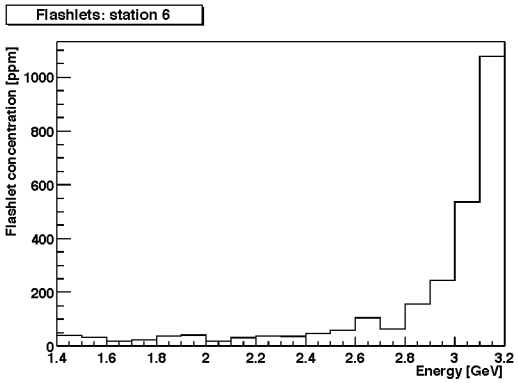

(f) Energy distribution in station 6

Figure 64: Flashlet distributions determined from the quads-off fills used to construct artificial flashlets.

	A	A'	B	B'	C	C'
Random seed	0.045	0.045	0.065	0.060	0.048	0.044
Bin width	0.061	0.057	0.151	0.123	0.094	0.103
Fast rotation time	0.080	0.073	0.115	0.111	0.085	0.078

Table 12: Systematic uncertainties from effects related to fast rotation.

15 Fast rotation effects

Five random seeds were used for the final results. For all of the start time groups, the RMS of the distribution of R values for the various seeds was approximately 0.1 ppm. The systematic uncertainty that is assigned for the random seed is therefore approximately 0.1 ppm/$\sqrt{5}$ = 0.45 ppm.

The fast rotation randomization period was varied from 149.0 ns to 149.4 ns in steps of 0.1 ns. (The nominal period is 149.2 ns.) For this study, the histogram time bin width remained fixed at 150 ns. The RMS of the resulting distribution of R values, which was approximately 0.1 ppm, was previously assigned as the fast rotation time systematic error. This is clearly an upper limit on the effect, since there are statistical variations among the various data sets as well. Indeed, at the ω_a review committee meeting, it was determined that this width is entirely within the statistical expectation, so it is not included as a systematic uncertainty.

Finally, the histogram bin width was varied from 148 ns to 152 ns in steps of 1 ns. The RMS of the distribution of R values, again approximately 0.1 ppm, is assigned as the bin width systematic error. Again, this is an upper limit because of statistical variations.

For each of these effects, the R and χ^2 values are shown in Figure 15. The systematic errors are summarized in Table 12.

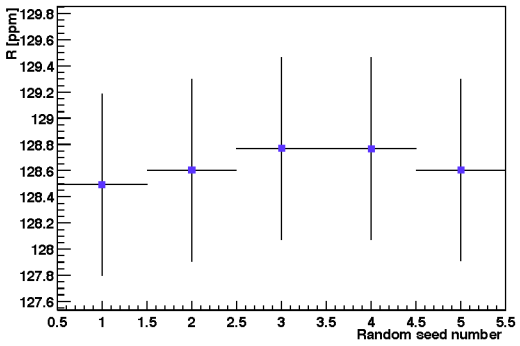

(a) Random seed R

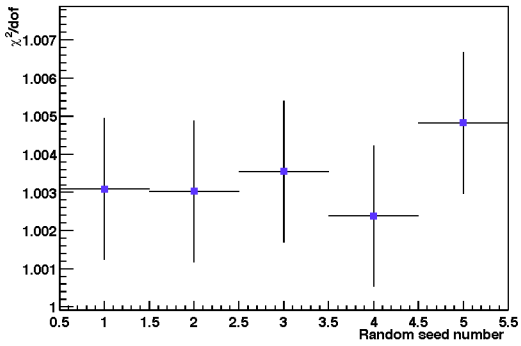

(b) Random seed χ^2

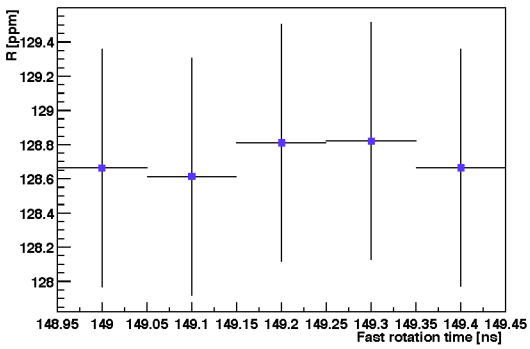

(c) Fast rotation time R

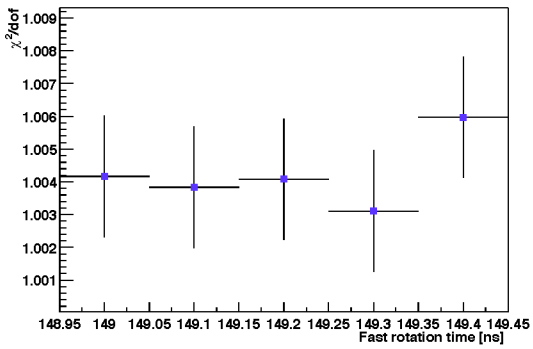

(d) Fast rotation time χ^2

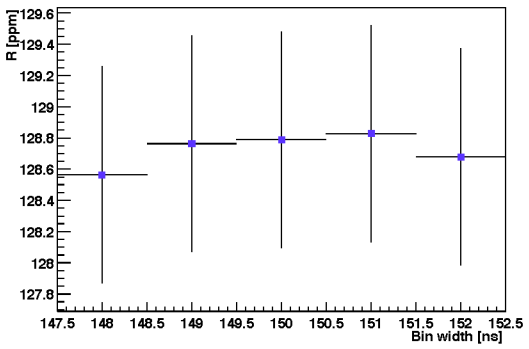

(e) Bin width R

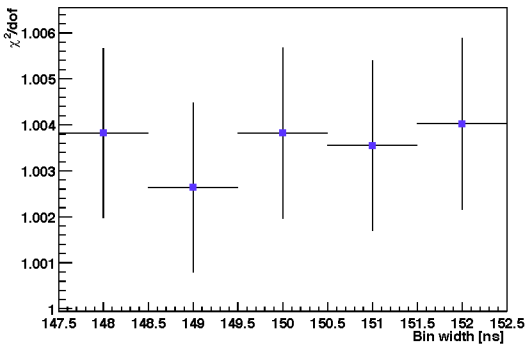

(f) Bin width χ^2

Figure 65: Results of systematic studies related to the fast rotation randomization

	A	A'	B	B'	C	C'
dR/dA_{VW} [ppm/unit of VW]	-0.0051	-0.0047	-0.0071	-0.0082	0.0030	0.0038
dR/dA_{2CBO} [ppm/unit of double CBO]	-0.012	-0.0082	-0.0066	-0.00066	-0.0083	-0.011

Table 13: Systematic effects from vertical waist and double CBO.

16 Vertical oscillations and double CBO

Particles in the storage ring perform vertical betatron motion at a frequency $f_{VO} = 2.36$ MHz. Beating with the fast rotation frequency leads to coherent motion–the "vertical waist"– with a frequency of $f_{VW} = f_{FR} - 2f_{VO} = 1.75$ MHz. Each of these effects leads to a modulation of the detector acceptance and therefore of the counting rate. These frequencies are well separated from ω_a, and the associated time constants are very short. The lifetime of the vertical betatron oscillations is approximately 3 μs, while that of the vertical waist is about 15 μs. Consequently, the effect on R is very small.

Also noticeable is the second harmonic of the radial CBO at 932 kHz. The time constant for this effect is significantly longer, about 50 μs, but the amplitude is very small.

The frequencies and time constants were estimated from overall fits at early start times. The amplitudes and phases were then determined for each energy bin for each station from fits starting at 31.6 μs. Stations 3 through 6 are not available at 31.6 μs; they were assigned vertical oscillation and vertical waist amplitudes and phases from the average of the other stations. For the vertical waist, the phase was adjusted properly for the ring position. The double CBO is sufficiently long-lived that its amplitude and phase can be reliably determined with a fit starting at 49.1 μs, so it is not necessary to interpolate values for stations 3-6 for this quantity. The parameters that were determined are shown in Figures 66 and 67.

For each of these modulations, fits were performed with the relevant amplitudes fixed at 0, 1, 5, and 10 times the values found from the early-time fits. The associated phases were held at the values found from the early-time fits. The slope of R versus the amplitude multiplier is determined.

The effect of the vertical betatron oscillations at these start times is too small even to write down; it is less than 0.0003 ppm in all cases. The systematic shifts of R and χ^2/dof from the vertical waist and double CBO are larger, though still very small. They are given in Table 13.

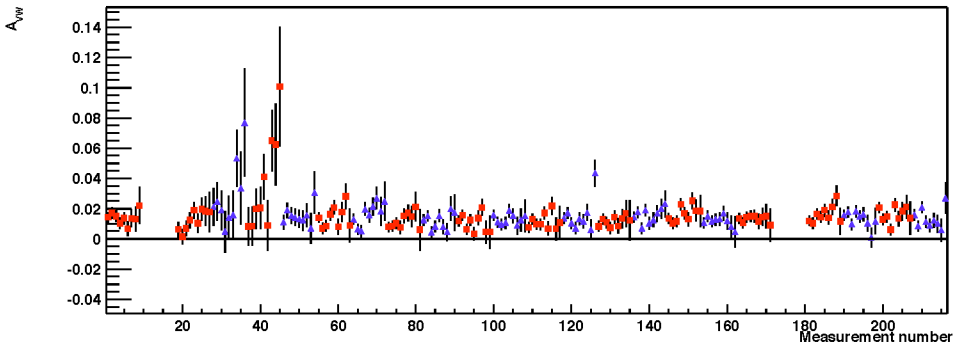

(a) Vertical waist amplitude

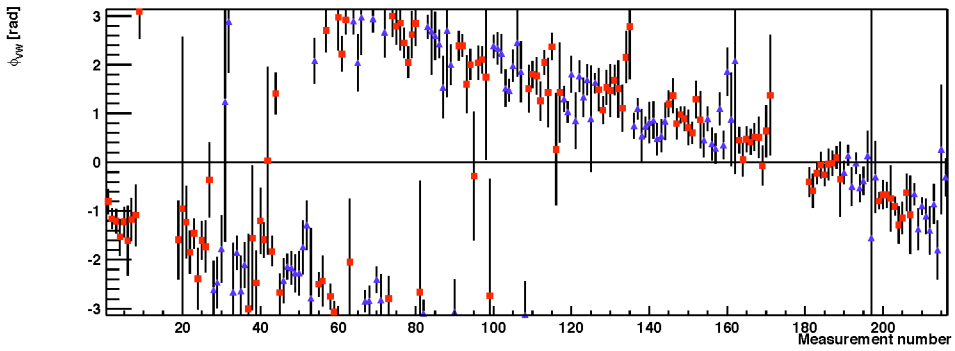

(b) Vertical waist phase

Figure 66: Vertical waist parameters determined from fits at early start times.

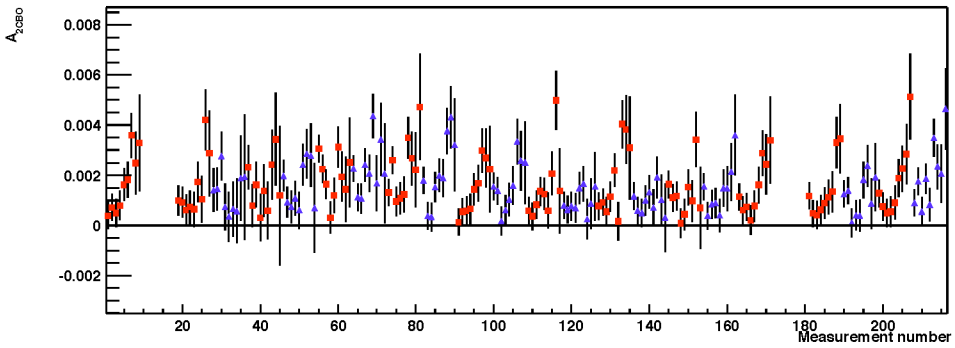

(a) Double CBO amplitude

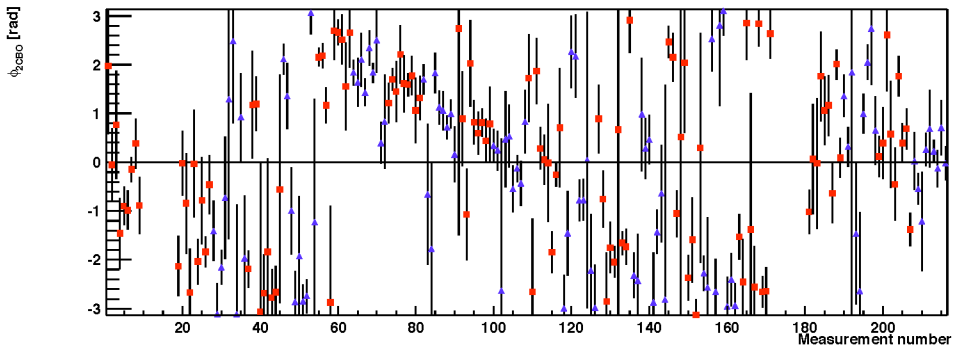

(b) Double CBO phase

Figure 67: Double CBO parameters determined from fits at early start times.

	A	A'	B	B'	C	C'
R for χ^2	128.848	128.706	127.944	127.703	128.574	128.449
δR for χ^2	0.627	0.673	0.720	0.771	0.691	0.743
R for $\log(L)$ (20 counts)	128.807	128.666	127.788	127.539	128.480	128.374
δR for $\log(L)$ (20 counts)	0.627	0.673	0.722	0.774	0.691	0.743
R for $\log(L)$ (550 μs)	128.863	128.709	127.892	127.728	128.458	128.363
δR for $\log(L)$ (550 μs)	0.618	0.663	0.714	0.762	0.680	0.729
$\delta R(\chi^2 - \log(L))$	0.041	0.040	0.156	0.163	0.094	0.075
δR ((20 counts) - 550 μs)	0.056	0.043	0.104	0.189	0.022	0.011

Table 14: Differences between results obtained with χ^2 and maximum likelihood fitting.

17 Maximum likelihood fitting

Sergei Redin suggested [5] that a potentially large bias results from fitting small subsets of the data with a χ^2 minimization. He suggested that the bias would be much smaller if a (log) maximum likelihood fit is performed instead. (This claim has since been retracted [6]; a similar bias is obtained for the two fitting methods.) This systematic error was evaluated by fitting with both methods and subtracting the results. The resulting systematic differences are of order 0.1 ppm, and they are largest for start time groups where the subsets are smallest. The results are listed in Table 14.

At an ω_a review committee meeting, Ernst Sichtermann pointed out that the difference between χ^2 and maximum likelihood fits is primarily statistical. As a check, Long Duong suggested comparing the results of χ^2 and maximum likelihood fits to data which was simulated with no statistical fluctuations. The difference between the results in this case was less than 0.001 ppm. Consequently, this "systematic error" is not included in the final table.

Jim Miller has also suggested that a bias may be introduced by the procedure of choosing a fit stop time based on the number of counts in a bin. Maximum likelihood fitting does not require a minimum number of counts per bin. Maximum likelihood fits were performed with a stop time of 550 μs in all bins. The difference between these results and those of the ordinary maximum likelihood fits is within the statistical expectation.

	A	A'	B	B'	C	C'
δR from lost protons	0.002	0.007	0.005	0.008	0.003	0.007

Table 15: Systematic errors from proton contamination.

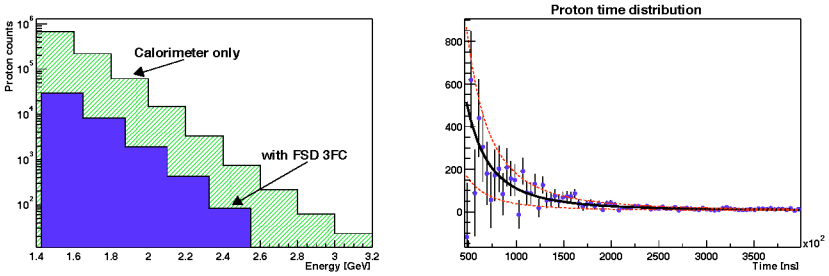

(a) Energy distribution (b) Time distribution

Figure 68: Energy and time distribution of lost protons.

18 Proton contamination

Because this analysis includes data from below 2 GeV, there is some contamination of the positron spectrum by lost protons. Their distribution was determined from Chris Polly's data. He identified straight tracks through three FSDs with energy deposited in the final calorimeter. The energy and time distributions are shown in Figure 68. There are two data sets in the energy distribution plot. One shows the energy distribution of all calorimeter pulses in the proton dump after the quads are turned off, and the other shows the distribution of those found in association with a threefold FSD coincidence. The ratio of the integrals of these distributions is approximately 13.4. The in-fill FSD triple coincidence data must be scaled up by this factor. There are 406 counts per station in this histogram in the ranges 1.3-2.2 GeV and 50-400 μs. Scaling up, there are 5440 proton counts per station in these ranges.

To determine the effect on R, simulated protons were added to the spectrum based on these distributions. They were added at levels corresponding to 0.33, 1.67, and 3.33 times the expected level (a factor-of-3 mistake was originally made in the normalization, leading to the peculiar numbers). The slope of R versus this scale factor is taken to be the systematic error. It is very small, in all cases less than 0.01 ppm. The results are given in Table 15.

τ	N	A	ϕ	R	A_{CBO1C}	A_{CBO1S}	A_{CBO2C}	A_{CBO2S}	A_{CBO3C}	A_{CBO3S}
1.000	-0.897	0.002	0.009	0.006	0.005	-0.003	0.003	0.005	-0.009	0.007
-0.897	1.000	0.002	-0.012	-0.009	-0.006	0.004	-0.004	-0.007	0.012	-0.010
0.002	0.002	1.000	-0.061	-0.065	0.007	0.000	0.106	-0.151	0.132	0.120
0.009	-0.012	-0.061	1.000	0.908	-0.002	0.002	0.146	0.197	-0.202	0.137
0.006	-0.009	-0.065	0.908	1.000	-0.002	0.001	0.097	0.164	-0.163	0.093
0.005	-0.006	0.007	-0.002	-0.002	1.000	-0.002	0.036	-0.004	0.067	0.004
-0.003	0.004	0.000	0.002	0.001	-0.002	1.000	0.001	0.034	0.001	0.062
0.003	-0.004	0.106	0.146	0.097	0.036	0.001	1.000	-0.000	-0.013	0.125
0.005	-0.007	-0.151	0.197	0.164	-0.004	0.034	-0.000	1.000	-0.177	-0.011
-0.009	0.012	0.132	-0.202	-0.163	0.067	0.001	-0.013	-0.177	1.000	-0.005
0.007	-0.010	0.120	0.137	0.093	0.004	0.062	0.125	-0.011	-0.005	1.000

Table 16: Parameter correlation matrix, averaged over fits to all stations and energy bins.

Energy [GeV]	1.4-1.6	1.6-1.8	1.8-2.0	2.0-2.2	2.2-2.4	2.4-2.6	2.6-2.8	2.8-3.0	3.0-3.2
τ	0.007	0.007	0.007	0.008	0.007	0.007	0.006	0.004	0.003
N	-0.01	-0.01	-0.01	-0.011	-0.01	-0.009	-0.009	-0.006	-0.004
A	-0.061	-0.061	-0.064	-0.065	-0.067	-0.068	-0.066	-0.067	-0.068
ϕ	0.904	0.901	0.908	0.912	0.909	0.905	0.909	0.914	0.914
R	1	1	1	1	1	1	1	1	1
A_{CBO1C}	-0.025	-0.011	-0.004	-0.002	0.001	0.003	0.003	0.004	0.009
A_{CBO1S}	0.022	0.004	0.002	0	-0.001	-0.003	-0.003	-0.003	-0.005
A_{CBO2C}	0.17	0.067	0.094	0.167	0.093	0.106	0.088	0.06	0.031
A_{CBO2S}	0.165	0.166	0.135	0.129	0.137	0.212	0.147	0.129	0.254
A_{CBO3C}	-0.171	-0.172	-0.14	-0.131	-0.139	-0.208	-0.143	-0.125	-0.241
A_{CBO3S}	0.171	0.063	0.092	0.164	0.088	0.103	0.081	0.053	0.025

Table 17: Correlations to R by energy, averaged over detectors.

19 Parameter correlations

The correlation matrix for the 12 free parameters in the fit is given in Table 16. This matrix is averaged over detectors and energy bins. In order to show the dependence on energy, the column with couplings to R is also given in Table 17. As expected, ϕ correlates very strongly with R. The half-ring effect amplitudes have a weaker but still significant correlation coefficient, approximately 0.2 in many of the energy bins.

References

[1] F.J.M. Farley, C.S. Özben, J. Pretz, and Y.K. Semertzidis, "Estimation of Error in Differential Pileup Subtracted Data," $(g-2)$ note 377.

[2] F. Gray, "Pulse fitting in G2Too", $(g-2)$ note submitted concurrently with this one.

[3] C. Polly, $(g-2)$ note in preparation.

[4] S.I. Redin, "Statistical Properties of Chi-squared," $(g-2)$ note 410.

[5] S.I. Redin, private communication, June 7, 2002.

[6] S.I. Redin, "Bias of fit parameters for log.likelihood and χ^2 minimization fits; $\sigma = \sqrt{N}$ versus $\sigma = \sqrt{f}$ for χ^2 minimization; possible improvement of χ^2 minimization fit," $(g-2)$ note to be submitted.

[7] Gerco Onderwater and Jörg Pretz, "Pile-up," $(g-2)$ note 363.